European Journal of Medicinal Chemistry 300 (2025) 118056

Contents lists available at ScienceDirect

European Journal of Medicinal Chemistry

journal homepage: www.elsevier.com/locate/ejmech

Research paper

Identification of pyrazolo-piperidinone derivatives targeting YAP-TEAD interface 3 as anticancer agents through integrated virtual screening and mass spectrometry proteomics

Laura Scalvini [a,1], Lorenzo Tagliazucchi [b,1], Gian Marco Elisi [a], Dana Zappaterra [b], Maria Gaetana Moschella [b,c], Sebastian Fantini [d], Daniele Aiello [b], Remo Guerrini [e], Valentina Albanese [e], Salvatore Pacifico [e], Ludovica Lopresti [f], Giulia Malpezzi [b,c], Giulia Saporito [b], Stefania Ferrari [b], Michele Lamesta [h,i], Lorena Losi [b], Cecilia Pozzi [f,g], Stefano Mangani [f], Gaetano Marverti [d], Alberto Venturelli [b], Glauco Ponterini [b], Domenico D'Arca [d,*], Marco Mor [a,**], Maria Paola Costi [b,***]

[a] Dipartimento di Scienze degli Alimenti e del Farmaco, Università degli Studi di Parma, Parco Area delle Scienze 27/A, I, 43124, Parma, Italy
[b] Department of Life Sciences, University of Modena and Reggio Emilia, Via G. Campi 103, 41125, Modena, Italy
[c] Clinical and Experimental Medicine (CEM) PhD Program, University of Modena and Reggio Emilia, Via G. Campi 287, 41125, Modena, Italy
[d] Department of Biomedical, Metabolic and Neural Sciences, University of Modena and Reggio Emilia, Via G. Campi 287, 41125, Modena, Italy
[e] Dept. of Medical Sciences and Laboratory for Technologies of Advanced Therapies (LTTA), University of Ferrara, 44121, Ferrara, Italy
[f] Department of Biotechnology, Chemistry and Pharmacy, Department of Excellence 2018-2020, University of Siena, via Aldo Moro 2, 53100, Siena, Italy
[g] Consorzio Interuniversitario Risonanze Magnetiche di Metallo Proteine (CIRMMP), Via Luigi Sacconi 6, 50019, Sesto Fiorentino (FI), Italy
[h] Department of Medical and Surgical Sciences for Children and Adults, University of Modena and Reggio Emilia, Modena, Italy
[i] Department of Precision Medicine in Medical, Surgical and Critical Care (Me.Pre.C.C.) PhD in Precision Medicine, University of Palermo, Palermo, Italy

ARTICLE INFO

Keywords:
Pyrazolo-piperidinone derivatives
TEAD targeting
Anticancer agents
Phenotypic screening
Fluorescence anisotropy
MS proteomics

ABSTRACT

The transcriptional activity of TEAD4 (transcriptional enhancer associated domain proteins), one of the final effectors of the Hippo pathway, can be dysregulated or mutated in cancer. Consequently, targeting the interaction between TEAD and its co-activator YAP (Yes Associated Protein) to disrupt the YAP:TEAD (Y:T) heterodimer has emerged as a promising anti-cancer strategy. Therefore, in this study, we aimed to identify novel scaffolds targeting the TEAD Interface 3 surface as effective anticancer agents against colorectal and ovarian cancer. Employing virtual screening, molecular dynamics, computational ADME-T prediction, and synthetic chemistry, we initially identified novel pyrazolo-piperidinone compounds exhibiting binding affinities (K_d) between 0.6 and 10 μM towards TEAD4 Interface 3 in a fluorescence anisotropy assay, with **6a** as the initial lead for a library of 20 compounds. A few of them demonstrated effective and well-characterized cellular antiproliferative activity against HCT116 and A2780 cancer cells. They demonstrated efficacy against colorectal cancer cells resistant to the KRAS-dependent clinical candidate IAG933 and confirmed the ability to inhibit TEAD4 target genes expression. Mass spectrometry-based proteomics of HCT116 cells treated with verteporfin and **6a** analogs revealed a proteome modulation consistent with an anti-TEAD mechanism of action, revealing the downregulation of CTGF and TGF-β1. Bioinformatic metabolic pathway analysis further differentiated the mechanism of action of the **6a** analogs from verteporfin, a known indirect modulator of the Y:T complex. These findings establish the pyrazolo-piperidinone class as novel Y:T disruptors and provide insights into their metabolic impact on downstream effectors, offering a valuable framework for future hit-to-lead optimization and mechanism of action studies.

* Corresponding author.
** Corresponding author.
*** Corresponding author.
E-mail addresses: domenico.darca@unimore.it (D. D'Arca), marco.mor@unipr.it (M. Mor), mariapaola.costi@unimore.it (M.P. Costi).
[1] Laura Scalvini and Lorenzo Tagliazucchi share the first position authorship.

https://doi.org/10.1016/j.ejmech.2025.118056
Received 22 April 2025; Received in revised form 4 August 2025; Accepted 6 August 2025
Available online 12 August 2025

Abbreviations

CRC	Colorectal Cancer
CTGF	Connective tissue growth factor
CYR61	Cysteine-rich angiogenic inducer 61
DEP	Differentially Expressed Protein
FA	Fluorescence anisotropy
FC	Fold-Change
HP	Hippo Pathway
MD	Molecular Dynamics
OC	Cvarian cancer
P6	Peptide 6
PDL5	Programmed cell death protein 5
TEAD	Transcriptional Enhancer Associated Domain
TGF-β1	Transforming Growth Factor Beta
TMR	Tetramethyl rhodamine
VP	Verteporfin
YAP	Yes Associated Protein
YBD	Yap Binding Domain

1. Introduction

The Hippo Pathway (HP) is a conserved signaling cascade that regulates cell proliferation and differentiation, tissue growth and organ size, under the control of various cytosolic and extracellular stimuli in all Eukaryotes [1–3]. The downstream co-activator of the HP is YAP (yes associated protein), which can be phosphorylated on S127 by LATS kinases, as a result of the signalling activation, leading to its own cytoplasmic retention and preventing its binding to TEAD1-4 transcriptional factors [4]. This results in the inactivation of the transcriptions of TEAD promoted genes, including CTGF, CYR61, Axl and BIRC5, all related to cell proliferation, and in the inhibition of pro-apoptotic mechanisms (Fig. 1A) [5].

Specific deletions of isoform 4 of TEAD have been correlated to poor prognosis in colorectal, ovarian, bladder and gastric cancers [6,7]. TEAD4 plays a key role in epithelial–mesenchymal transition (EMT), promoting metastasis in breast, lung, and colorectal cancers [8], which highlights TEAD4 and the Y:T complex as promising targets in cancer therapy [9].

In this perspective, in the last two decades different efforts to identify compounds able to interrupt the Y:T interaction have been performed. Strategies include the use of small molecules that retain YAP in the cytoplasm, reducing TEAD activity. Verteporfin (**VP**, Visudyne™), for instance, increases 14-3-3σ accumulation, leading to YAP cytosolic sequestration and TEAD inhibition [13–16]. On the other hand, direct TEAD inhibition can occur via covalent modification of a highly conserved cysteine residue, which undergoes a post-translational S-autopalmitoylation. Considering the fundamental role of this event in favoring the protein structure and its association with YAP [17,18], the design of compounds targeting the palmitoylation pocket has been adopted as a strategy to identify potent covalent and non covalent TEAD inhibitors [16]. These include acrylamide-based covalent inhibitors, as the nanomolar **K975** [19] and, more recently, the orally bioavailable **MYF-03–176** [20,21]. Other compounds targeting the palmitoylation site also include the reversible **IK-930** [22]**,** the low-nanomolar **VT-105** [23], and **GNE-7883** [24], a pan-TEAD inhibitor which was found to overcome KRAS G12C inhibitors resistance [25].

An alternative strategy in the design of inhibitors is based on the search of compounds able to impede the Y:T interaction at key protein–protein interfaces [26,27]. The resolution of the YAP:TEAD complex has offered valuable insighits into the identification of key protein residues involved in Y:T interacion [28], from the first structure of the human TEAD1:YAP complex (PDB ID: 3KYS), showing three main YAP regions interacting with TEAD, which include a β-strand (residues 52–58), an α-helix (61–73), and an Ω-loop (85–99) [10], to a more recent structure (PDB ID: 6Q2X) of TEAD4 bound to a shorter YAP fragment, confirming the critical role of the Ω-loop in binding to TEAD's hydrophobic surface (Fig. 1B and C) [11]. In this light, linear and cyclic peptides mimicking the structure of the Ω-loop of YAP (86–100), and binding the Interface 3 of TEAD were synthesized [29,30].

Using a fragment-based approach, Inventiva Pharma™ identified a library of Interface 3-interacting small molecules, patented for the treatment of mesothelioma [31]. More recently, Novartis™ developed Interface 3 targeting compounds, which represent the first class of potent small molecules disrupting the Y:T complex [32]. Among them, a dihydrobenzofurane derivative showed a promising pharmacological profile (**YTP-13** in Fig. 2, IC_{50} = 3 nM), further improved to give **IAG933**, currently under phase I clinical evaluation for the treatment of mesothelioma (**IAG933** in Fig. 2, clinical trials ID: NCT04857372) [33]. To date, only few Y:T interaction inhibitors are being included in solid tumor and mesothelioma cinical trials, all in phase I to test their safety, tolerability, pharmacokinetics and biological activity [33]. To fully explore the value of this approach, the pipeline of leads and clinical candidates still requires more compounds characterized by structural diversity and variable in vivo anticancer activities.

In the present work, we aimed to expand the repertoire of Interface 3 inhibitors classes to explore their potential application against drug-sensitive and resistant colorectal and ovarian cancers. To this aim, we initiated a virtual screening approach targeting the Interface 3 surface of

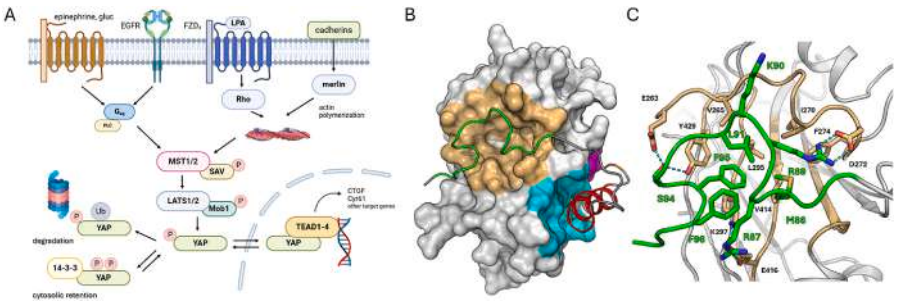

Fig. 1. (**A**) Schematic representation of the HP with its main regulators and upstream activators. (**B**). Crystallographic structure of TEAD1 (represented with light grey surface) and YAP (represented with colored cartoon; PDB id: 3KYS) [10]; structural elements of TEAD and YAP are highlighted: interface 1 (magenta surface), interacting with a strand motif of YAP (orange cartoon, residues 52–58); interface 2 (cyan surface), interacting with a helix motif of YAP (red cartoon, residues 61–73); interface 3 (light orange surface), interacting with the Ω-loop of YAP (green cartoon, residues 85–99) [10]. (**C**) Detail of the protein-protein interaction at the Interface 3 of the YAP:TEAD4 complex (PDB id: 6Q2X) [11]. The Ω-loop of YAP is represented with green cartoon and carbon atoms; TEAD4 is represented with grey and light orange cartoon and carbon atoms. Key residues for the stabilization of the complex are represented. Dashed cyan lines mark the interatomic distances between residues involved in polar contacts distances between residues involved in polar contacts. 3D rendering were obtained using the PyMol suite [12].

TEAD4, followed by hit confirmation and biological studies to demonstrate the capacity of the identified compounds to inhibit colorectal cancer (CRC) and ovarian cancer (OC) cell growth. The phenotypic screening allowed the selection of 5 hit compounds. Chemoinformatic analysis of the ADME-(eco)Tox properties guided the selection of the starting hit for library design and synthesis, namely pyrazolo-piperidinone derivatives. Over 24 compounds were synthesized and screened using a fluorescence anisotropy displacement method designed to measure the Kd for binding to the TEAD4 Interface 3 surface. Their potency was measured on CRC and OC cancer cell lines. The most potent compounds were further investigated using whole-cell bottom-up Mass Spectrometry (MS) proteomics on HCT-116 cancer cells treated with the 5 best derivatives to characterize protein modulation with respect to **VP**, used as a reference compound. An experimental workflow illustrating the steps performed to characterize the biological profile of the pyrazolo-piperidinone derivatives, ensuring future medicinal chemistry optimization, is depicted in Fig. 3.

2. Results

2.1. Virtual screening

A first virtual screening (VS) campaign was performed on the ChemDiv™ subset PPI Library, using the X-ray coordinates of the YAP: TEAD1 complex to identify compounds able to weaken the protein-protein interaction by targeting Interface 3 of TEAD YAP-binding domain (YBD). The initial library was preliminarily refined to exclude compounds with a low or a very high molecular weight (*i.e.* < 100 or > 900) and those characterized by an intrinsic high reactivity (Pan-assay interference compounds, PAINS). A pharmacophore model was then built starting from the structure of a potent cyclic macro-peptide [30] mimicking the YAP Ω-loop modelled on the surface of TEAD1 (Supplementary Information 1, Figure S1, Figure S2). The pharmacophore model was devised to favor compounds able to mimick the interactions of the side chain of Tyr421 of TEAD1, a conserved residue important for the complex stability, and to fit a hydrophobic cleft limited by residues Lys265, Lys289, Glu383, and Glu408 and occupied by non-polar residues of YAP and the macro-peptide (Fig. S2). The compounds of the library were then docked on Interface 3 of TEAD1, and submitted to a shape similarity search combined with the electrostatic treatment of atoms, using a portion of the YAP Ω-loop, to select molecules able to reproduce the arrangement of YAP residues pointing towards the surface of TEAD and to mimick the conformation of the Ω-loop. A consensus score, that combines the adherence to the pharmacophore model, the stereo-electronic similarity with the YAP Ω-loop, and the predicted binding affinity was applied to rank the compounds. The 3000 top-ranked molecules were selected and, as a final step, a hierarchical clustering was performed to reduce the number of scaffolds to be considered and, at the same time, to maximize diversification of chemical space among the potential lead compounds. A top-down approach was applied with the aim to identify a pre-defined number of clusters (50, in this case). Linear hashed fingerprints were used, and the Tanimoto similarity metrics was applied to cluster the compounds [34]. The resulting clusters were then analyzed to select, from each cluster, the compound characterized by the highest consensus score, finally giving 50 compounds. Given the high sequence identity shared by TEAD1 and TEAD4 (see **SI1**-Fig. S3 for sequence alignment and **SI1**-Fig. S4 for 3D structure alignment), and considering that the residues that enclose Interface 3 of the YBD are highly conserved in both isoforms, the same computational approach was applied to investigate whether the 50 compounds selected could also be evaluated as YAP: TEAD4 interaction inhibitors. Starting from the X-ray coordinates of TEAD4 co-crystallized with a potent linear peptide, a second VS was performed on the filtered ChemDiv™ library applying an analogous computational approach consisting of *i.* a screening based on a pharmacophore model built on the linear peptide, *ii.* a search based on the shape similarity to the YAP Ω-loop, and *iii.* docking on the Interface 3 of TEAD4 YBD. The same consensus scoring function, combining the adherence to the pharmacophore model, the stereo-electronic similarity to the YAP Ω-loop and the predicted binding affinity, was applied to rank the compounds. We verified that the 50 molecules, preliminarily selected in the VS *vs* TEAD1, were also found among the 3000 top-ranked compounds (**SI1**-Table S1, **SI2**) of the second VS round (**SI2**, virtual screening docking scores *vs* TEAD4). The predicted properties of the 50 compounds are reported in **SI1**-Table S1. The selected compounds were tested against the two isoforms TEAD1 and TEAD4, thus ensuring a selectivity for the TEAD proteins. We could expect that the compounds were potentially active against both isoforms TEAD1 and TEAD4, however all the experimental work was performed on TEAD4 that is of major interest in the selected target cancers. These compounds were then screened on cancer cells to assess their anticancer properties against CRC and OC cells.

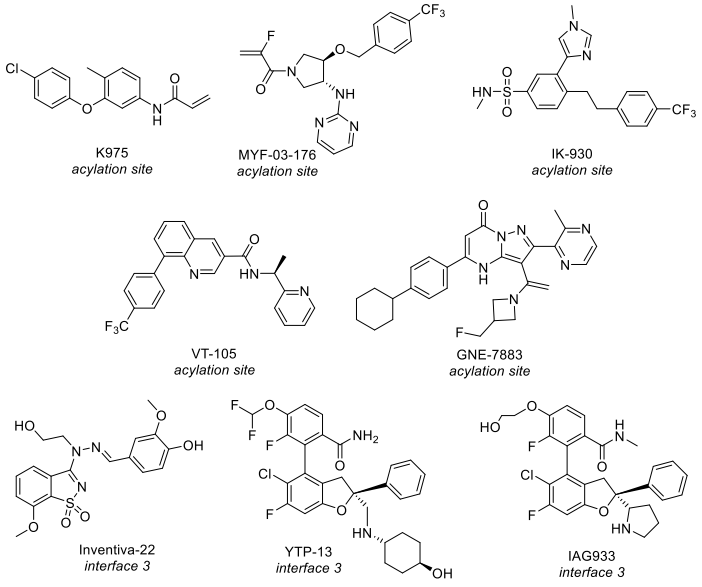

Fig. 2. Chemical structures of the most outstanding non-peptidic Y:T complex inhibitors with relevance in research and clinical development. The targeted binding interface on TEAD are reported below the compound code.

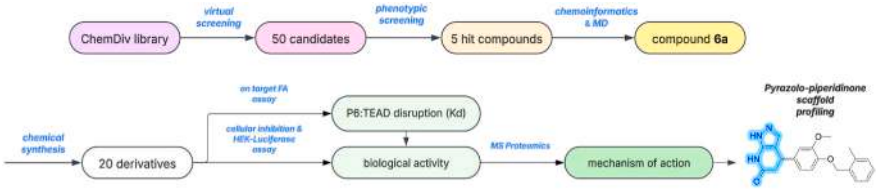

Fig. 3. Workflow of the drug discovery program aimed at the identification of TEAD4 Interface 3 binders and target genes modulator. The program started with a virtual screening campaign and ended with a MS characterization of the biochemical pathways involved in the response to our new pyrazolo[3,4-*b*]pyridin-6-one derivatives. This diagram was generated with Lucidchart™.

2.2. Evaluation of the anti-proliferative effects on cancer cells of the ChemDiv compounds

To test the capacity of the 50 compounds to reduce cancer cell growth, and select compounds for hit development, the library was first evaluated against HT29 (CRC) and A2780 cells (OC). The compounds, obtained from the ChemDiv™ vendor, were tested without further purification. The cancer cell lines were selected based on their profiles. HT29 are CRC cells resistant to the 5-fluorouracil prodrug, which harbour the Adenomatous Polyposis Coli (APC) mutations and depend on YAP1 for survival [35]. The cisplatin-sensitive A2780 cell line represents a well-established cell model to study the HP [36], in which YAP was shown to promote the self-renewal of OC-initiated cells through its binding to TEAD [37]. Therefore, Y:T complex modulation in both cell lines may alter cancer cell growth. Each compound was screened against both cell lines. Only compounds causing 40 % or higher cell-growth inhibition at 40 μM were further investigated. **VP** was used as positive control. **VP** shows respectively 70 % and 52 % inhibition with respect to HT29 and A2780, results consistently with previous literature. The results are reported in Fig. 4 and **SI1**-Table S2.

The compounds showing the highest cancer cell growth inhibition at 40 μM against at least one cell line (**VS3, VS6, VS22, VS23, VS37**) were tested at 5–40 μM on both cell lines for 72 h to obtain IC_{50} values. The IC_{50} detection was extended to the human CRC cell line, HCT116, and to A2780/CP, OC cells resistant to cisplatin. The HCT116 cell line expresses low TAZ levels and represents a known cell model for exploring the biological functions of the YAP:TAZ interaction [37]. A2780/CP cells were chosen based on their constitutive upregulation of TEAD2/4 levels, which contribute to drug resistance in vitro and in vivo in these cancer cells [37]. The IC_{50} values obtained for the five compounds and **VP**, together with their structures, are reported in Table 1 and Fig. 5. Their computed chemical properties are reported in **SI1**-Table S3.

Some of the selected hit compounds feature IC_{50} values lower than 40 μM, and two of them (**VS3**, **VS22**) around 15 μM *vs* the A2780 cells. Between the two colon cancer cell lines, the best IC_{50} values were observed on HCT116 cells. Only compounds **VS3** and **VS37** showed IC_{50} values higher than 40 μM. On the contrary, in the case of HT29 cells, four compounds out of 5 did not reach a 50 % growth inhibition at 40 μM, and compound **VS23** showed an IC_{50} value close to this concentration limit. The most active compounds were **VS3** and **VS22** with

Table 1
IC_{50} values of the 5 hit compounds against A2780, HCT116 and HT29.

Compound code	IC_{50} (μM)		
	A2780	HCT116	HT29
VS3	13.0 ± 6.4	>40	>40
VS6	28 ± 5	28 ± 3	>40
VS22	14.9 ± 4.9	38.4 ± 2.6	>40
VS23	24.7 ± 5.3	38.1 ± 2.3	30.0 ± 6.9
VS37	27.9 ± 7.9	>40	>40
VP	12.4 ± 2.1	24.6 ± 2.2	36

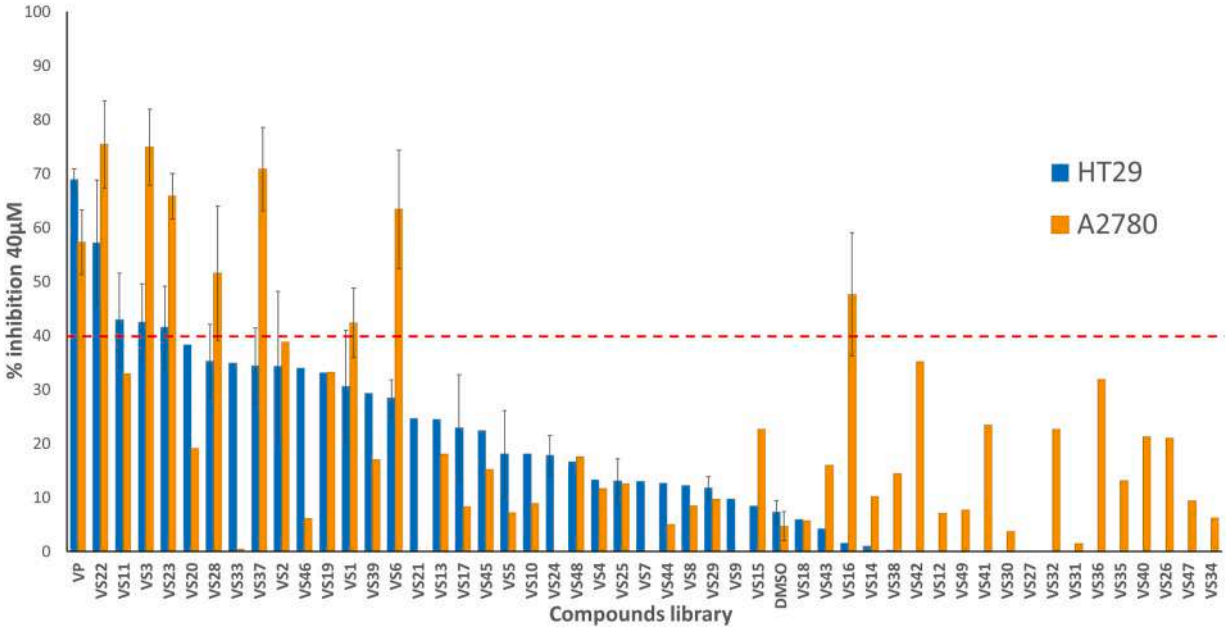

Fig. 4. Graphical representation of the inhibition potency shown by the 50 compounds against HT29 (CRC, 5FU resistant) and A2780 (OC, cisplatin sensitive) performed with the crystal violet assay at 40 μM (see cut-off line in red is set at 40 %) for 72hrs. The compounds were selected for further development if they show 40 % of growth inhibition at the tested concentration with respect to the control with the solvent only; **VP** is the compound of comparison. The bars represent the mean ± SEM of three separate experiments performed in duplicate. **SI1**-Table S2 reports the numerical values.

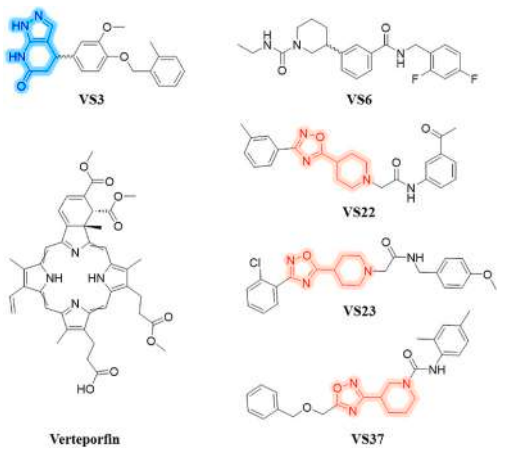

Fig. 5. Chemical structures of the 5 hit compounds and verteporfin (**VP**). The pyrazole piperidinone scaffold is colored in blue, the oxadiazole -piperidine fragment in red.

IC_{50} values of 13.0 ± 6.4 and 14.9 ± 4.9 μM against A2780 cells. The two compounds have prominent hydrophobicity, typical of PPI inhibitors [38]. Three molecules (**VS22**, **VS23**, **VS37**) share a common piperidin-oxadiazole moiety prompting the idea that this could be a key fragment for the protein-ligand interaction (**SI3**).

2.3. Selection of a hit compound for synthetic development

The 5 selected hits that emerged from the phenotypic screening underwent a chemoinformatic evaluation in comparison with **VP**, **IK-930** and **IG933**, to detect their expected drug likeliness and ADME-(eco) Tox parameters. **VP** and compounds **IK-930** (a non covalent ligand targeting the acylation site) and **IAG933** (Interface 3 ligand and clinical candidate) were included as reference compounds. **VP** and **IK-930** were chosen to represent compounds that, while acting on the HP pathway, have either a target different from the Y:T complex formation (**VP**), or a different mechanism of action on TEAD (**IK-930**). The ADMETLab 2.0 tool was employed for this purpose and the results are represented in Fig. 6 [39]. The predictive models are built over validated chemical libraries and compare the physicochemical properties of the input molecules. Drug-likeliness parameters suggest that all the selected compounds comply with standard guidelines for drug design [40,41]. The results suggest that compound **VS3** is the only one that is not expected to cross the Blood Brain Barrier (BBB) (Fig. 6, Distribution) and shows low cytochromes inhibition (**SI1**-Table S4). All compounds showed a medium to high predicted *h*ERG inhibition activity and moderate hepatotoxicity. However, none of them is predicted to interfere with either the Heat shock factor response element, the mitochondrial membrane potential, or with the p53 pro-apoptotic pathway. Also, compound **VS3** does not show interaction with the estrogen/androgen receptors, suggesting no endocrinous interference properties. All compounds display satisftying ecotoxicological parameters, with low toxicity for the model organisms (Tetrahymena pyriformis, fathead minnow, and Daphnia magna), with compound **VS3** scoring the highest EC_{50}/LD_{50} values, and the best profile [39]. The profile of compound **VS3** was very similar to that of **IK-930** and better than **IAG933**.

Details of the considered parameters and thresholds of acceptance are reported in **SI1**-Table S4. The outcome of the analysis was compared with the results of a parallel evaluation with the SwissADME tool (**SI1**-Table S5). The results of the chemoinformatic analysis predicted compound **VS3** as the safest compound among those evaluated. Altogether, the above results prompted the selection of compound **VS3** for further pyrazole[3,4-b]pyridine derivative design.

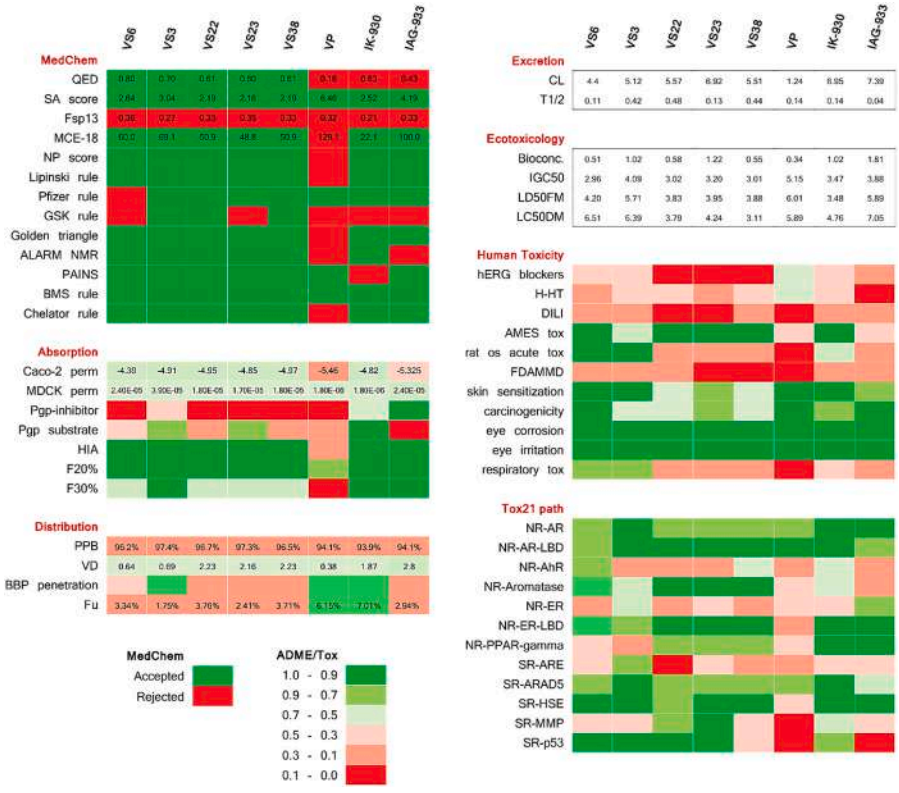

Fig. 6. HeatMap represention of the predicted drug likeliness and ADME-Tox parameters for the five compounds identified in the phenotypic screening through the ADMETLab 2.0 software [39]. The outcomes of the analysis are expressed as 'accepted (green)/rejected (red)' for the MedChem section parameters. Scoring of the other sections (absorption, distribution, metabolism, toxicity, Tox21 Pathways, Excretion and ecotoxicology) are expressed with a six-level colour scale of percentage probability, from dark green (lowest predicted probability) to dark red (highest predicted probability).

2.4. Docking and molecular dynamics simulations of compound VS3, and design of its derivatives

To develop a series of molecules active towards Interface 3, the interaction mode of compound **VS3** with TEAD was modelled by computer simulations and the results formed the basis for the design of new derivatives. Analysis of the docking pose of compound **VS3** on the Interface 3 of TEAD4 showed that the methylbenzyl group occupied a hydrophobic cavity that is lined by the side chains of Phe274, Leu295, Thr394 and Val414 of the protein (Fig. 7A) and that accommodates the side chain of Met86 of the YAP Ω loop. The pyrazolo[3,4-*b*]pyridin-5-one group made polar interactions with the NH group of the backbone of Asp266 (Fig. 7A). To assess the stability of this binding pose, two 500 ns-long MD simulations were performed. During the simulations, the binding pose was characterized by a high stability (**SI1-**Fig. S5). The methylbenzyl group was firmly inserted within the hydrophobic cavity, taking hydrophobic contacts with the side chains of Phe274 and Val414. In one of the simulations, the pyrazole[3,4-*b*]pyridin-5-one group modified its initial orientation, in which it took hydrogen bonds with the backbone of Asp266, to a specular one, obtained by rotation around the bond between the pyrazole[3,4-*b*]pyridine and the metoxyphenyl moiety. In this conformation, the ligand formed polar contacts with the side chains of Glu263 and Tyr429 (**SI1**-Fig. 7B).

While this manuscript was in preparation, the crystal structure of TEAD4 in complex with a novel potent inhibitor (**YTP-13,** a **IAG933** analog) bound to Interface 3 of the protein was reported [32] (**SI1-**Fig. S6). In this structure, the 5-chloro-6-fluoro-2,3-dihydrobenzofuran group of the ligand occupies the same hydrophobic sub-pocket that accommodates the 6-chlorotryptophan amino acid of the optimized linear peptide co-crystallized with TEAD4. The phenyl substituent at position 2 of the dihydrobenzofuran sits within a small cleft delimited by the side chains of Lys297, Trp299 and Glu416 (**SI1-**Fig. S6). This cleft, which serves as an anchoring point for the hydrophobic scaffold of the ligand, is not present in other crystallographic structures of TEAD4, where Lys297 and Glu416 are usually engaged in a ionic bridge. An additional 4-aminocyclohexan-1-ol substituent at position 2 of the dihydrobenzofuran is placed within a solvent-exposed polar cavity, lined by the side chains of Asn387, Glu392 and Glu416, while the 4-difluoromethoxy-benzamide fragment occupies the upper part of the cavity on the TEAD4 Interface 3 engaging the side chain of Lys297 in a polar contact. A major difference between this crystal structure and the crystal structure used in this work thus lies in the different orientation of the Lys297 side chain, while the RMSD calculated for Cα atoms of residues within 7 Å from the coordinates of the co-crystallized inhibitor is 0.36 Å. An alternative binding mode of compound **VS3**, in which the methylbenzyl and methoxyphenyl group superimposed the phenyl substituent and dihydrobenzofuran ring of **YTP-13**, respectively, was modelled (**SI1-**Fig. S7). To assess the stability of this binding pose, a 250

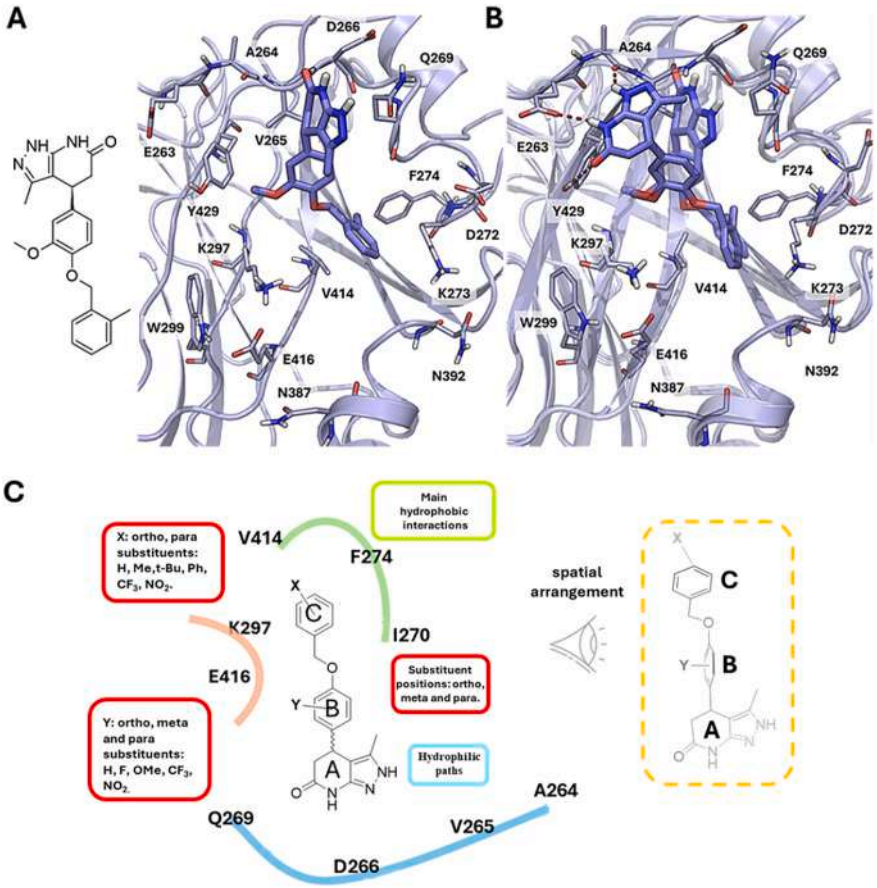

Fig. 7. (**A**) Docking pose of **VS3** (light blue carbon atoms) on the Interface 3 of hTEAD4 YAP binding domain (grey carbon atoms and cartoons). The methylbenzyl group is inserted within the hydrophobic cavity on the surface of *h*TEAD4, while the pyridinone group takes polar contacts with the backbone of Asp266. The 2D representation of **VS3** is also reported on the left. (**B**) Superposition of the binding mode of **VS3** (transparent atoms) and a conformation identified during one of thea 500 ns-long MD simulations (light blue carbon atoms), in which the pyrazo-pyridinone group assumed an alternative orientation, taking additional polar contacts with Tyr429 and Glu263. Hydrogen bonds are marked with dark red dashed lines. (**C**) 2D representation of the binding mode of **VS3** derivatives on the *h*TEAD4 Interface 3. The hydrophobic scaffold, comprising rings B and C, is involved in the main hydrophobic interactions highlighted by a green line. In contrast, the hydrophilic interaction pathways are delineated by a blue line. To probe the impact of bulkier substituents on the activity of this class of compounds, the original methoxy and methyl groups (denoted as X and Y, respectively, in compound **VS3**) were specifically replaced. The substitutions on rings B and C, along with their precise positions, are highlighted in red boxes for clarity. On the right, spatial arrangement of the three rings within the binding pocket.

ns-long MD simulation was performed. Shortly after few nanoseconds of MD simulation, the ligand assumed a different conformation, similar to the binding mode obtained *via* docking simulations, in which the methylbenzyl portion was directed towards the hydrophobic sub-pocket for the 6-chlorotryptophan amino acid, and the methoxyphenyl group was placed in the cavity lined by Val265, Leu295 and Tyr429 (**SI1**-Fig. S7). Taken together, the results of the molecular modelling studies suggest that the phenyl rings of compound **VS3** represent a key element in the stabilization of the ligand binding mode, serving as an anchor to the Interface 3 of TEAD4.

Starting from these results, novel derivatives of compound **VS3** were designed and synthesized to be evaluated as inhibitors of the Y:T complex formation. We thus investigated the effect of different substituents on the benzyl fragment or at the central methoxyphenyl moiety (Fig. 7C). For clarity, in the following sections, the compound numbers are referred to the section "Synthesis of compound **VS3** derivatives**"**. Compound **VS3** was acquired from the vendor and tested without further characterization or purification. After re-synthesis it was renamed compound **6a**.

Analysis of docking studies showed that, consistently with the binding mode identified for **VS3(6a)**, compounds with planar and bulky substituent at the para position of the benzyl ring (**6k**, **6m**, **6l**, and **6n**; Fig. 8) occupied the cleft on the surface of TEAD4, inserting their hydrophobic portion within the hydrophobic sub-pocket for the 6-chlorotryptophan amino acid. On the opposite side, the pyrazolo[3,4-*b*] pyridin-5-one group of larger derivatives was accommodated towards the side chain of Glu263 and Tyr429, taking additional polar interactions and mimicking the polar interactions between the side chain of Ser94 of YAP and of Tyr421 and Glu255 of TEAD1 (Tyr429 and Glu263 in TEAD4), as in Fig. 8.

2.5. Synthesis of derivatives of compound VS3 (6a)

The synthesis involved two steps as shown in Scheme 1. Firstly, a Williamson ether synthesis was performed using aryl-bromide **1** (1.0 eq), 4-hydroxy-aldehyde **2** (1.1 eq) and an excess amount of K_2CO_3 with acetonitrile (ACN) as the solvent at reflux for 4hrs. The second step was a multicomponent reaction for the formation of the 3-methyl-1,4,5,7-tetrahydro-6H-pyrazolo[3,4-b]pyridin-6-one heterocycle, derivatives **6**, and was performed using an equimolar amount of aldehydes **3a-r** obtained in step 1, 5-methyl-1H-pyrazol-3-amine **4** and Meldrum's Acid **5** under refluxing MeOH for 18hrs [42]. Almost all compounds possess a stereocenter at position 4 of ring A. However, the synthetic methodology employed is not stereoselective, leading to the formation of racemic mixtures. The biological assays were performed with such racemic mixtures. The compounds characterization is reported in **SI4** and **SI5**.

As depicted in Scheme 2, we also attempted to synthesize meta-substitued compounds. Also in this case, the synthetic procedure involved formation of the ether using a Williamson reaction followed by a multi-component reaction to obtain and connect the pyrazol[3,4-b] pyridin-6-one moiety. Compound **9** was obtained by this route. Subsequent hydrolysis of the cyano group in the presence of 4 M NaOH made

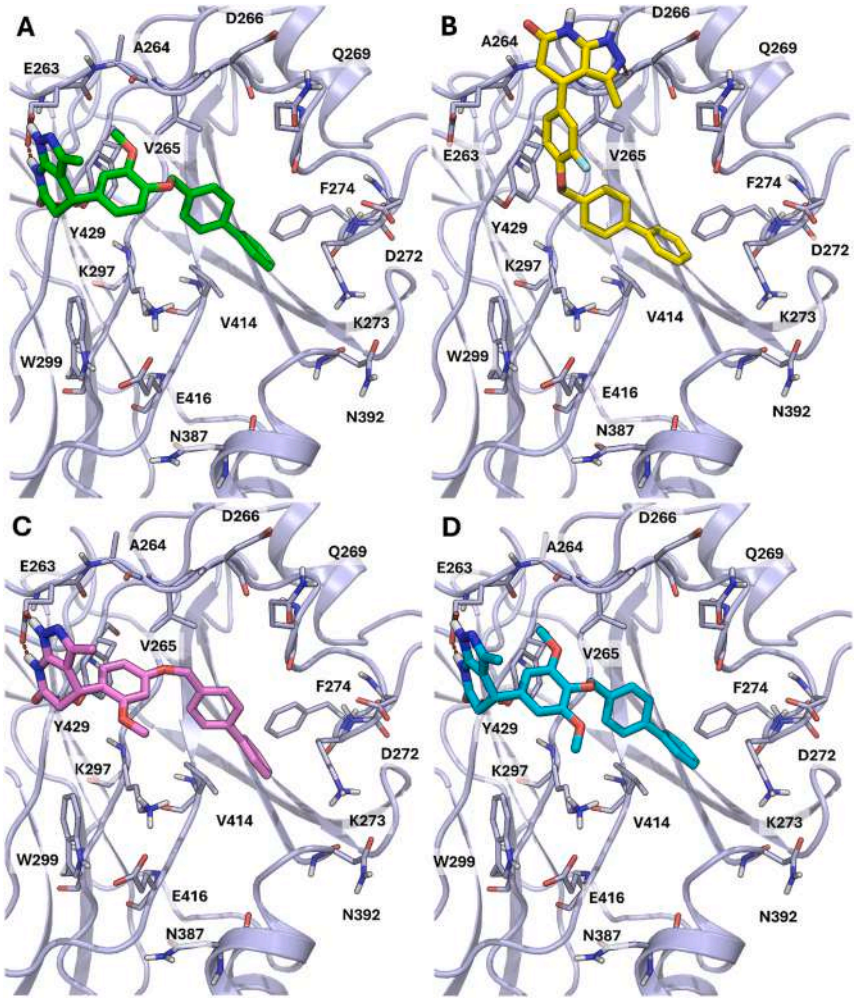

Fig. 8. Docking poses of derivatives of compound **VS3(6a)** with bulkier hydrophobic scaffolds on the surface of TEAD4 (grey carbon atoms and cartoons): **6k** (A; green carbon atoms) **6l** (B; yellow carbon atoms), **6m** (C; pink carbon atoms) and **6n** (D; cyan carbon atoms). Hydrogen bonds are marked with dark red dashed lines.

1a-e

	R1	R2
1a	H	Me
1b	H	CF_3
1c	H	NO_2
1d	*t*-Bu	H
1e	Ph	H

2a-h

	R3	R4	R5
2a	OMe	H	H
2b	CF_3	H	H
2c	NO_2	H	H
2d	F	H	H
2e	H	H	OMe
2f	OMe	OMe	H
2g	NO_2	OMe	H
2h	NO_2	F	H

3a-r

	R1	R2	R3	R4	R5
3a	H	Me	OMe	H	H
3b	H	Me	CF_3	H	H
3c	H	Me	NO_2	H	H
3d	H	CF_3	OMe	H	H
3e	H	CF_3	CF_3	H	H
3f	H	CF_3	NO_2	H	H
3g	H	NO_2	OMe	H	H
3h	H	NO_2	CF_3	H	H
3i	*t*-Bu	H	OMe	H	H
3j	*t*-Bu	H	NO_2	H	H
3k	Ph	H	OMe	H	H
3l	Ph	H	F	H	H
3m	Ph	H	H	H	OMe
3n	Ph	H	OMe	OMe	H
3o	H	Me	NO_2	OMe	H
3p	*t*-Bu	H	NO_2	OMe	H
3q	H	Me	NO_2	F	H
3r	Ph	H	NO_2	H	H

6a-r

	R1	R2	R3	R4	R5
6a	H	Me	OMe	H	H
6b	H	Me	CF_3	H	H
6c	H	Me	NO_2	H	H
6d	H	CF_3	OMe	H	H
6e	H	CF_3	CF_3	H	H
6f	H	CF_3	NO_2	H	H
6g	H	NO_2	OMe	H	H
6h	H	NO_2	CF_3	H	H
6i	*t*-Bu	H	OMe	H	H
6j	*t*-Bu	H	NO_2	H	H
6k	Ph	H	OMe	H	H
6l	Ph	H	F	H	H
6m	Ph	H	H	H	OMe
6n	Ph	H	OMe	OMe	H
6o	H	Me	NO_2	OMe	H
6p	*t*-Bu	H	NO_2	OMe	H
6q	H	Me	NO_2	F	H
6r	Ph	H	NO_2	H	H

Scheme 1. General synthetic routes for compounds **6a-r**.

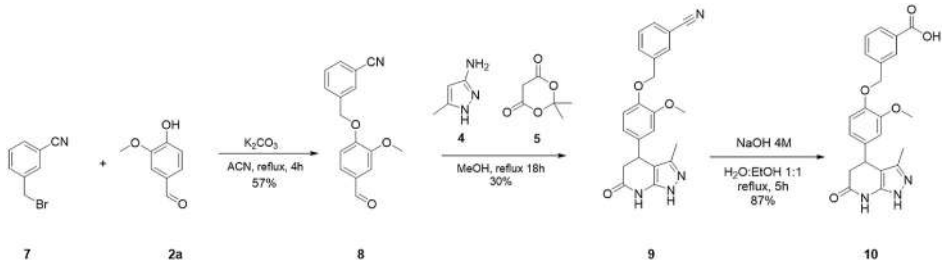

Scheme 2. Synthesis of compounds **9** and **10.**

possible the formation of compound **10**.

2.6. Synthesis of reference compounds 20 and 23

Compounds **20** and **23** were synthesized as reference compounds, following the expected mechanism of action reported in the Inventiva Pharma™ patent [31]. The synthesis of compounds **20** (compound 22 in the Inventiva Pharma™ patent [31]) and **23** (compound 2 in the patent) involved three steps. In the first one, saccharin (commercially available) or saccharin derivatives (prepared according to Scheme 3) reacted with chlorinating agents such as thionyl chloride in the presence of N, N-dimethyl formamide to obtain 3-chloro-1,2-benzothiazole 1,1-dioxides. In the second step, 3-methoxy-4-hydroxy-benzaldehyde reacted with various hydrazines to give 2-methoxy-4-hydrazonomethyl-phenols that would react in step 3 with 3-chloro-1,2-benzothiazole 1,1-dioxides to give the desired compounds [31].

As depicted in Scheme 3, the synthesis of compound **20** required the preparation of the intermediate **17**. The route began with the sulfonylation of cumylamine (**12**) with 2-methoxybenzenesulfonyl chloride (**11**) in the presence of Et_3N and the The resulting sulfonamide was subjected to an ortho-lithiation using a pre-mixed TMEDA/n-BuLi solution in THF at 0 °C, followed by reaction with diethylcarbamoyl

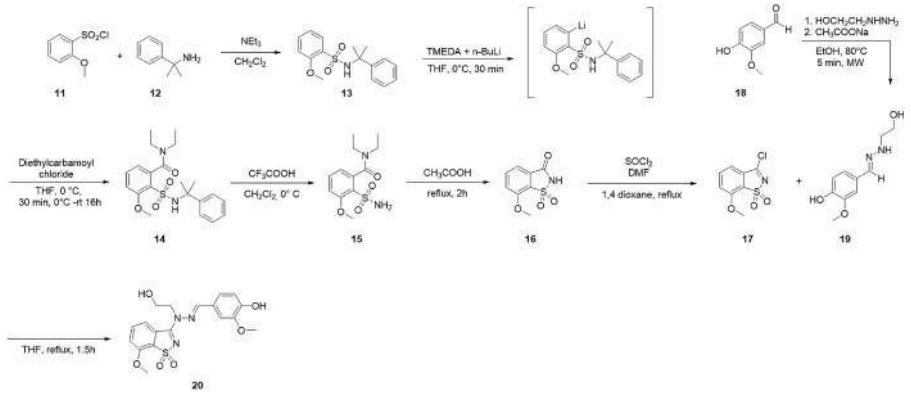

Scheme 3. Synthesis of (E)-4-((2-(2-hydroxyethyl)hydrazineylidene)methyl)-2-methoxyphenol **19** and compound **20.**

chloride to afford compound **14** in 43 % yield.

Decumylation with TFA and subsequent ring closure in refluxing acetic acid gave compound **16**. Chlorination with $SOCl_2$ in 1,4-dioxane (DMF-catalyzed) yielded intermediate **17**.

In a separate sequence, condensation of 3-methoxy-4-hydroxybenzaldehyde with hydroxyethyl hydrazine under microwave irradiation (EtOH, NaOAc, 80 °C) afforded hydrazone **19**. Coupling of compound **17** with **19** in refluxing THF, followed by recrystallization from acetonitrile, furnished compound **20**.

As shown in Scheme 4, compound **23** was synthesized starting from commercial saccharin (**21**), chlorinated with $SOCl_2$/DMF to give **22**, which was then coupled with hydrazone **19** under the same conditions used for compound **20**, yielding compound **23** after recrystallization.

2.7. Fluorescence-anisotropy displacement assay and binding affinity evaluation

Aiming to develop an assay to screen compounds able to destabilize the Y:T complex, we have designed a displacement test based on fluorescence anisotropy. The latter can be employed as a suitable observable to monitor and quantitatively characterize formation and disruption of a complex between a small interactor, in our case peptide 6 **(P6)**, mimetic of the YAP Ω-loop, labelled with tetramethylrhodamine (TMR, **P6-TMR**), and a protein, in our case YAP Binding Domain (YBD) of TEAD4. A recently obtained X-ray crystal structure of the **P6**:TEAD4 complex showed the peptide bound at the Interface 3 of TEAD4. The crystal structure will be published in a forthcoming paper (in preparation). Binding of **P6-TMR** at the YBD Interface 3 of TEAD4 reduces the rotational freedom of the TMR fluorophore and causes an increase in its anisotropy. Conversely, displacement of the peptide from the protein by a suitable compound results in an anisotropy decrease. The TMR emission anisotropy was measured between 560 and 610 nm upon excitation at 550 nm and the average value between 575 and 600 nm was taken, together with the associated uncertainty. At room temperature in a 4:1 acqueous-glycerolic solution, the anisotropy of **P6-TMR** alone was $r = 0.14 \pm 0.01$. Subsequent additions of TEAD4 to **P6-TMR** caused its increase up to a final value of 0.27 ± 0.02, thus confirming binding of **P6-TMR** to the protein. The final anisotropy was stable, between 0.25 and 0.28, for at least 2 h. A standard binding equilibrium analysis of the results of this titration allowed us to evaluate the equilibrium constant for dissociation of the **P6-TMR**/TEAD4 complex (Fig. 9A). We found $K_{PT} = 0.25 \pm 0.03$ μM. To validate the displacement assay, we first performed **P6-TMR** displacement from TEAD4 by untagged **P6**. The starting sample consisted in a 3:1 (mol/mol) TEAD4:P6-TMR solution (900 nM:300 nM) ($r_0 = 0.26 \pm 0.01$). **P6** was added progressively and the emission anisotropy was measured until a stable value was reached, $r_\infty = 0.14 \pm 0.01$, corresponding to full displacement of **P6-TMR** from TEAD4. The results were analyzed with a model that accounts for the competitive binding of two different ligands, one progressively displaced by the other, to a protein molecule [43,44]. For the incoming **P6** ligand, we determined an equilibrium constant for dissociation from TEAD4 $K_P = 0.30 \pm 0.05$ μM, a result consistent with the above K_{PT} for the TMR-tagged peptide and with the IC_{50} value, 0.409 ± 0.055 μM, obtained by a time-resolved-FRET experiment [11]. Also, the inhibitor **IAG933**, with high specificity for the TEAD:YAP complex, was used to validate the anisotropy-based displacement assay [33]. **IAG933** effectively displaced the P6TER probe. The experimentally determined K_d (≈10 nM) was consistent with the literature value (8 nM, determined by TR-FRET). This validation supports the reliability of this assay for profiling Y:T complex formation inhibitors.

The same method was used to investigate the displacement of **P6-TMR** from TEAD4 by the compounds synthesized with the aim to interfere with the Y:T complex formation. The displacement was quantitatively assessed by measuring the decrease in the emission anisotropy of the fluorescent probe as a function of the incoming displacer concentration. The same data fitting, based on the previously mentioned competitive binding model, was applied to estimate the K_ds of the incoming-displacer/TEAD complexes. A few examples of displacement titration results are shown in Fig. 9B (compounds **P6, 6r, 6l, 6e** and **6m**). Some compounds produced results that were either little reproducible or not acceptably fitted by the displacement model (**6j**, **6n**, **6p**). We believe that this misbehaviour was related to their rather high hydrophobicities and resulting aggregation in the aqueous buffer. This hypothesis was also supported by the observation of light scattering producing high baselines in the UV–vis absorption spectra. The K_d values, determined for compounds whose data could be reasonably well fitted, are collected in Fig. 10 and in Table 2. Additionally, **VP** was tested as TEAD inhibitor and no binding to TEAD was observed up to 40 μM.

Most of the compounds featured K_d values in the 2–10 μM range with **6r** as the highest affinity compound ($K_d = 0.6$ μM). The reference compounds, **20** and **23**, had K_ds in the same range as the derivatives of **6a**, the starting hits, equal to 18 and 10 μM, respectively, thus confirming the expected mechanism of inhibition by binding Interface 3 of TEAD surface. Only two compounds, **6g** and **10**, showing a clogP < 3, reported K_ds ~100 times higher than the more lipophilic compounds (clogP >3.14 for the derivatives of **6a**), suggesting that the specific pocket is very lipophilic in the phenyl-ring anchoring region on the TEAD surface, as showed in Fig. 7. A positive trend was observed, with a few exceptions, between the compounds' lipophilicity and K_d. This trend suggests that, as a general rule, the lipophilic surface of the protein binds preferentially to lipophilic compounds (**SI1-**Fig. S8).

2.8. Cancer cell growth inhibition studies

All compounds were screened, at first, at 40 μM on CRC and OC cells in comparison to **VP** and **IAG933.** The percentage of cell growth inhibition at 40 μM along with the measurable IC_{50} values are reported in Table 2 and Fig. 11A. **IAG933** is a selective and potent Y:T inhibitor to treat mesothelioma and other types of tumors, including colorectal cancer, that harbour alterations in RAS-MAPK pathways [33]. Noteworthy, CRC (HCT116) and OC (A2780, A2780/CP) cell models do not present these specific alterations as reported by the DepMap portal (https://depmap.org/portal/) and, indeed, do not respond to **IAG933**. The other CRC cell line we used, HT29, presents a mutation in the BRAF gene (BRAFV600E) [45], known to confer insensitivity to **IAG933** when this is administered alone (Fig. 11A). Cells were exposed to increasing concentrations, from 10 to 60 μM, of the compounds that were found most active at 40 μM and/or showed a K_d *vs* hTEAD4 below 10 μM. As

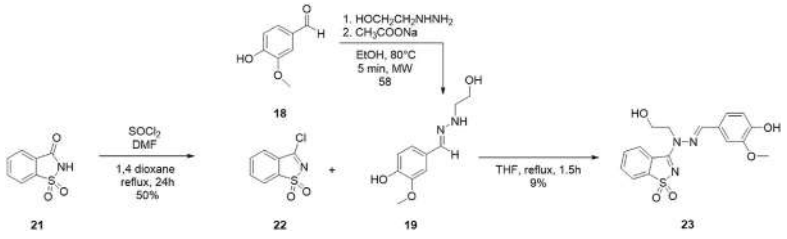

Scheme 4. Synthesis of 3-chlorobenzo[d]isothiazole 1,1-dioxide **22** and synthesis **23**.

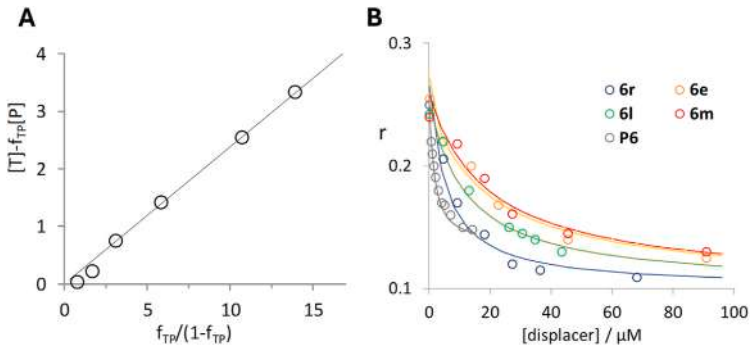

Fig. 9. **(A)** Graphical analysis of binding of P6-TMR to TEAD4. [T], [P] = total TEAD4, **P6-TMR** concentrations; f_{TP} = fraction of P6-TMR bound to TEAD4. The line represents the linear least-squares best fitting to the results of the titration of **P6-TMR** with TEAD4 based on measurement of the TMR fluorescence anisotropy (see the Materials and Methods for more details). **(B)** Fluorescence anisotropy (r) values obtained in displacement experiments of **P6-TMR** from TEAD4 caused by addition of four compounds and of untagged **P6**. The curves represent our best fittings of the data based on a model with two ligands (**P6-TMR** and the displacer) competing for the same binding site of TEAD4 [43].

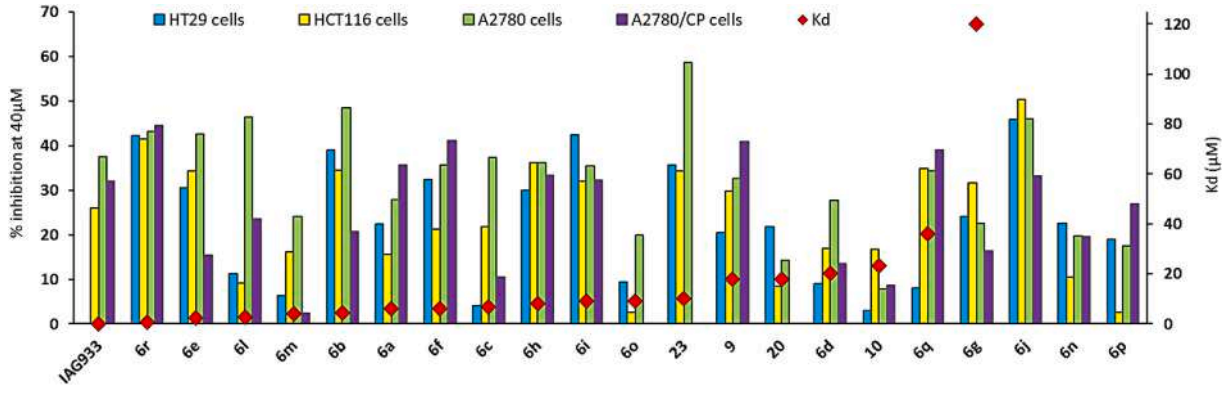

Fig. 10. Percentage inhibition of cellular growth (histogram, left Y axis) and K_ds (red diamonds, right Y axis) of the compounds displayed in the X-axis in the order of decreasing affinity/increasing K_d (red squares). The percentage inhibitions reported were measured at 40 µM on four cell lines: HT29 (blue), HCT116 (yellow), A2780 (green) and A2780/CP (violet). For compounds **6j**, **6n** and **6p**, it could not be possible to evaluate a K_d due to low solubility in the assay solvent.

Table 2
Calculated logP (clogP), K_d values (anisotropy assay), and percentage inhibition of cell growth at 40 µM on HT29, HCT116, A2780 and A2780/CP cell lines. IC_{50}, when measurable, is reported in parentheses with asterisks.

compound	clogP[a]	Anisotropy assay[b]	% of cell growth inhibition at 40 µM and IC50*			
		K_d (µM)	HT29	HCT116	A2780	A2780/CP
VS3(6a)	3.81	6.0 ± 1.2	22.4 ± 8.2	49.8 ± 10.0 (*41.7 ± 9)	36.6 ± 1.0 (*57.3 ± 6)	35.5 ± 7.0
6b	4.85	4.3 ± 0.9	38.9 ± 2.1	34.5 ± 10.4	48.5 ± 6.0	20.7 ± 1.9
6c	3.14	4.0 ± 0.8	21.8 ± 4.3	37.2 ± 5.0	10.5 ± 2.0	6.8 ± 1.2
6d	4.24	9.0 ± 1.8	16.9 ± 4.0	27.7 ± 3.0	13.8 ± 5.0	20.3 ± 3.0
6e	5.29	2.4 ± 0.5	30.4 ± 7.9	34 ± 20	42.6 ± 3.0	15.4 ± 6.2
6f	3.71	6.0 ± 1.2	32.3 ± 5.0	21.2 ± 5.0	35.5 ± 9.0	41.1 ± 4.0
6g	2.86	120 ± 24	24.0 ± 2.9	31.6 ± 4.0	22.6 ± 5.0	16.3 ± 2.0
6h	3.71	8.0 ± 1.6	30 ± 17	36 ± 15 (*61.8 ± 4.0)	36.8 ± 10	33.4 ± 6.0
6i	5.02	9.0 ± 1.8	42.3 ± 16.7	32.1 ± 6.0 (*83.7 ± 5)	35.5 ± 0.4	32.1 ± 3.1
6j	4.60	No fitting	45.8 ± 23.8 (*60.3 ± 11)	35.3 ± 13 (*56.8 ± 6)	46.1 ± 5.0 (*60.2 ± 7)	33.1 ± 9.0
6k	4.99	5 ± 1	21.9 ± 1.8	3.8 ± 2	18.7 ± 2.8	2.1 ± 1.0
6l	5.28	2.7 ± 0.5	11.3 ± 3.7	9.1 ± 1	46.3 ± 23.5	23.5 ± 4.0
6m	4.99	4.0 ± 0.8	6.4 ± 3.6	16.2 ± 8.0	23.9 ± 7.2	2.4 ± 1.0
6n	4.87	No fitting	22.6 ± 2.4	10.5 ± 1.3	19.8 ± 4.3	19.6 ± 7.0
6o	3.27	9.0 ± 1.8	9.3 ± 3.1	2.6 ± 1.3	20.0 ± 3.3	19.8 ± 1.0
6p	4.73	No fitting	18.9 ± 1.2	2.6 ± 1.6	17.4 ± 1.0	26.9 ± 3.0
6q	4.41	8.0 ± 1.6	35 ± 14	34.2 ± 3.0	38.9 ± 14.7	36.1 ± 7.3
6r	4.16	0.6 ± 0.1	42.2 ± 2.0	41 ± 25	43 ± 22	44 ± 27
9	3.35	18.0 ± 3.6	20.5 ± 6.0	30 ± 18	32 ± 16	41 ± 12
10	2.88	150 ± 30	16.7 ± 2.3	7.8 ± 2.1	8.6 ± 1.2	23.2 ± 3.0
20	2.08	18.0 ± 3.6	21.8 ± 1.4	8.4 ± 3.3	14.3 ± 4.1	10.5 ± 2.6
23	2.82	10 ± 2	35.6 ± 4.2	34 ± 21	58.7 ± 10.6	38.1 ± 1.2
IAG933	3.82	0.01 ± 0.005	–	26 ± 5.2	37.5 ± 7.5	32.5 ± 6.4
VP	4.58	ND[c]	68.9 ± 2.0 (*22.5 ± 4)	*10.1 ± 5.0	57.3 ± 6.0 (*39 ± 7)	*11.9 ± 3

[b]estimated error, ±20 %. [c]ND = not determined because of spectral interference.[a] calculated from Chemdraw V22.2.

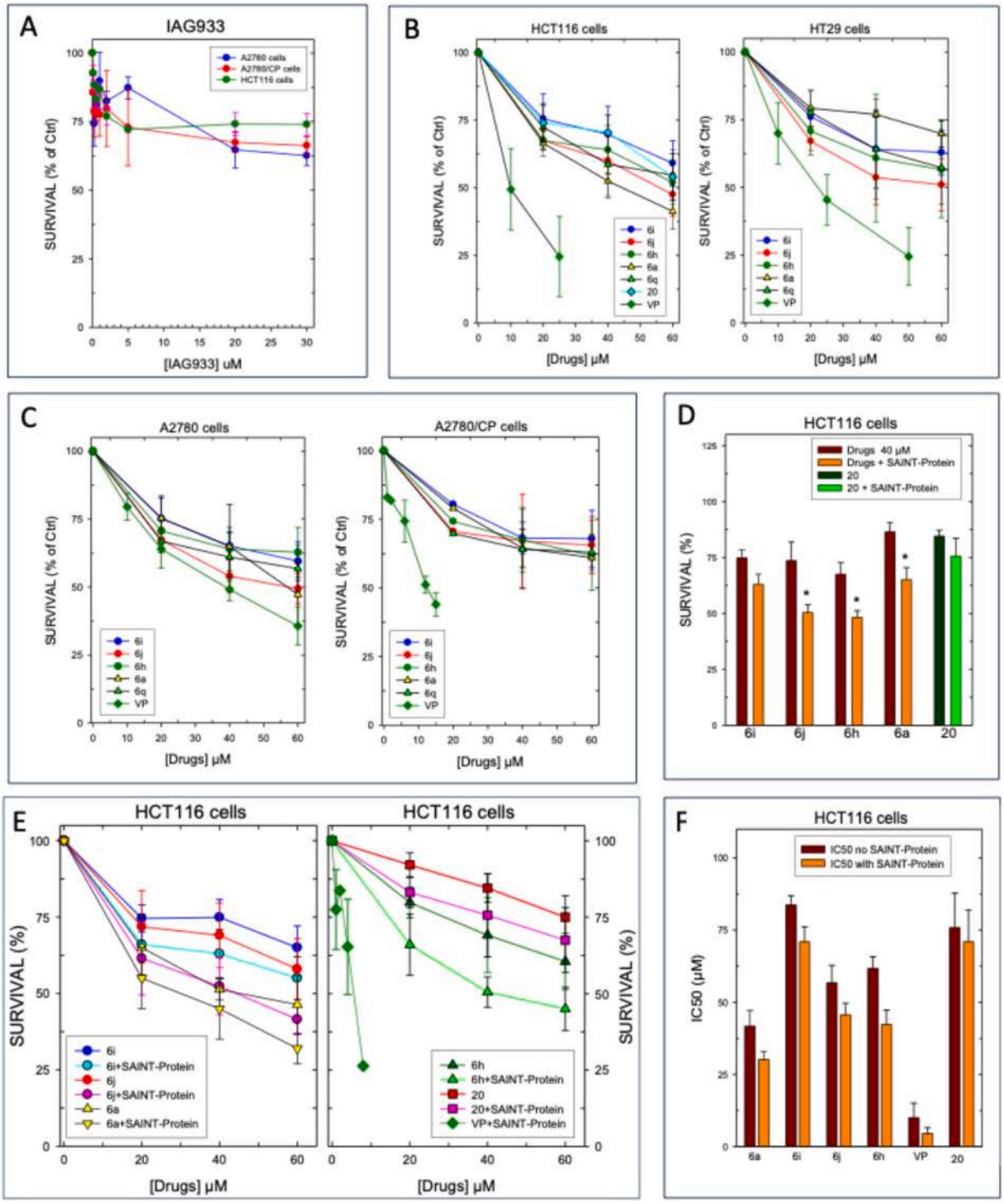

Fig. 11. **(A)** Dose-response curves of **IAG933** after a 72 h exposure to HCT116, A2780 and A2780/CP cell lines. Cell survival rates are mean ± S.D. of two separate experiments performed in duplicate. (**B,C**) Survival of HCT116, HT29 CRC, A2780 and A2780/CP OC cell lines after 72h-treatment with the selected compounds: **6i**, **6j**, **6h**, **6q**, **6a**, **20** and **VP**. Error bars, mean ± S.D. from at least three experiments performed in duplicate. (**D**) HCT116 cell survival after transfection with SAINT-Protein of the reported compounds at 40 μM. Error bars, mean ± S.D. from at least three experiments performed in duplicate. **(E)** HCT116 cell survival dose-response curves after transfection with compounds **6i**, **6j**, **6a** with/without SAINT-Protein (left), **6h**, **20**, **VP** with/without SAINT-Protein (right). Error bars, mean ± S.D. from at least three experiments performed in duplicate. Error bars, mean ± S.D. from at least three experiments performed in duplicate. (**F**) Histogram showing IC_{50} of **6a**, **6i, 6j, 6h** compared to **VP** and **20** in HCT116 cancer cells. Error bars, mean ± S.D. from at least three experiments performed in duplicate.

reported in Tables 2 and in Fig. 11B–E, **6a**, **6h** and **6j** showed 35–50 % growth inhibition at 40 μM against some of the cell lines. Compound **6i** proved to be the least active on all four cell lines, reaching approximately 40 % maximum inhibition only at 60 μM. All the other compounds showed similar behaviour, particularly on OC cell lines, although they were slightly more cytotoxic. On the contrary, compounds **6a**, **6j**, **6q** and **6r** showed greater efficacy on all four cell lines, especially on CRC cells. **6a** and **6j** also showed response curves closer to that of the reference compound, **VP**, and also reaching, in this concentration range, the IC_{50} values in at least two out of four cell lines (Table 2). A2780/CP

cells proved to be the least responsive of the four cell lines tested. The cisplatin-resistance phenotype also makes these cells more cross-resistant to these compounds, except for **VP** (Fig. 11C). Some of the tested compounds, bearing various substituents at the *ortho* and *para* positions of ring C and at the *ortho* positions of ring B (see Fig. 7C), were selected for further experiments. Compounds **6a** and **6h** are characterized by a methyl or a nitroso group at the *ortho* position of ring C, respectively, while compounds **6i** and **6j** present a *tert*-butyl substituent at the *para* position of ring C. Two additional compounds, **6q** and **6r**, showed about 40 % cell growth inhibition, but no IC50 could be measured due to solubility issues; only **6q** was selected.

To favor internalization of the tested compounds, i.e., to increase their intracellular concentrations, the delivery system SAINT-Protein (Synvolux Therapeutics, NL) was adopted with compounds **6a, 6h, 6i, 6j** and **20,** as compound of reference, on HCT116 cancer cells. **VP** was adopted as compound for comparison because it shows a different mechanism of action in cancer cells, by acting on LATS preventing YAP phosphorylation and translocation to the nucleus [46]. This non-liposomal transfection reagent does not form micelles, but wraps suitable compounds and releases them inside cells without involving the endosome. It was developed to deliver peptides into cells and, to this aim, was extensively used in previous experiments to transfect tumour cells [47]. Based on this experience, the system was adapted and optimized to deliver small synthetic molecules by facilitating their crossing of the plasma membrane. We found that the optimal ratio of drug solution volume to SAINT-Protein volume (which alone showed a cellular cytotoxic effect lower than 5 %) was approximately 1:4, a quarter of the volume recommended by the manufacturer. Increasing concentrations of the compounds were added while maintaining a constant volumetric ratio between the drug solutions and the transfectant for both cytotoxicity and RT-PCR experiments. After 72 h from the administration of the compounds at different concentrations, cell growth inhibition was evaluated by the crystal violet dye assay. Fig. 11D shows that the cytotoxicity of compounds **6i** and **20** increased by about 10 %, (IC_{50} 71.1 ± 9 and 70.2 ± 8 μM respectively) whereas the transfection of **6a**, **6h** and **6j** with the SAINT-Protein caused an increase of cell growth

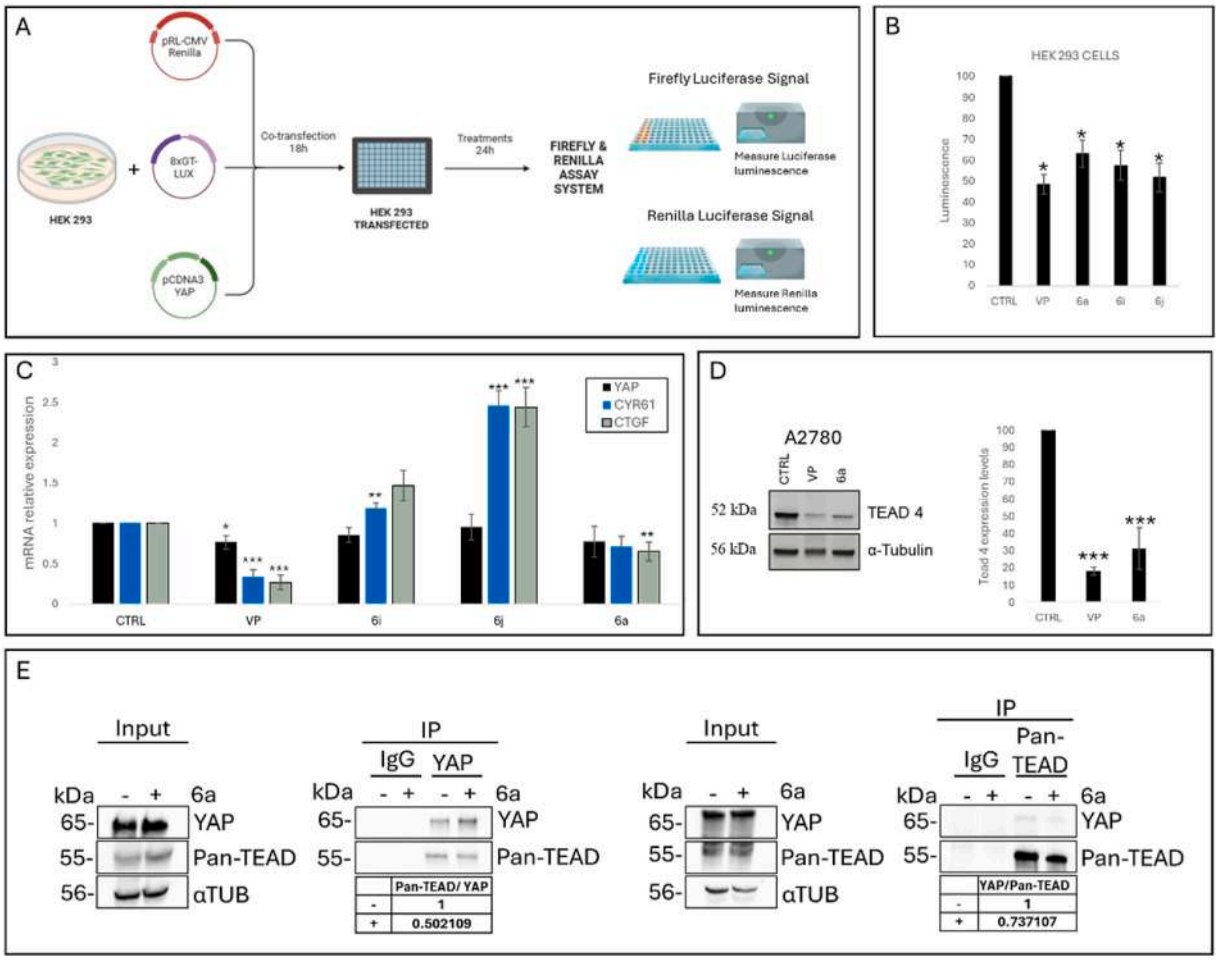

Fig. 12. Inhibition of YAP-TEAD transcriptional activity and disruption of the endogenous YAP-TEAD association in cells. (**A**) Workflow of Dual-Glo Luciferase Assay on HEK 293 cells. **(B)** Luciferase assay data represented by the reduction of the luminescence signal with respect to the control for compounds VP, **6a, 6i** and **6j**. Raw numerical data associated with Fig. 12B are reported in **SI1**-Table S6. (C) YAP mRNA and its target genes levels after 48h of treatment in HCT116 by real-time RT-PCR assays for compounds **6a, 6i** and **6j**. **VP** was used as a compound for comparison. Black bar: YAP gene expression levels, blue bar: CYR61 gene expression levels, grey bar: CTGF gene expression levels. Data indicate mean values and standard deviation of biological repeats performed in triplicate. Associated *p*-values were calculated with a two-sided Student's t-test (*$p < 0.05$; **$p < 0.01$; ***$p < 0.001$). The table with numeric data, referring to Fig. 12C, is reported in SI1-Table S7. (**D**) Representative Western blot and quantification histogram for TEAD 4 expression levels in A2780 cells after **6a** and **VP** treatment. The numeric data referring to Fig. 12D is reported in **SI1**-Table S8. Tubulin has been used as a housekeeping protein. The bands obtained by immunoblot were analyzed by ImageJ (Java-based image-processing and analysis software). *p*-values were calculated with a two-sided Student's t-test (***$p < 0.001$). (**E**) Co-immunoprecipitation after an 8-hr incubation of HCT116 cells with DMSO (−) or **6a** (+). Endogenous TEAD co-immunoprecipitation with a YAP antibody (left, quantification of ratio Pan-TEAD/YAP on the bottom); endogenous YAP co-immunoprecipitation with a Pan-TEAD antibody (right, quantification of ratio YAP/Pan-TEAD on the bottom). **6a** is capable of disrupting the YAP-TEAD interaction.

inhibition by about 20–25 % (30.2 ± 3, 42.3 ± 5 and 45.7 ± 4 μM respectively). Use of the SAINT-Protein decreased the IC_{50} of **VP** below 10 μM. The dose-response curves and percentage survivals at 40 μM in Fig. 11F confirm that administration of the compounds in the presence of the SAINT-Protein transfectant enhances their effectiveness at various concentrations [48].

2.9. Pyrazolo-piperidinone derivatives inhibition of YAP-TEAD transcriptional activity and disruption of the endogenous YAP-TEAD association in cells

The compounds showing the most interesting properties, such as K_d below 10 μM and measurable IC_{50} values, were first assayed for their ability to inhibit TEAD-dependent transcriptional activity in cells. **6j** showed a high lipophilicity that prevents the detection of K_d. Luciferase assays were performed in HEK293 cells. To this aim, after treatment with **6i**, **6j**, **6a**, cells were co-transfected for 18 h with pRL-CMV Renilla, 8xGT-LUX, and pCDNA3–YAP. Then, they were treated with **6i** (80 μM), **6j** (55 μM), **6a** (60 μM), and **VP** (12 μM). The compounds under examination were tested for a treatment duration of 24 h. The luciferase bioluminescence signal intensity was reduced in cells treated with **6i**, **6j**, **6a**, and **VP** compared to vehicle-treated cells (Fig. 12A and B), demonstrating their ability to inhibit TEAD activity in cells. Notably, all compounds tested at their IC_{50} concentration resulted in a similar decrease of the luminescence signal, ranging from 40 to 50 %.

To understand whether the cell growth inhibition reported in Fig. 11 could relate to the suppression of TEAD-related genes, RT-PCR studies were conducted on HCT116 cells treated with compounds **6a**, **6i** and **6j**. Indeed, we found that, in these cells, compound **6a** at 60 μM inhibited TEAD related transcriptional activities in real-time RT-PCR assays (48 h), as shown by the reduction of the expression of two target genes crucial for colon cancer progression, namely, CTGF, also known as CCN family member 2 (CCN2) or connective tissue growth factor [49], and CYR61, the cysteine-rich angiogenic inducer 61 or CCN1 [50] (Fig. 12C). CTGF has important roles in many biological processes, including cell adhesion, migration, and proliferation, and is critically involved in several forms of cancer. CYR61 is involved in a broad range of cellular activities, including cell adhesion, migration, proliferation, differentiation, apoptosis, and senescence. An increase of the CTGF and CYR61 expression was unexpectedly observed after **6i** (at a concentration of 80 μM), and **6j** (at a concentration of 55 μM) treatment (Fig. 12C). **VP** (12 μM), showed reduced expression of both CTGF and CYR61 in agreement with previous results.

Since YAP:TEAD inhibitors are expected to lower TEAD levels [57], we investigated if our new TEAD inhibitors would do the same. Fig. 12D shows that starting compound **6a** decreased TEAD4 protein levels in A2780 cells, similar to the known effect of VP.

To investigate whether our compounds may impair YAP-TEAD interaction in cells, we set up an endogenous co-immunoprecipitation (Co-IP) experiment to monitor YAP-TEAD interactions in the presence of the **6a** compound. Notably, 8 h of treatment of HCT116 cells with **6a** significantly decreased endogenous TEAD co-immunoprecipitation with a YAP antibody (Fig. 12E, left). Remarkably, the ability of **6a** to disrupt the YAP-TEAD interaction was also demonstrated by a reversed co-immunoprecipitation assay. This approach is beneficial for verifying interactions, especially when one protein (TEAD) is suspected to be present at a significantly lower concentration compared to the other protein (YAP). As demonstrated in Fig. 12E, right, **6a** decreased endogenous YAP co-immunoprecipitation with a pan-TEAD antibody.

2.10. Whole cell LC-MS/MS proteomics

To better understand the intracellular mechanism of action of the tested compounds and to integrate the information obtained from the cell growth inhibition experiments and cell biology, the total proteome modulation induced by compounds **6a**, **6i** and **6j** in comparison with **VP** was quali-quantitatively characterized in HCT116 cells. Herein, by reducing TEAD transcription with Y:T complex formation inhibitors, a downstream effect is expected in the modulation of the metabolic network, recorded as up/down expression of certain protein levels. The compounds were selected due to their capacity to give a measurable IC_{50} against HCT116 other than showing a low micromolar K_d for the target protein. For this experiment, the SAINT-Protein delivery system was used to more efficiently deliver the compounds intracellularly and favor cellular uptake (Fig. 11B).

HCT116 cells treated with the compounds and SAINT delivery system were submitted to protein digestion and LC-MS/MS analysis was performed with Proteome Discoverer v.3.0. The differential protein analysis (one-way ANOVA) defined each protein by a fold change (FC, i.e. level of expression *vs* the control) and a signficance value (*q*-value). A protein with a FC $\geq$ 1.0/$\leq$-1.0 and a *q*-value <0.05 is considered as significantly differentially expressed (DEP), and DEP's were considered for further bioinformatics characterization, as associated with the compound treatment. The following differential analyses were performed: *i.* DEPs obtained with the delivery system alone versus untreated HCT116; *ii.* DEP's from **VP** treatment; *iii.* **6a**, **6i** and **6j** compounds and non-treated cells as reference; *iv.* biological pathway analysis from DEPs analysis of all compounds and **VP**. The SAINT-Protein control analysis with respect to untreated set was named 'control system' (**Δc** set). As shown in **SI1**-Fig. S9, the enriched STRING network obtained with the DEPs from this differential analysis enhanced only two pathways, GO:009902, Vesicle tethering and GO:0006901, Vesicle coating. DEPs identified from this analysis are reported in **SI1**-Table S9. The SAINT-Protein effect is consistent with the mechanism of action of the delivery system involving lipid and vesicular transportation. The limited effect of the delivery system on protein modulation, supported the use of the delivery system to load the TEAD4 inhibitors without significantly affecting the proteome and the TEAD function. Then, the samples from the different treatments were analyzed independently. Results from the ANOVA test showed a total number of proteins per sample in the range of 5250–5500, giving a total number of proteins identified around 20.000, with a FDR (false discovery rate) < 5 % (Storey-Tibshirani procedure for *p*-value correction) for each comparison. The analysis resulted in 129 DEPs for the treatment with **VP**, 49 for **6a**, 122 for **6j**, 82 for **6i**. The total quantified proteins and DEPs per each differential analysis are reported in **SI1**-Table S10. The obtained Volcano-plots (V-plots) from the MS differential analyses are reported in Fig. 13.

2.11. Proteome analysis of HCT116 cells treated with VP

The differential analysis between **VP**-treated cells and **Δc** set data are reported in the **Supplementary Information 6**. Results from the protein non-enriched analysis indicates that **VP** inhibits PDL5 (programmed cell death protein 5), which is already reported in the literature as one of the down-regulated key proteins [51]. Additionally, the Ubiquitin-conjugating enzyme E2 G1 (P62253) (FC -2.86), its variant 1 (Q13404) (FC -2.87), Ubiquitin E2 L3 (P68036 FC -2.04) and E2 N (P61088 FC -2.06) resulted significantly down-regulated with respect to the control samples. Protein 14-3-3σ (P31947) results 1.2-fold up-regulated with respect to control (Fig. 14A). The local DEP network for **VP**, obtained with non enriched STRING analysis, including TGF-β1 is illustrated in Fig. 14B where the connection with the ubiquitination proteins is higlighted. This outcome is in agreement with the expected **VP** mechanism to promote 14-3-3σ protein transcription, which consequently results in an increased YAP cytosolic sequestration [52] and decrease in TEAD transcription. All these findings are consistent with **VP** mechanism of action and support the MS proteomic methods applied.

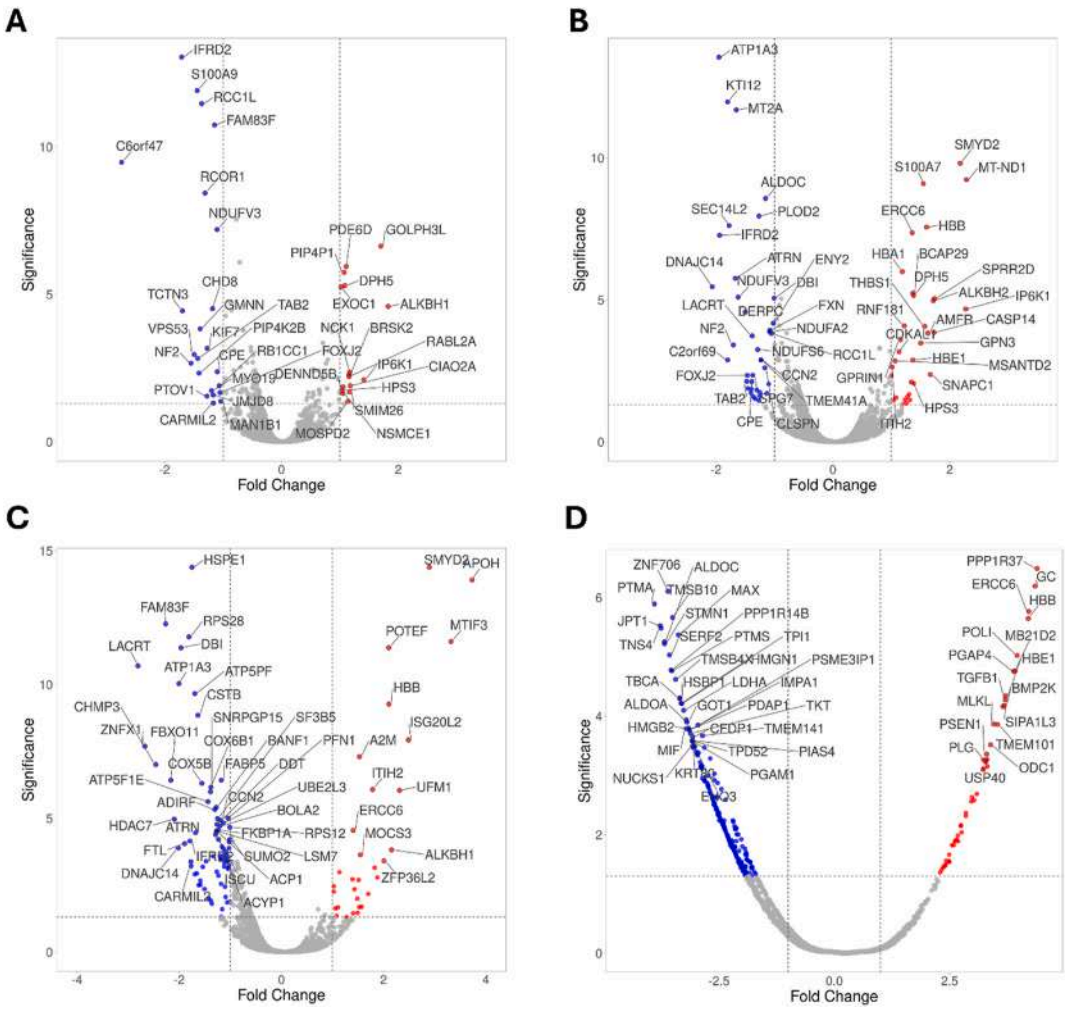

Fig. 13. Volcano Plots representing the differential analysis between each treatment and the control cells (**A**) **6a**, (**B**) **6i**, (**C**) **6j**, (**D**) **VP**. Significantly up-regulated proteins are represented in red, significantly down-regulated proteins are represented in blue (significance>1.3, expressed as -log(10) *q*-value, FC ≤ -1 and FC ≥ -1) Both non-significant protein (<1.3) and significant proteins which are not up/down regulated (significance >1.3, $-1 \leq$FC ≤ 1) are represented in grey dots. FC = $\log_2$(ratio)). Y-axes: significance is the -log(10) of the *q*-values associated with the DEPs from the adjusted *p*-test.

2.12. Proteome analysis of HCT116 cells treated with 6a, 6i and 6j

The comparative analysis among treated samples and controls evidenced that five DEPs are significantly differentially down-regulated by **6a, 6i** and **6j**, with the same trend of expression. Indeed, carboxypeptidase E (CPE), RCC1-like G exchanging factor-like protein (RCC1L), interferon-related developmental regulator 2 (IFRD2), Na/K ATPase subunit alpha-3 (ATP1A), and attractin (ATRN) are all down-regulated with respect to **Δc**, whereas prolargin (PRELP) is up-regulated. Their expression levels are represented in Fig. 14C, in the Venn diagram in **SI1**-Fig. S10, and described in **SI1-**Table S11. Because the DEPs are not apparently involved in HP signalling, we explored the dependence of HCT116 cell growth on their corresponding gene expression examining the effects of its depletion in DepMap. DepMap is a publicly available dataset of 1032 cells in which the gene has been knocked out by CRISPR/Cas9 [54]. The repository is able to compute the importance of a gene on cell survival based on the CHRONOS score, an algorithm that allows the prediction of gene importance in the specific cell lines [55]. The lower the score, the more important the gene involvement in cell death/cytotoxicity: 0.5 represents depletion of the corresponding transcripted protein in most cell lines, while less than −1 represents certainty that the gene knock-out results in cell killing. On the other hand, a higher score stands as important for cell vitality [55]. When comparing the 6 mutual DEPs (Fig. 14D), four of them resulted non significant for cell survival (CPE, ATP1A, ATRN, PRELP). IFRD2 is highly expressed in colorectal cancer, and its down-regulation indicates a favourable effect on cell growth inhibition. RCC1L, whose action results in decreased translation, is correlated with cytotoxicity mechanisms after compound administration. (Fig. 14C).

Comparative analysis (DEP's analysis) among **6a**, **6i**, **6j** and **VP** showed that connective tissue growth factor CTFG (or CNN2), one of the known TEAD4 target genes, results significantly down-regulated (Fig. 14E). Cells treated with **6a** did not reveal a significant modulation of CTGF (**SI6**). *TGF*-β1 (transforming growth factor beta 1) is one of the multi functional cytokines belonging to the transforming growth factor superfamily. Once activated, it acts as serine/threonine kinase able to bind TGF-β receptors, stop cells replication in the G1 phase and induces differentiation [56]. In the analyzed samples, down-regulation of *TGF*-β1 after administration of **VP**, **6j** and **6i**, but not of **6a** was observed (Fig. 14E). Interestingly, E3 ubiquitin-protein ligase AMFR (Q9UKV5) was significantly overexpressed in **6i-**treated cells, but not by treatment with **VP** or **6a** and **6j**; the latest compounds caused an over-expression of the ubiquitin-conjugating enzyme E2 L3 (P68036). The observed up-regulation of the proteasome assembly machine is connected to the hyperactivation of the ubiquitination process that leads to YAP/TAZ degradation in the cytosolic environment [57].

To summarize, the comparison between the proteins identified in the Volcano plot and those differentially espressed in the DEPs analysis,

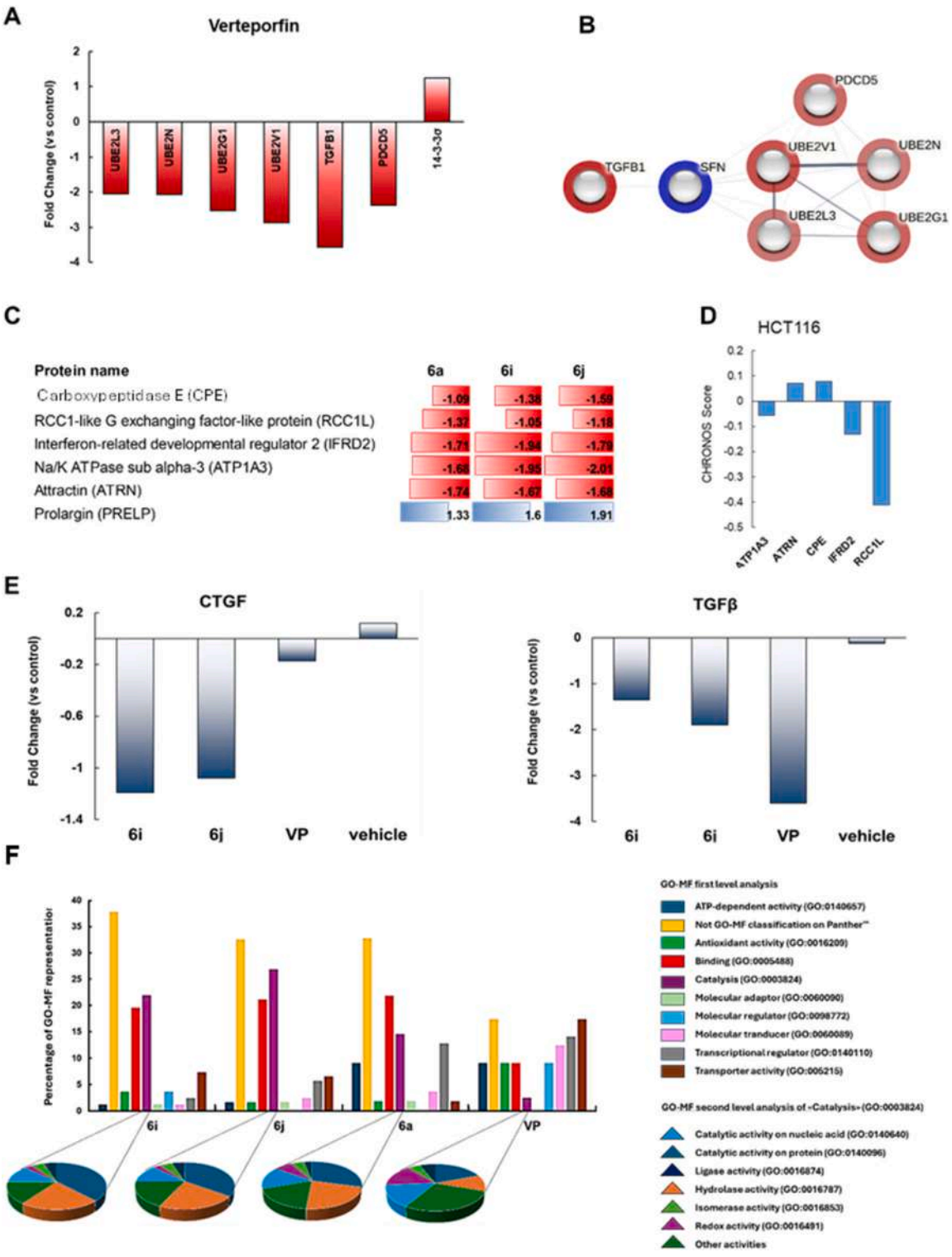

Fig. 14. **(A) VP** DEPs analysis. Fold Change (FC), expressed as $\log_2$ of protein abundance ratios between treated samples and the **Δc** group. The expression of the main DEPs is discussed in the results section. **(B)** Main local networks (**VP**) emerging from the first level enrichment analisys of TFG-β1 and the ubiquitination proteins. The two main GO's (Biological Processes) are GO:1902523 (Positive Regulation of protein K63-linked ubiquitination, p = 0.0051) and GO:0070534 (Protein K63-linked ubiquitination, $p = 0.00042$). **(C)** Fold-change of the six proteins shared by **6a, 6j** and **6i**, identified by the Venn Diagram in (**SI1-**Fig. S10 and **SI1-**Table S11) **(D)** CRISP/Cas9 knock out analysis of the five genes corresponding to the proteins in Fig. 14C expressed with CHRONOS score on DepMap tool. **(E)** Fold-change of the proteins shared by **6j**, **6i** and **VP**. These include Connective Tissue Growth factor (CTGF/CCN2) and Transforming growth factor (TFG-β1) expressed as FC with respect to the **Δc** samples. **(F)** Histogram representation of the most significant biological pathways represented as GO-MF's (Molecular Function) associated to each treatment from the DEP's analysis. The histogram was obtained with PANTHER v18.0 by imputing, for each differential analysis, the emerged DEPs and the outcome values normalized to a percentage [53]. A second-level analysis (GO-MS[2]) was performed on the entry (GO:0003824) containg protein characterized by catalytic activity, since it represents the most abundant first-level GO-MF clustering class (**SI1** pag 38).

show some differences. While the Volcano plot shows the independent effect of each compound on the protein modulation (Fig. 13), the DEPs analysis, obtained thorugh a comparative analysis among different compounds (**6a**, **6i**, **6j**) and the reference drug (**VP**), provides information about the modulation of specific proteins and enhance the difference in the mechanism of action between **VP** and the pyrazolo-piperidineone compounds. All the compounds studied modulate some common specific proteins, such as CTGF, TGF-β1 and proteasome proteins.

The results from the transcript analysis, generally confirmed the data observed in the MS analysis for **VP**. The transcript analysis shows that the known target genes CTGF and CYR61 other than YAP total proteins are downregulated in the case of **6a** as it is observed for **VP**.

After the protein analysis, a non enriched metabolic pathway analysis was performed using different softwares and the GO database. The GOs analysis performed on STRING from the DEPs of the treated samples evidenced a strong similarity among the pathways emerged from the treatments with **6a, 6i** and **6j**. Indeed, aerobic electron transport chain (GO:0019646), mitochondrial ATP synthesis coupled electron transport (GO:0042775), nucleobase-containing compound biosynthetic process (GO:0034654) and regulation of collagen biosynthetic process (GO:0032967) emerged as significant networks (FDR <0.05) in all three treatments. On the other hand, GO analysis of cells treated with **VP** evidenced none of these pathways. The first level networks generated with the DEPs and their corresponding emerged GOs are reported in **SI1**-Figure S11-S14.

This analysis was cross validated by a cellular-function gene analysis on the PANTHER suite [53,58] to map the most involved GO- Molecular functions (GO-MF's) (Fig. 14F). Compounds **6a, 6i** and **6j** display many proteins belonging to process involved in the "catalytic activities" (GO:0003824), and "binding" (GO:0005488) (Details in Supplementary Information 1 pag S38). On the other hand, **VP** is mainly represented by "molecular transducer" (GO:0060089), "transcription regulatory activity" (GO:0140110) and "transporter activities" (GO:0005215) functions. Even a second level GO-MF's on the sub-classification of the most abundant primary GO (i.e. catalytic activities GO:0003824) confirms the evident difference in the proteome modulation between the novel inhibitors and **VP**. For the Y:T disrupters, "catalytic activity on proteins" (GO:0140096), and "hydrolases" (GO:0016787) are mainly regulated, while for **VP** the main 2nd level GO-MF's is represented by "other activities", including demethylase activity (GO:0032451), cyclase activity (GO:0009975), lyase activity (GO:0016829).

Overall, despite the MS proteomic analysis did not identify TEAD4 among the DEP's, the levels of expression of the downstream proteins regulated the by Y:T system are consistent with the expected mechanism of action of the compounds, and prove their ability to impair the HP signalling. Also, the direct comparison with **VP** treated cells evidences that the same mechanisms of action is shared by compounds **6a, 6i** and **6j. VP,** instead modulate a different biochemical pathway is, that is known to act upstream of the HP.

3. Conclusions

Our integrated virtual screening and experimental validation studies identified novel pyrazolo-piperidinone derivatives that target the YAP-TEAD Interface 3 surface. Compound **6a**, identified through virtual screening, was recognized as an interesting hit for further medicinal chemistry studies. Structure-activity relationship (SAR) analysis of the designed compound library indicates that hydrophobic or slightly polar substituents on ring C of the scaffold are tolerated or can improve affinity for TEAD.

The initial compound **6a** and its derivatives **6i** and **6j** exhibited a moderate but specific anti-TEAD profile in both target-based and cellular experiments. These compounds also showed antiproliferative activity in colorectal and ovarian cancer cells, including those resistant to the KRAS-dependent inhibitor IAG933.

Using a whole-cell proteomic approach, we demonstrated that these compounds, unlike verteporfin, directly engaged TEAD4, leading to the downregulation of downstream effectors such as CTGF and TGF-β1. They also induced a distinct proteomic profile, indicating modulation of the Hippo pathway via TEAD. Overall, this work led to the identification and validation of a novel series of compounds. This study positions pyrazolo-piperidinones as promising TEAD4 inhibitors with a unique biological impact, opening avenues for further hit-to-lead optimization and detailed mechanism of action studies.

4. Experimental section

4.1. Molecular modeling

4.1.1. Preparation of the models

The X-ray structures of YAP1-TEAD1 complex (3KYS.pdb, chain D and C) [10] of TEAD4 in complex with linear peptide (6Q36.pdb, chain A and C) [11] were prepared using the Protein Preparation Wizard tool within the Schrodinger suite by applying the OPLS2005 force field [59]. Missing hydrogen atoms were added; orientation of thiol and hydroxyl groups of amino acids, and the conformation of histidine residues were modelled to maximize the hydrogen-bonding network. Acid and basic amino acids were modelled in their charged forms. All the models were then energy-minimized with OPLS2005 force field restraining the position of heavy atoms to a RMSD value of 0.3 Å. The crystal structure of TEAD4 in complex with Compound **4** (8CAA.pdb [32]) is characterized by a gap affecting residues 251 to 259, which form a loop in close contact with the Interface 3. The three-dimensional structure of this region is solved in the crystal structure of TEAD4 in complex with the linear peptide (6Q36.pdb). With the exception of the side chain of Lys297, Interface 3 of these two crystal structures is highly superimposable (RMSD calculated for Cα atoms of 0.36 Å). Starting from the coordinates of 6Q36, a model of TEAD4 was thus prepared by manually modifying Lys297 side chain and by reproducing the binding mode of Compound **4**. The resulting model was then energy-minimized with OPLS2005 restraining the position of the backbone heavy atoms to a RMSD value of 0.3 Å, and used to model an alternative binding pose of compound **VS3 (6a)**, similar to the binding mode of Compound **4**. A model of the cyclic macro peptide 17 was prepared in Maestro and docked on the surface of TEAD1 (3KYS.pdb) and the complex was submitted to MD simulation following a procedure described in the supplementary information (**SI1**-Fig. S1).

4.1.2. Filtering and preparation of the chemical libraries

The ChemDiv library was preliminary filtered to exclude highly reactive compounds; PAINS (pan-assays interference compounds) [60] and Michael acceptors were filtered out. A filter on molecular weight was also imposed to exclude compounds characterized by a low molecular weight. Compounds with a molecular weight value within 100 and 900 were retained. The filtered compounds were prepared using the LigPrep, and Epik was used to assign the protonation state of basic and acid groups at physiological pH [61,62]. Chirality of ligands was maintained when specified, while all the possible stereoisomers were generated for all the other compounds. Salts and any other cofactor molecules were removed. This protocol allowed to obtain 349,510 compounds starting from an initial set of 450,989 prepared compounds.

4.1.3. Pharmacophore models

A first pharmacophore model was built using Phase starting from the coordinates of the cyclic macro-peptide modelled on the surface of TEAD1 and equilibrated *via* MD simulation. Three different pharmacophoric features were generated, comprising *i.*) a hydrogen bond acceptor, corresponding to the serine residue of the peptide; *ii.*) an aromatic ring corresponding to the *m*-chlorophenylalanin ring of the peptide; *iii.*) an hydrophobic feature corresponding to the Cl atom of the *m*-chlorophenylalanin residue of the peptide. Matching of all the

pharmacophoric features was imposed. A second pharmacophore model was built from the X-ray coordinates of the linear peptide co-crystallized on the surface of TEAD4. Three different pharmacophoric features were generated, comprising *i.*) a hydrogen bond acceptor, corresponding to the serine residue of the peptide; *ii.*) an aromatic ring corresponding to the 6-chloroindole ring of the peptide; *iii.*) an hydrophobic feature corresponding to the Cl atom of the 6-chloroindole residue of the peptide. Matching of all the pharmacophoric features was imposed. The screened compounds were ranked according to their fitness score, which is a linear combination of the site and vector alignment score and gives a measure of how well specific conformations of the compounds match the pharmacophore hypothesis.

4.1.4. Docking studies

Docking studies were performed using Glide [63,64]. Docking grids were prepared starting from the X-ray structures of *h*TEAD1 (3KYS.pdb) and *h*TEAD4 bound to a linear peptide (6Q36.pdb). The grids were centered on the coordinates of residues Lys289, Glu383, Val406 and Tyr421 of hTEAD1, corresponding to Lys297, Glu391, Val414 and Tyr429 in hTEAD4, seeting the dimensions of the inner and outerboxes to 14 Å and 34 Å, respectively. Default settings were applied in the Glide standard precision (SP) mode. The binding modes of compounds were ranked according to the predicted affinity (Gscore).

4.1.5. Shape similarity screening

A shape similarity screening was performed using Phase [65]. A portion of the YAP Ω-loop was used as template molecule, adjusting the residues weights to set a higher relevance for the side chains of residues M86, L91, F95 and S94. The shape similarity search was performed on the MacroModel atom types. The shape similarity was computed as a function of the overlap between the template and the ligands.

4.1.6. Definition of a consensus score and cluster analysis

The Consensus score was defined taking into account the fitness score, the shape similarity, the Gscore and the molecular weight as follows:

$$Consenus\ score = X_{fitness} \times X_{shape\ similarity} \times X_{Gscore}$$

Where:

$$X_{(term)} = \frac{(X - X_{min})}{(X_{max} - X_{min})}$$

3000 top-ranked compounds according to the Consensus score were clustered by applying a top-down approach to identify 100 lead compounds. Linear hashed fingerprints were used, and the Tanimoto metrics was used to cluster the compounds. 50 compounds with the highest Consensus score were selected for biological evaluation.

4.1.7. Molecular dynamics of the complex TEAD4 - VS3

The best binding mode according to the Gscore of compound **VS3** docked on the surface of TEAD4 was submitted to molecular dynamics simulation, following a minimization within the OPLS4 force field using Macromodel keeping the α carbon atoms of the protein fixed. The system was solvated into a simulation box of 40 Å × 98 Å × 93 Å by adding TIP3P water molecules and neutralized by adding 6 Na^+ ions. Following a brief equilibration, the system was submitted to 500 ns-long or 250 ns-long MD simulations in the NVT ensemble setting the temperature to 300 K. To assess the stability of the protein ligand complex, the RMSD of TEAD4 and of the ligand was evaluated (**SI1-**Fig. S6).

4.2. Synthesis and characterization of compound 6a derivatives

Unless otherwise specified, all reagents were obtained from commercial sources (Sigma Aldrich, Merck, Fluorochem, BLD, ABCR) and used without further purification. The reactions were monitored by thin layer chromatography (TLC) with 0.20 mm EMD/millipore silica plates (60-F254), using UV light (λ = 254 nm) as developing agent, Cerium Ammonium Molybdate (CAM), followed by a short heating with a heat gun. The ^1H and ^{13}C NMR spectra were recorded with a Bruker DPX-400 spectrometer or with a Bruker FT-NMR Avance III HD 600 MHz. The chemical shifts are reported on a δ scale with solvent residual signals as internal references ($\delta_H = 7.26$, $\delta_C = 77.16$ CDCl3; $\delta_H = 2.50$, $\delta_C = 39.52$ DMSO–d6). Two-dimensional NMR techniques (COSY, HSQC, HMBC) were employed for signal assignment in the ^1H and ^{13}C spectra. The chemical shifts are expressed in ppm (s = singlet, d = doublet, t = triplet, q = quartet, dd = double doublet, m = multiplet, br = broadened signal); the coupling constants (J) are expressed in Hz. High-resolution mass spectra were obtained using MeOH as solvent and Thermo Fisher HPLC-MS UltiMate 3000 mass spectrometer, with hybrid Q Exactive quadrupole – HESI-II electron spray orbitrap mass analyzer. Purity was determined using a HPLC-UV/Vis (Agilent Infinity II). Chromatographic separation were carried out on a RP Kinetex 2.6 μm Biphenyl 100 Å maintained at 30 °C. The separation was performed under gradient conditions using solvent A t0 95 %–5 % over 22 min at a flowrate of 1 mL/min. Eluent A (H_2O +0.1 % Formic acid), eluent B (ACN +0.1 % Formic acid). The separation was monitored using wavelengths of 254 nm and 280 nm. Purity detection was obtained with the HPLC method of area %, calculation. Unless otherwise specified, all reactions were carried out on a small scale, typically in the milligram range. For some key intermediates, reactions were performed on a larger scale, up to a maximum of approximately 3 g. Final compounds were generally obtained in milligram quantities and purified for biological evaluation.

4.2.1. General procedure for the synthesis of 4-(benzyloxy)benzaldehydes 3a-q derivatives – step 1

To a stirred mixture of 4-Hydroxybenzaldehyde derivative 2a-h (1.1 eq.) in ACN (3 mL) was added K_2CO_3 (5 eq.) followed byand after 5 a mixture of aryl-bromide 1a-e (1 eq.) in ACN (3 mL). The obtained suspension was stirred under reflux, once the reaction was completeat complete reaction the mixture was cooled to room temperature and the solvent was evaporated under reduced pressure. The residue was dissolved in DCM and washed with 4M NaOH acq. solution, the aqueous layer was separated and extracted 3 times with DCM. The organic phases collected were washed with brine and dried over Na_2SO_4. The solvent was removed under reduced pressure and the intermediates obtained 3a-q are used in subsequent step 2 without further purification.

4.2.1.1. 3-methoxy-4-((2-methylbenzyl)oxy)benzaldehyde (3a). Colorless oil, 97 % yield (87 mg). ^1H NMR (400 MHz, Chloroform-d) δ 9.84 (s, 1H), 7.43–7.37 (m, 3H), 7.25–7.17 (m, 3H), 7.01 (d, J = 8.0 Hz, 1H), 5.19 (s, 2H), 3.92 (s, 3H), 2.38 (s, 3H).

4.2.1.2. 4-((2-methylbenzyl)oxy)-3-(trifluoromethyl)benzaldehyde (3b). Yellowish solid, 79 % yield (56 mg). ^1H NMR (400 MHz, DMSO-d_6) δ 9.97 (s, 1H), 8.24–8.17 (m, 2H), 7.65 (d, J = 8.6 Hz, 1H), 7.47–7.43 (m, 1H), 7.31–7.21 (m, 3H), 5.39 (s, 2H), 2.33 (s, 3H).

4.2.1.3. 4-((2-methylbenzyl)oxy)-3-nitrobenzaldehyde (3c). Yellow solid, 83 % yield (80 mg). ^1H NMR (400 MHz, DMSO-d_6) δ 9.96 (s, 1H), 8.44 (d, J = 2.1 Hz, 1H), 8.21 (dd, J = 8.8, 2.1 Hz, 1H), 7.75 (d, J = 8.8 Hz, 1H), 7.46 (d, J = 7.4 Hz, 1H), 7.26 (m, J = 7.4, 7.0, 3.3 Hz), 5.43 (s, 2H), 2.34 (s, 3H).

4.2.1.4. 3-methoxy-4-((2-(trifluoromethyl)benzyl)oxy)benzaldehyde (3d). White solid, 84 % yield (102 mg). ^1H NMR (400 MHz, DMSO-d_6) δ 9.86 (s, 1H), 7.84–7.72 (m, 3H), 7.64–7.54 (m, 2H), 7.45 (d, J = 1.9 Hz, 1H), 7.27 (d, J = 8.3 Hz, 1H), 5.34 (d, J = 1.3 Hz, 2H), 3.84 (s, 3H).

4.2.1.5. 3-(trifluoromethyl)-4-((2-(trifluoromethyl)benzyl)oxy) benzaldehyde (3e). Yellow solid, 98 % yield (110 mg). ^1H NMR (400 MHz,

DMSO-d_6) δ 9.98 (s, 1H), 8.27–8.17 (m, 2H), 7.84 (d, J = 7.8 Hz, 1H), 7.82–7.73 (m, 2H), 7.67–7.58 (m, 2H), 5.51 (s, 2H).

4.2.1.6. 3-nitro-4-((2-(trifluoromethyl)benzyl)oxy)benzaldehyde (3f). Yellow solid, 67 % yield (93 mg). ^{1}H NMR (400 MHz, DMSO-d_6) δ 9.97 (s, 1H), 8.46 (d, J = 2.1 Hz, 1H), 8.22 (dd, J = 8.7, 2.1 Hz, 1H), 7.85–7.75 (m, 3H), 7.71 (d, J = 8.8 Hz, 1H), 7.64 (dd, J = 8.5, 6.7 Hz, 1H), 5.56 (s, 2H).

4.2.1.7. 3-methoxy-4-((2-nitrobenzyl)oxy)benzaldehyde (3g). Yellow solid, 93 % yield (160 mg). ^{1}H NMR (400 MHz, DMSO-d_6) δ 9.86 (s, 1H), 8.17 (dd, J = 8.1, 1.2 Hz, 1H), 7.84–7.76 (m, 2H), 7.65 (td, J = 7.6, 6.9, 2.0 Hz, 1H), 7.54 (dd, J = 8.2, 1.9 Hz, 1H), 7.46 (d, J = 1.9 Hz, 1H), 7.26 (d, J = 8.3 Hz, 1H), 5.59 (s, 2H), 3.87 (s, 3H).

4.2.1.8. 4-((2-nitrobenzyl)oxy)-3-(trifluoromethyl)benzaldehyde (3h). White solid, 82 % yield (143 mg). ^{1}H NMR (400 MHz, DMSO-d_6) δ 9.98 (s, 1H), 8.25–8.16 (m, 3H), 7.86 (td, J = 7.5, 1.3 Hz, 1H), 7.79 (dd, J = 7.9, 1.5 Hz, 1H), 7.68 (ddd, J = 8.7, 7.4, 1.6 Hz, 1H), 7.60 (d, J = 9.2 Hz, 1H), 5.77 (s, 2H).

4.2.1.9. 4-((4-(tert-butyl)benzyl)oxy)-3-methoxybenzaldehyde (3i). White solid, 96 % yield (160 mg). ^{1}H NMR (400 MHz, DMSO-d_6) δ 9.85 (s, 1H), 7.55 (dd, J = 8.3, 1.9 Hz, 1H), 7.47–7.36 (m, 5H), 7.28 (d, J = 8.3 Hz, 1H), 5.18 (s, 2H), 3.84 (s, 3H), 1.29 (s, 9H).

4.2.1.10. 4-((4-(tert-butyl)benzyl)oxy)-3-nitrobenzaldehyde (3j). The product obtained following the general procedure of step 1 is in an orange oil, this was triturated with Et_2O and n-exane and the product was obtained as yellow flaky crystals, 52 % yield (80 mg). ^{1}H NMR (600 MHz, $CDCl_3$) δ 9.93 (s, 1H), 8.35 (d, J = 2.1 Hz, 1H), 8.04 (dd, J = 8.7, 2.1 Hz, 1H), 7.46–7.41 (d, 2H), 7.38 (d, J = 8.3 Hz, 2H), 7.27 (d, J = 14.7 Hz, 1H), 5.31 (s, 1H), 1.33 (s, 9H).

4.2.1.11. 4-([1,1′-biphenyl]-4-ylmethoxy)-3-methoxybenzaldehyde (3k). White solid, 96 % yield (87 mg). ^{1}H NMR (400 MHz, DMSO-d_6) δ 9.85 (s, 1H), 7.74–7.64 (m, 3H), 7.59–7.52 (m, 3H), 7.52–7.41 (m, 3H), 7.41–7.34 (m, 1H), 7.30 (d, J = 8.3 Hz, 1H), 5.27 (s, 2H), 3.85 (s, 3H).

4.2.1.12. 4-([1,1′-biphenyl]-4-ylmethoxy)-3-fluorobenzaldehyde (3l). White solid, 68 % yield (64 mg). ^{1}H NMR (400 MHz, DMSO-d_6) δ 9.87 (d, J = 2.0 Hz, 1H), 7.85–7.76 (m, 1H), 7.76–7.66 (m, 6H), 7.63–7.42 (m, 6H), 7.42–7.33 (m, 1H), 5.37 (s, 2H).

4.2.1.13. 4-([1,1′-biphenyl]-4-ylmethoxy)-2-methoxybenzaldehyde (3 m). White solid, 97 % yield (170 mg). ^{1}H NMR (600 MHz, DMSO-d_6) δ 10.19 (s, 1H), 7.73–7.66 (m, 5H), 7.57 (d, J = 8.2 Hz, 2H), 7.48 (t, J = 7.7 Hz, 2H), 7.38 (t, J = 7.4 Hz, 1H), 6.83 (d, J = 2.2 Hz, 1H), 6.76 (dd, J = 8.7, 1.5 Hz, 1H), 5.29 (s, 2H), 3.91 (s, 3H).

4.2.1.14. 4-([1,1′-biphenyl]-4-ylmethoxy)-3,5-dimethoxybenzaldehyde (3n). White solid, 98 % yield (160 mg). ^{1}H NMR (400 MHz, DMSO-d_6) δ 9.89 (s, 1H), 7.71–7.63 (m, 4H), 7.54 (d, 2H), 7.47 (t, J = 7.7 Hz, 2H), 7.38 (t, 1H), 7.28 (s, 2H), 5.09 (s, 2H), 3.88 (s, 6H).

4.2.1.15. 3-methoxy-4-((2-methylbenzyl)oxy)-5-nitrobenzaldehyde (3o). Off-white solid, 40 % yield (147 mg). ^{1}H NMR (400 MHz, DMSO) δ 9.97 (s, 1H), 8.01 (d, J = 1.8 Hz, 1H), 7.85 (d, J = 1.8 Hz, 1H), 7.34–7.14 (m, 4H), 5.26 (s, 2H), 4.04 (s, 3H), 2.35 (s, 3H).

4.2.1.16. 4-((4-(tert-butyl)benzyl)oxy)-3-methoxy-5-nitrobenzaldehyde ***(3p).*** Yellow amorphous solid, 30 % yield. ^{1}H NMR (400 MHz, DMSO) δ 9.97 (s, 1H), 8.02 (d, J = 1.8 Hz, 1H), 7.84 (d, J = 1.8 Hz, 1H), 7.48–7.38 (m, 2H), 7.36–7.31 (m, 2H), 5.21 (s, 2H), 4.03 (s, 3H), 1.28 (s, 9H).

4.2.1.17. 3-fluoro-4-((2-methylbenzyl)oxy)-5-nitrobenzaldehyde (3q). Off-white solid, 20 % yield (56 mg). ^{1}H NMR (400 MHz, DMSO) δ 9.96 (d, J = 1.9 Hz, 1H), 8.36–8.31 (m, 1H), 8.19 (dd, J = 11.4, 2.0 Hz, 1H), 7.39–7.17 (m, 5H), 5.43 (d, J = 1.7 Hz, 2H), 2.36 (s, 3H).

4.2.1.18. 4-([1,1′-biphenyl]-4-ylmethoxy)-3-nitrobenzaldehyde (3r). White solid, 96 % yield (110 mg). ^{1}H NMR (400 MHz, DMSO) δ 9.96 (s, 1H), 8.46 (d, J = 2.0 Hz, 1H), 8.20 (dd, J = 8.7, 2.1 Hz, 1H), 7.78–7.65 (m, 6H), 7.61–7.52 (m, 2H), 7.51–7.43 (m, 2H), 7.42–7.33 (m, 1H), 5.50 (s, 2H).^{13}C NMR (101 MHz, DMSO) δ 190.92, 155.61, 140.65, 140.23, 140.11, 135.37, 134.97, 129.44, 128.69, 128.10, 127.39, 127.19, 126.97, 116.52, 71.35.

4.2.2. General procedure for multicomponent reaction to obtain 2,4,5,7-tetrahydro-6H-pyrazolo[3,4-b]pyridin-6-one (6a-q) derivatives – step 2

To a suspension of 3a-q obtained following step 1 procedure (1 eq.) in 3 mL of MeOH, 5-methyl-1H-pyrazol-3-amine 4 (1 eq.) in 3 mL of MeOH and Meldrum's Acid 5 (1 eq.) in 3 mL of MeOH were added. The mixture was stirred at reflux for 18hrs. At complete reaction, the mixture has been cooled to room temperature and the precipitate formed was filtrated via vacuum and washed with cold MeOH and let air dried for 2hrs. The desired product has been purified by flash chromatography with Biotage Isolera One automated chromatography system (DCM: MeOH 95:5). All the compounds have been tested in vitro as racemates.

4.2.2.1. 4-(3-methoxy-4-((2-methylbenzyl)oxy)phenyl)-3-methyl-2,4,5,7-tetrahydro-6H-pyrazolo[3,4-b]pyridin-6-one (6a). White solid, 50 % yield (40 mg). ^{1}H NMR (400 MHz, DMSO-d_6) δ 11.76 (s, 1H), 10.23 (s, 1H), 7.38 (d, J = 7.3 Hz, 1H), 7.27–7.18 (m, 3H), 6.99 (d, J = 8.2 Hz, 1H), 6.85 (s, 1H), 6.63 (d, J = 8.6 Hz, 1H), 5.01 (s, 2H), 4.08 (t, J = 6.7 Hz, 1H), 3.72 (s, 3H), 2.73 (dd, J = 15.7, 6.7 Hz, 1H), 2.60 (dd, J = 15.8, 6.6 Hz, 1H), 2.31 (s, 3H), 1.83 (s, 3H). ^{13}C NMR (101 MHz, DMSO) δ 169.70, 149.23, 148.73, 146.57, 136.69, 136.50, 135.13, 134.55, 130.05, 128.67, 128.03, 125.72, 118.69, 113.64, 111.22, 102.16, 68.67, 55.52, 40.78, 33.73, 18.40, 9.49. HRMS (ESI) for $C_{22}H_{24}N_3O_3$ $[M+H]^+$: calc. 378.1818 found: 378.1800. HPLC, t_R: 14.916, purity, 97.9 %

4.2.2.2. 3-methyl-4-(4-((2-methylbenzyl)oxy)-3-(trifluoromethyl)phenyl)-2,4,5,7-tetrahydro-6H-pyrazolo[3,4-b]pyridin-6-one (6b). Yellow solid, 40 % yield (18 mg). ^{1}H NMR (400 MHz, DMSO-d_6) δ 11.85 (s, 1H, H-22), 10.32 (s, 1H, H-18), 7.43 (dd, J = 4.9, 2.6 Hz, 3H, H-1, H-2, H-3), 7.37 (d, J = 9.3 Hz, 1H, H-13), 7.27–7.21 (m, 3H, H-10, H-11, H-6), 5.20 (s, 2H, 2H-7), 4.23 (t, J = 6.4 Hz, 1H, H-15), 2.73 (dd, J = 15.8, 6.8 Hz, 1H, H-16'), 2.60 (dd, J = 15.9, 6.6 Hz, 1H, H-16) 2.32 (s, 3H, 3H-25), 1.85 (s, 3H, 3H-27). ^{13}C NMR (101 MHz, DMSO) δ 169.36, 154.77, 148.77, 136.54, 135.85, 135.05, 134.60, 134.28, 132.55, 130.14, 128.16, 128.09, 125.81, 125.20, 117.10, 114.18, 101.64, 68.56, 40.59, 32.83, 18.23, 9.42. HRMS (ESI) for $C_{22}H_{21}F_3N_3O_2^+$ $[M+H]^+$: calcd. 414,1435, found 414,1435. HPLC, t_R: 12.693, purity, 95.1 %.

4.2.2.3. 3-methyl-4-(4-((2-methylbenzyl)oxy)-3-nitrophenyl)-2,4,5,7-tetrahydro-6H-pyrazolo[3,4-b]pyridin-6-one (6c). White solid, 44 % yield (12 mg). ^{1}H NMR (400 MHz, DMSO-d_6) δ 11.88 (s, 1H, H-22), 10.33 (s, 1H, H-18), 7.66 (s, 1H, H-13), 7.48–7.46 (m, 2H, H-10, H-11), 7.43 (d, J = 7.5 Hz, 1H, H-6), 7.27–7.20 (m, 3H, H-1, H-2, H-3), 5.25 (s, 2H, 2H-7), 4.24 (t, J = 6.4 Hz, 1H, H-15), 2.80 (dd, J = 15.9, 6.9 Hz, 1H, H-16'), 2.59 (dd, J = 15.9, 6.1 Hz, 1H, H-16), 2.32 (s, 3H, 3H-28), 1.86 (s, 3H, 3H-25). ^{13}C NMR (101 MHz, DMSO) δ 169.20, 149.68, 148.77, 139.38, 136.76, 136.37, 134.75, 133.88, 132.87, 130.20, 128.45, 128.37, 125.81, 123.25, 115.80, 101.21, 69.35, 40.38, 32.66, 18.37, 9.47. HRMS (ESI) for $C_{21}H_{19}N_4O_4^-$ $[M-H]^-$: calc. 391,1412, found: 391,1412. HPLC t_R: 11.929, purity, 99.0 %.

4.2.2.4. 4-(3-methoxy-4-((2-(trifluoromethyl)benzyl)oxy)phenyl)-3-methyl-2,4,5,7-tetrahydro-6H-pyrazolo[3,4-b]pyridin-6-one (6d). White

solid, 70 % yield (21 mg). ^{1}H NMR (400 MHz, DMSO-d_6) δ 11.78 (s, 1H, H-22), 10.25 (s, 1H, H-18), 7.81–7.70 (m, 3H, H-2, H-3, H-6), 7.58 (t, J = 7.6 Hz, 1H, H-1), 6.93 (d, J = 8.3 Hz, 1H, H-10), 6.88 (s, 1H, H-13), 6.63 (d, J = 8.3, 1H, H-11), 5.18 (s, 2H, 2H-7), 4.09 (t, J = 6.7 Hz, 1H, H-15), 3.74 (s, 3H, 3H-27), 2.73 (dd, J = 15.8, 6.8 Hz, 1H, H-16'), 2.60 (dd, J = 15.9, 6.6 Hz, 1H, H-16), 1.83 (s, 3H, 3H-25)) ^{13}C NMR (101 MHz, DMSO) δ 169.67, 149.31, 148.73, 146.12, 137.16, 135.26, 134.57, 132.81, 130.20, 128.57, 126.7-126.47-125.97-125.65 (q), 125.91, 122.93,118.76, 113.94, 111.42, 102.09, 66.77, 55.57, 40.73, 33.73, 9.47. HRMS (ESI) for $C_{21}H_{19}N_4O_4^-$ [M − H]$^-$: calcd. 432,1530, found: 432,1530. HPLC t_R: 11.737, purity, 99.5 %.

4.2.2.5. 3-methyl-4-(3-(trifluoromethyl)-4-((2-(trifluoromethyl)benzyl) oxy)phenyl)-2,4,5,7-tetrahydro-6H-pyrazolo[3,4-b]pyridin-6-one (6e). Yellow solid, 80 % yield (17 mg). ^{1}H NMR (400 MHz, DMSO-d_6) δ 11.86 (s, 1H, H-22), 10.33 (s, 1H, H-18), 7.80 (d, J = 7.7 Hz, 1H, H-3), 7.75 (s, 2H, H-1, H-6), 7.60 (s, 1H, H-13), 7.43 (d, J = 9.6 Hz, 2H, H-2, H-11), 7.30 (d, J = 8.4 Hz, 1H, H-10), 5.33 (s, 2H, 2H-7), 4.23 (t, J = 6.2 Hz, 1H, H-15), 2.80 (dd, J = 15.9, 6.9 Hz, 1H, H-16'), 2.56 (dd, J = 15.9, 5.9 Hz, 1H, H-16), 1.84 (s, 3H, H-25). ^{13}C NMR (101 MHz, DMSO) δ 9.42, 32.84, 39.52, 40.56, 66.78, 101.56, 114.14, 117.32, 125.24, 126.19, 128.88, 129.93, 132.69, 132.93, 134.16, 136.37, 148.74, 154.32, 169.32. HRMS (ESI) $C_{22}H_{16}F_6N_3O_2^-$ [M − H]$^-$: calc. 468,1152, found: 468,1150 t_R: 18.509, purity, 99.7 %.

4.2.2.6. 3-methyl-4-(3-nitro-4-((2-(trifluoromethyl)benzyl)oxy)phenyl)-2,4,5,7-tetrahydro-6H-pyrazolo[3,4-b]pyridin-6-one (6f). White solid, 80 % yield (14 mg). ^{1}H NMR (400 MHz, DMSO-d_6) δ 11.88 (s, 1H, H-22), 10.34 (s, 1H, H-18), 7.78 (dd, J = 15.7, 7.6 Hz, 3H, H-1, H-2, H-3), 7.69 (d, J = 2.1 Hz, 1H, H-6), 7.61 (t, J = 7.6 Hz, 1H, H-13), 7.49–7.40 (m, 2H, H-10, H-11), 5.39 (s, 2H, 2H-7), 4.25 (t, J = 6.4 Hz, 1H, H-15), 2.81 (dd, J = 15.9, 6.9 Hz, 1H, H-16'), 2.59 (dd, J = 15.9, 6.1 Hz, 1H, H-16), 1.86 (s, 3H, 3H-25). ^{13}C NMR (101 MHz, DMSO) δ 169.39, 149.53, 148.98, 139.60, 137.07, 134.98, 133.99, 133.26, 133.16, 130.41, 129.22, 127.42-127.11-126.81-126.52 (q), 126.52-126.4-126.41-126.35 (q), 125.76–123.04 (d) 123.62, 115.94, 101.36, 67.74, 40.55, 32.87, 9.68. HRMS (ESI) for $C_{21}H_{16}F_3N_4O_4^-$ [M − H]$^-$: Calc: 445,1129, found: 445,1129. HPLC, t_R: 13.961, purity, 97.9 %.

4.2.2.7. 4-(3-methoxy-4-((2-nitrobenzyl)oxy)phenyl)-3-methyl-2,4,5,7-tetrahydro-6H-pyrazolo[3,4-b]pyridin-6-one (6g). Yellow solid, 58 % yield (19 mg). ^{1}H NMR (400 MHz, DMSO-d_6) δ 11.77 (s, 1H, H-22), 10.24 (s, 1H, H-18), 8.12 (d, J = 8.0 Hz, 1H, H-6), 7.82–7.76 (m, 1H, H-2), 7.61 (ddd, J = 8.7, 5.8, 3.2 Hz, 2H, H-1, H-3), 6.94–6.86 (m, 2H, H-10, H-13), 6.62 (dd, J = 8.3, 2.0 Hz, 1H, H-11), 5.39 (s, 2H, 2H-7), 4.08 (t, J = 6.7 Hz, 1H, H-15), 3.74 (s, 3H, 3H-27), 2.72 (dd, J = 15.8, 6.8 Hz, 1H, H-16'), 2.60 (dd, J = 15.8, 6.7 Hz, 1H, H-16), 1.82 (s, 3H, 3H-25). ^{13}C NMR (101 MHz, DMSO) δ 169.68, 149.29, 148.72, 147.34, 145.95, 137.21, 134.57, 134.04, 132.87, 129.20, 129.03, 124.79, 118.79, 114.16, 111.45, 102.10, 67.22, 55.63, 40.71, 33.76, 9.48. HRMS (ESI) for $C_{21}H_{19}N_4O_5^-$ [M − H]$^-$: Calc: 407,1361, found: 407,1358. HPLC, t_R: 11.049, purity, 98.0 %.

4.2.2.8. 3-methyl-4-(4-((2-nitrobenzyl)oxy)-3-(trifluoromethyl)phenyl)-2,4,5,7-tetrahydro-6H-pyrazolo[3,4-b]pyridin-6-one (6h). Yellow solid, 62 % yield (22 mg). ^{1}H NMR (400 MHz, DMSO-d_6) δ 11.85 (s, 1H, H-22), 10.33 (s, 1H, H-18), 8.16 (s, 1H, H-6), 7.87–7.75 (m, 2H, H-2, H-13), 7.69–7.60 (m, 1H, H-3), 7.48–7.38 (m, 2H, H-1, H-11), 7.31 (d, J = 8.5 Hz, 1H, H-10), 5.59 (s, 2H, 2H-7), 4.23 (t, J = 6.5 Hz, 1H, H-15), 2.79 (dd, J = 15.6, 6.8 Hz, 1H, H-16'), 2.57 (dd, J = 16.0, 6.0 Hz, 1H, H-16), 1.84 (s, 3H, 3H-25). ^{13}C NMR (101 MHz, DMSO) δ 169.34, 154.17, 148.77, 147.15, 136.41, 134.62, 134.27, 132.73, 131.97, 129.29, 128.75, 125.30, 125.07, 122.31, 117.16, 114.22, 101.58, 67.10, 40.53, 32.85, 9.42. HRMS (ESI) for $C_{21}H_{16}F_3N_4O_4^-$ [M − H]$^-$: Calc: 445,1129, found: 445,1133. HPLC, t_R: 10.366, purity, 96.7 %.

4.2.2.9. 4-(4-((4-(tert-butyl)benzyl)oxy)-3-methoxyphenyl)-3-methyl-2,4,5,7-tetrahydro-6H-pyrazolo[3,4-b]pyridin-6-one (6i). White solid, 70 % yield (24 mg). ^{1}H NMR (400 MHz, DMSO-d_6) δ 11.77 (s, 1H), 10.25 (s, 1H), 7.44–7.30 (m, 4H), 6.94 (d, J = 8.3 Hz, 1H), 6.84 (d, J = 2.1 Hz, 1H), 6.61 (dd, J = 8.3, 2.1 Hz, 1H), 4.98 (s, 2H), 4.07 (t, J = 6.7 Hz, 1H), 3.71 (s, 3H), 2.71 (dd, J = 15.8, 6.8 Hz, 1H), 2.59 (dd, J = 15.8, 6.8 Hz, 1H), 1.82 (s, 3H), 1.28 (s, 9H). ^{13}C NMR (101 MHz, DMSO) δ 169.70, 150.27, 149.11, 148.72, 146.59, 136.34, 134.54, 134.19, 127.73, 125.11, 118.69, 113.44, 111.23, 102.17, 69.74, 55.50, 40.78, 34.28, 33.74, 31.12, 9.48. HRMS (ESI) for $C_{25}H_{30}N_3O_3$ [M+H]$^+$: calc = 420,2282, found: 420,2275. HPLC, t_R: 17.710, purity, 97.4 %.

4.2.2.10. 4-(4-((4-(tert-butyl)benzyl)oxy)-3-nitrophenyl)-3-methyl-2,4,5,7-tetrahydro-6H-pyrazolo[3,4-b]pyridin-6-one (6j). Off white solid, 50 % yield (30 mg). ^{1}H NMR (400 MHz, DMSO) δ 11.88 (s, 1H), 10.33 (s, 1H), 7.66 (d, J = 1.9 Hz, 1H), 7.46–7.32 (m, 6H), 5.23 (s, 2H), 4.23 (t, J = 6.5 Hz, 1H), 2.79 (dd, J = 15.9, 6.9 Hz, 1H), 2.58 (dd, J = 15.9, 6.2 Hz, 1H), 1.84 (s, 3H), 1.27 (s, 9H); ^{13}C NMR (101 MHz, DMSO) δ 169.21, 150.61, 149.72, 148.76, 139.47, 136.34, 134.75, 132.97, 132.86, 127.42, 125.28, 123.24, 115.86, 101.22, 70.38, 40.37, 34.32, 32.67, 31.09, 9.46. HRMS (ESI) for $C_{24}H_{25}N_4O_4$ [M+H]$^-$: calc: 433,1881, found: 433,1870. HPLC t_R: 18.161, purity, 95.1 %.

4.2.2.11. 4-(4-([1,1′-biphenyl]-4-ylmethoxy)-3-methoxyphenyl)-3-methyl-2,4,5,7-tetrahydro-6H-pyrazolo[3,4-b]pyridin-6-one (6k). White solid, 40 % yield (11 mg). ^{1}H NMR (400 MHz, DMSO) δ 11.77 (s, 1H), 10.25 (s, 1H), 7.72–7.63 (m, 4H), 7.55–7.42 (m, 4H), 7.41–7.32 (m, 1H), 6.97 (d, J = 8.3 Hz, 1H), 6.86 (d, J = 2.1 Hz, 1H), 6.63 (dd, J = 8.3, 2.1 Hz, 1H), 5.08 (s, 2H), 4.08 (t, J = 6.7 Hz, 1H), 3.74 (s, 3H), 2.65 (ddd, 2H), 1.82 (s, 3H); ^{13}C NMR (101 MHz, DMSO) δ 169.70, 149.18, 148.73, 146.48, 139.83, 139.66, 136.50, 136.44, 134.55, 128.94, 128.36, 127.48, 126.70, 126.66, 118.71, 113.64, 111.28, 102.16, 69.64, 55.55, 40.78, 33.74, 9.48. HRMS (ESI) for $C_{27}H_{24}N_3O_3$ [M − H]$^-$: Calc = 438,1823, found = 438,1826. HPLC, t_R: 17.073, purity, 96.2 %.

4.2.2.12. 4-(4-([1,1′-biphenyl]-4-ylmethoxy)-3-fluorophenyl)-3-methyl-2,4,5,7-tetrahydro-6H-pyrazolo[3,4-b]pyridin-6-one (6l). White solid, 38 % yield (21 mg). ^{1}H NMR (600 MHz, DMSO) δ 11.82 (s, 1H), 10.28 (s, 1H), 7.71–7.65 (m, 4H), 7.53 (d, J = 8.1 Hz, 2H), 7.47 (t, J = 7.8 Hz, 2H), 7.37 (t, 1H), 7.21 (t, J = 8.7 Hz, 1H), 7.02 (dd, J = 12.5, 2.1 Hz, 1H), 6.92 (d, 1H), 5.19 (s, 2H), 4.11 (t, J = 6.5 Hz, 1H), 2.75 (dd, J = 15.8, 6.8 Hz, 1H), 2.56 (dd, J = 15.8, 6.2 Hz, 1H), 1.83 (s, 3H). ^{13}C NMR (151 MHz, DMSO) δ 169.43, 152.49, 150.88, 148.69, 144.72, 144.65, 139.89, 139.75, 137.11, 137.08, 135.78, 134.63, 128.95, 128.42, 127.53, 126.79, 126.68, 122.96, 122.94, 115.54, 114.68, 114.56, 101.76, 69.95, 40.53, 33.02, 9.40. HRMS (ESI) for $C_{26}H_{23}FN_3O_2$ [M+H]$^+$: calc = 428,1769, found = 428,1769. HPLC t_R: 17.203, purity, 95.7 %.

4.2.2.13. 4-(4-([1,1′-biphenyl]-4-ylmethoxy)-2-methoxyphenyl)-3-methyl-2,4,5,7-tetrahydro-6H-pyrazolo[3,4-b]pyridin-6-one (6 m). Yellowish solid, 50 % yield (17 mg). ^{1}H NMR (600 MHz, DMSO) δ 11.79 (s, 1H), 10.20 (s, 1H), 7.69 (dd, J = 7.8, 5.5 Hz, 4H), 7.54 (d, J = 7.9 Hz, 2H), 7.48 (t, J = 7.6 Hz, 2H), 7.38 (t, J = 7.4 Hz, 1H), 6.71–6.66 (m, 2H), 6.53 (dd, J = 8.4, 2.4 Hz, 1H), 5.12 (s, 2H), 4.31 (dd, J = 7.3, 4.5 Hz, 1H), 3.82 (s, 3H), 2.73 (dd, J = 15.9, 7.4 Hz, 1H), 2.47 (dd, J = 15.9, 4.5 Hz, 1H), 1.87 (s, 3H). ^{13}C NMR (151 MHz, DMSO) δ 169.84, 158.39, 157.21, 149.29, 139.81, 139.69, 136.31, 134.34, 128.94, 128.36, 127.60, 127.49, 126.73, 126.67, 123.51, 105.34, 101.29, 99.36, 69.00, 55.41, 40.06, 27.16, 9.31. HRMS (ESI) for $C_{27}H_{26}N_3O_3$ [M+H]$^+$: Calc = 440,1969, found = 440,1969. HPLC t_R: 18.107, purity, 97.0 %.

4.2.2.14. 4-(4-([1,1′-biphenyl]-4-ylmethoxy)-3,5-dimethoxyphenyl)-3-methyl-2,4,5,7-tetrahydro-6H-pyrazolo[3,4-b]pyridin-6-one (6n). Yellow solid, 70 % yield (18 mg). ^{1}H NMR (600 MHz, DMSO) δ 11.78 (s, 1H),

10.28 (s, 0H), 7.66 (dd, 2H), 7.52 (d, $J = 8.1$ Hz, 1H), 7.47 (t, $J = 7.8$ Hz, 1H), 7.37 (t, 1H), 6.54 (s, 1H), 4.92 (s, 1H), 4.09 (t, $J = 7.2$ Hz, 1H), 3.73 (s, 3H), 2.74–2.63 (m, 1H), 1.80 (s, 1H). ^{13}C NMR (151 MHz, DMSO) δ 169.78, 153.09, 148.73, 139.94, 139.50, 139.32, 137.15, 134.98, 134.69, 128.96, 128.52, 127.44, 126.64, 126.37, 104.46, 101.97, 73.65, 55.95, 40.62, 34.67, 9.53. HRMS (ESI) for $C_{28}H_{28}N_3O_4$ $[M+H]^+$: calc = 470,2074, found = 470,2074. HPLC, t_R: 17.203, purity, 95.7 %.

4.2.2.15. 4-(3-methoxy-4-((2-methylbenzyl)oxy)-5-nitrophenyl)-3-methyl-2,4,5,7-tetrahydro-6H-pyrazolo[3,4-b]pyridin-6-one (6o). Off-white solid, 30 % yield (25 mg). ^{1}H NMR (400 MHz, DMSO) δ 11.89 (s, 1H), 10.36 (s, 1H), 7.36–7.14 (m, 6H), 7.11 (d, $J = 2.0$ Hz, 1H), 5.10 (s, 2H), 4.26 (t, $J = 6.9$ Hz, 1H), 3.92 (s, 3H), 2.78 (dd, $J = 15.9$, 6.8 Hz, 1H), 2.70 (dd, $J = 15.9$, 7.1 Hz, 1H), 2.35 (s, 3H), 1.85 (s, 3H). ^{13}C NMR (101 MHz, DMSO) δ 169.73, 154.21, 149.26, 145.18, 140.92, 139.20, 137.34, 135.32, 134.90, 130.52, 130.03, 128.97, 126.22, 116.41, 113.91, 101.43, 73.74, 57.11, 40.68, 34.24, 18.71, 10.04. HRMS (ESI) for $C_{22}H_{23}N_4O_5^+$ $[M+H]^+$: calc. 422,1590, found: 423.1646. HPLC, t_R: 15.918, purity, 95.2 %.

4.2.2.16. 4-(4-((4-(tert-butyl)benzyl)oxy)-3-methoxy-5-nitrophenyl)-3-methyl-2,4,5,7-tetrahydro-6H-pyrazolo[3,4-b]pyridin-6-one (6p). Off-white solid, 35 % yield (22 mg). ^{1}H NMR (400 MHz, DMSO) δ 11.88 (s, 1H), 10.34 (s, 1H), 7.43–7.35 (m, 2H), 7.34–7.27 (m, 3H), 7.10 (d, $J = 2.0$ Hz, 1H), 5.05 (s, 2H), 4.24 (t, $J = 6.9$ Hz, 1H), 3.91 (s, 3H), 2.73 (ddd, $J = 15.9$, 15.8, 7.0 Hz, 2H), 1.82 (s, 3H), 1.28 (s, 9H). ^{13}C NMR (101 MHz, DMSO) δ 169.24, 153.67, 150.77, 148.77, 144.62, 140.33, 138.76, 134.81, 133.39, 128.23, 125.05, 115.92, 113.41, 100.96, 75.03, 56.63, 40.19, 34.31, 33.77, 31.09, 9.54. HRMS (ESI) for $C_{25}H_{29}N_4O_5^+$ $[M+H]^+$: Calc. 465.2138, found: 465.2117. HPLC t_R: 18.883, purity, 98.8 %.

4.2.2.17. 4-(3-fluoro-4-((2-methylbenzyl)oxy)-5-nitrophenyl)-3-methyl-2,4,5,7-tetrahydro-6H-pyrazolo[3,4-b]pyridin-6-one (6q). Off-white solid, 27 % yield (16 mg). ^{1}H NMR (400 MHz, DMSO) δ 11.93 (s, 1H), 10.38 (s, 1H), 7.54 (d, $J = 2.7$ Hz, 2H), 7.34–7.14 (m, 4H), 5.21 (s, 2H), 4.29 (t, $J = 6.7$ Hz, 1H), 2.80 (dd, $J = 15.9$, 6.9 Hz, 1H), 2.65 (dd, $J = 16.0$, 6.6 Hz, 1H), 2.34 (s, 3H), 1.85 (s, 3H). ^{13}C NMR (101 MHz, DMSO) δ 169.45, 154.57, 149.21, 144.90, 144.86, 141.24, 141.18, 138.68, 138.52, 137.55, 135.44, 134.23, 130.67, 130.07, 129.36, 126.32, 120.69, 120.48, 119.22, 101.01, 75.38, 75.33, 33.59, 18.68, 9.98. HRMS (ESI) for $C_{21}H_{20}FN_4O_4^+$ $[M+H]^+$: calc. = 411.1469, found = 411.1449. HPLC, t_R: 16.064, purity, 95.1 %.

4.2.2.18. 4-(4-([1,1′-biphenyl]-4-ylmethoxy)-3-nitrophenyl)-3-methyl-2,4,5,7-tetrahydro-6H-pyrazolo[3,4-b]pyridin-6-one (6r). White solid, yield 30 % (19 mg). ^{1}H NMR (400 MHz, DMSO) δ 11.90 (s, 1H), 10.36 (s, 1H), 7.75–7.65 (m, 5H), 7.60–7.52 (m, 2H), 7.52–7.42 (m, 4H), 7.42–7.34 (m, 1H), 5.34 (s, 2H), 4.25 (t, $J = 6.4$ Hz, 1H), 2.81 (dd, $J = 15.9$, 6.9 Hz, 1H), 2.60 (dd, $J = 15.9$, 6.2 Hz, 1H), 1.87 (s, 3H). ^{13}C NMR (101 MHz, DMSO) δ 169.23, 149.70, 148.79, 139.96, 139.71, 139.48, 136.46, 135.18, 134.79, 132.94, 128.95, 128.09, 127.56, 126.84, 126.70, 123.33, 115.93, 101.23, 70.26, 40.38, 32.70, 9.48. HRMS (ESI). HPLC, t_R: 14.284, purity, 96.6 %.

4.2.2.19. 3-((4-formyl-2-methoxyphenoxy)methyl)benzonitrile (8). To a solution of 4-hydroxy-3-(trifluoromethyl)-benzaldehyde (1,4 mmol, 1.1 eq.) in acetonitrile (3 mL) was added K_2CO_3 (550 mg, 4 eq.) and a mixture of 2-nitro-benzylbromide (1,3 mmol, 1 eq.) in acetonitrile (3 mL). The suspension was stirred at reflux for 5 hrs after which the mixture was cooled at room temperature the suspension was filtered to remove K_2CO_3 and the filtrate was concentrated under reduced pressure. The residue obtained was dissolved in DCM and washed with NaOH 4 M acq. The aqueous phase was extracted 3 times with DCM and all the organic phases collected where washed with brine, dried over Na_2SO_4 and the solvent removed under reduced pressure to obtain the desired product as a yellowish solid, 57 % yield (70 mg). The product is used in subsequent reactions without further purification. ^{1}H NMR (400 MHz, $CDCl_3$) δ 9.87 (s, 1H), 7.80–7.74 (m, 1H), 7.71–7.66 (m, 1H), 7.66–7.61 (m, 1H), 7.52 (t, $J = 0.6$ Hz, 1H), 7.46 (d, $J = 1.9$ Hz, 1H), 7.42 (dd, $J = 8.1$, 1.9 Hz, 1H), 6.97 (d, $J = 8.2$ Hz, 1H), 5.24 (s, 2H), 3.97 (s, 3Hz). ^{13}C NMR (101 MHz, $CDCl_3$) δ 190.97, 153.01, 150.29, 137.86, 132.04, 131.50, 131.02, 130.77, 129.73, 126.47, 118.66, 113.14, 112.59, 109.77, 69.74, 56.22.

4.2.2.20. 3-((2-methoxy-4-(3-methyl-6-oxo-4,5,6,7-tetrahydro-1H-pyrazolo[3,4-b]pyridin-4-yl)phenoxy)methyl) benzonitrile (9). To a solution of 3-((4-formyl-2-methoxyphenoxy)methyl)benzonitrile (**8**) (1 eq.) in 3 mL of MeOH was added in this order 5-methyl-1H-pyrazol-3-amine (1 eq.) in 3 mL of MeOH and Meldrum Acid (1 eq.) in 3 mL of MeOH. The mixture was stirred at reflux for 6hrs. At complete reaction, the mixture has been cooled to room temperature and the solvent removed under reduced pressure. The residue has been dissolved in DCM and the organic phase washed with NaOH acq. 4 M. The aqueous phase was extracted 3 times with DCM and the organic phases collected were washed with brine, dried over Na_2SO_4 and the solvent removed under reduced pressure. The residue obtained has been purified by flash chromatography (DCM:MeOH 95:5). White solid, 30 % yield (50 mg). ^{1}H NMR (400 MHz, DMSO) δ 11.77 (s, 1H), 10.25 (s, 1H), 7.87 (s, 1H), 7.84–7.74 (m, 2H), 7.61 (t, $J = 7.8$ Hz, 1H), 6.95 (d, $J = 8.2$ Hz, 1H), 6.87 (d, $J = 2.1$ Hz, 1H), 6.62 (dd, $J = 8.3$, 2.1 Hz, 1H), 5.10 (s, 2H), 4.08 (t, $J = 6.8$ Hz, 1H), 3.74 (s, 3H), 2.71 (dd, $J = 15.8$, 6.8 Hz, 1H), 2.60 (dd, $J = 15.8$, 6.9 Hz, 1H), 1.81 (s, 3H).^{13}C NMR (101 MHz, DMSO) δ 169.73, 149.31, 148.77, 146.13, 139.07, 137.02, 134.60, 132.54, 131.65, 131.11, 129.76, 118.78, 118.74, 114.12, 111.40, 102.17, 69.04, 55.61, 40.79, 33.83, 9.51. HRMS (ESI) for $C_{22}H_{19}N_4O_3^-$ $[M-H]^-$: Calc: 387,1463, found: 387,1468. HPLC, t_R: 18.509, purity, 98.9 %.

4.2.2.21. 3-((2-methoxy-4-(3-methyl-6-oxo-4,5,6,7-tetrahydro-1H-pyrazolo[3,4-b]pyridin-4-yl)phenoxy) methyl) benzoic acid (10). To a stirred solution of NaOH (4 eq.; 20 mg) in H_2O:EtOH 1:1 (8 mL) was added 3-((2-methoxy-4-(3-methyl-6-oxo-4,5,6,7-tetrahydro-1H-pyrazolo[3,4-b] pyridin-4-yl)phenoxy)methyl)benzonitrile (**9**) (1 eq; 50 mg). The solution was stirred at reflux for 5 hrs. At complete reaction, the mixture was cooled to room temperature and EtOH was removed under reduced pressure. To the remaining aqueous mixture was added HCl 4 N acq. at 0 °C until pH 2. The mixture was extracted four times with EtOAc, the organic phases collected were washed with brine, dried over Na_aSO_4 and the solvent removed under reduced pressure. The residue was purified via recrystallization in EtOH to obtain the desired product as a white solid, 87 % yield (43 mg). ^{1}H NMR (400 MHz, DMSO) δ 11.88 (s, 1H), 10.35 (s, 1H), 7.42–7.35 (m, 2H), 7.34–7.27 (m, 3H), 7.10 (d, $J = 2.0$ Hz, 1H), 5.05 (s, 2H), 4.24 (t, $J = 6.9$ Hz, 1H), 3.91 (s, 3H), 2.77 (dd, $J = 15.9$, 6.7 Hz, 1H), 2.69 (dd, $J = 15.9$, 7.2 Hz, 1H), 1.82 (s, 3H). ^{13}C NMR (101 MHz, DMSO) δ 169.26, 153.68, 150.78, 148.77, 144.63, 140.34, 138.78, 134.84, 133.40, 128.24, 125.06, 115.93, 113.41, 100.96, 75.04, 56.64, 40.21, 34.31, 33.78, 31.09, 9.56. HRMS (ESI) for $C_{22}H_{20}N_3O_5^-$ $[M-H]^-$: Calc: 406,1408, found: 406,1428. HPLC, t_R: 15.885, purity, 97.9 %.

HPLC-UV/Vis Purity and ^{1}H/^{13}C NMR characterization of the compounds are reported in Supplementary Information 4 and Supplementary Information 5, respectively.

4.2.2.22. 2-methoxy-N-(2-phenylpropan-2-yl)benzenesulfonamide (13). In a two-necked round-bottom flask, cumylamine **12** (4.17 mL, 29.04 mmol, 2.4 eq.) was dissolved in CH_2Cl_2 (40 mL) and TEA (2.00 mL, 5.80 mmol, 1.2 eq.) was added and cooled to 0 °C. To the stirred suspension, 2-methoxybenzene sulfonyl chloride **11** (2.50 g, 12.10 mmol, 1 eq.) dissolved in CH_2Cl_2 (12 mL) was slowly added (over 2 min). The ice-bath was removed, and the mixture was left to stir for

18 h at RT. After complete consumption of the starting material (TLC monitoring), the solution was acidified with HCl 1 N, the layers were separated and the organic phase dried (Na_2SO_4) and concentrated in *vacuo*. The crude product was purified by FC (Petroleum spirit: Ethyl acetate) to give (3.23 g, yeld 87 %). R_f 0.71 (5:5 PE:EtOAc).^{1}H NMR (400 MHz, DMSO) δ 1.43 (s, 6H), 3.87 (s, 3H), 6.93 (td, $J = 7.5$, 1.0 Hz, 1H), 7.02–7.12 (m, 2H), 7.12–7.24 (m, 2H), 7.29–7.37 (m, 2H), 7.44–7.53 (m, 2H), 7.54 (s, 1H). ^{13}C NMR (101 MHz, DMSO) δ 29.46, 55.66, 57.25, 112.43, 119.76, 125.22, 126.19, 127.46, 128.59, 130.41, 133.82, 146.46, 155.97. HRMS (ESI) for $C_{16}H_{18}NO_3S^-$ [M − H]$^-$ calc. 304.1013, found:304.1013.

4.2.2.23. N,N-diethyl-3-methoxy-2-(N-(2-phenylpropan-2-yl)sulfamoyl) benzamide (14). In an oven-dried three-necked round-bottom flask under N_2, TMEDA (0.50 mL, 3.38 mmol, 2.2 eq.) was dissolved in anhydrous THF (5 mL) and the solution cooled to 0 °C. To the cooled solution, *n*-BuLi 2.5 M (1.54 mL, 3.38 mmol, 2.2 eq.) was slowly added (T must stay at 0 °C) to the solution and left to stir at 0 °C for 30 min. After 30 min, 2-methoxy-N-(2-phenylpropan-2-yl)benzenesulfonamide 13 (470 mg, 1.54 mmol, 1 eq.) dissolved in dry THF (1 mL) was added and the solution was stirred at 0 °C for 30 min. After 30 min, carbamoyl chloride (390 μL, 3.08 mmol, 2 eq.) was slowly added at 0 °C. The mixture was left to stir at rt for 16h. The solution was quenched with saturated NH_4Cl solution and extracted with EtOAc (3x). The organic layers were collected, dried (Na_2SO_4) and concentrated in *vacuo*. The crude compound was purified by FC (PE:EtOAc) to yield compound 14 (300 mg, yeld 48 %). Rf: 0.35 (5:5 PE:EtOAc). ^{1}H NMR (400 MHz, DMSO) δ 0.91 (t, $J = 7.1$ Hz, 3H), 1.05 (t, $J = 7.0$ Hz, 3H), 1.43 (s, 3H), 1.50 (s, 3H), 2.89 (q, $J = 7.1$ Hz, 2H), 3.21 (dq, $J = 14.0$, 7.0 Hz, 1H), 3.47 (dq, $J = 14.1$, 7.0 Hz, 1H), 3.86 (s, 3H), 6.70 (dd, $J = 7.6$, 1.0 Hz, 1H), 7.03 (dd, $J = 8.5$, 1.1 Hz, 1H), 7.06–7.13 (m, 1H), 7.14–7.21 (m, 2H), 7.33–7.40 (m, 2H), 7.43 (s, 1H), 7.49 (dd, $J = 8.4$, 7.6 Hz, 1H). ^{13}C NMR (101 MHz, DMSO) δ 11.88, 13.17, 29.15, 29.52, 37.73, 41.87, 55.85, 57.73, 112.18, 119.01, 125.24, 126.17, 126.65, 127.41, 133.43, 137.67, 146.71, 156.06, 167.74. HRMS (ESI) for $C_{12}H_{19}N_2O_4S$ [M + H – $C(CH_3)_2$Ph] calcd.287.1066, found 287.1054; *m/z* for $C_{21}H_{29}N_2O_4S$ [M+H] calcd.405.1348, found: 405.1831.

4.2.2.24. N,N-diethyl-3-methoxy-2-sulfamoylbenzamide (15). In a round bottom flask, N,N-diethyl-3-methoxy-2-(N-(2-phenylpropan-2-yl) sulfamoyl)benzamide 14 (300 mg, 0.74 mmol, 1 eq.) were dissolved in CH_2Cl_2 (2 mL) and cooled to 0 °C. Cold TFA (5 mL) was slowly added and the reaction warmed to rt and stirred for 10 min. After starting material consumption (TLC monitoring) the solvent was removed in vacuo and the residue co-evaporated with CH_2Cl_2 (3x) to obtain a white solid. The crude was used directly (168 mg, yeld 79 %). Rf 0.13 (5:5 PE: EtOAc). ^{1}H NMR (400 MHz, DMSO) δ 0.26 (t, $J = 7.1$ Hz, 3H), 0.43 (t, $J = 7.1$ Hz, 3H), 2.37 (tt, $J = 8.5$, 4.3 Hz, 3H), 2.57 (dd, $J = 13.6$, 7.0 Hz, 1H), 2.85 (dq, $J = 14.2$, 7.2 Hz, 1H), 4.04 (s, 3H), 6.06 (dd, $J = 7.6$, 1.0 Hz, 1H), 6.47 (dd, $J = 8.5$, 1.0 Hz, 1H), 6.81 (dd, $J = 8.4$, 7.6 Hz, 1H). NH_2 is not visible due to its fast exchange. ^{13}C NMR (101 MHz, DMSO) δ 2.71, 3.96, 30.78, 35.10, 47.61, 104.62, 110.99, 119.05, 125.64, 128.61, 149.04, 162.13. HRMS (ESI) for $C_{12}H_{19}N_2O_4S$ [M+H] calcd.287.1066, found: 287.1052.

4.2.2.25. 7-methoxybenzo[d]isothiazol-3(2H)-one 1,1-dioxide (16). In a round bottom flask, 15 (168 mg, 0.58 mmol, 1 eq.) was dissolved in AcOH (3 mL) and heated under reflux for 2 h. The solvent was concentrated in *vacuo* and the residue triturated with HCl 1 N. The solid was filtered, washed with cold water and dried under vacuum at 50 °C. The crude was further purified by trituration with Hexane to give xx as white solid (96 mg, yeld 78 %). Rf 0.20 (7:3:1 EtOAc:PE:TEA). ^{1}H NMR (400 MHz, DMSO) δ 4.01 (s, 3H), 7.51 (dd, $J = 7.5$, 0.7 Hz, 1H), 7.61 (d, $J = 8.4$ Hz, 1H), 7.88 (dd, $J = 8.4$, 7.5 Hz, 1H). ^{13}C NMR (101 MHz, DMSO) δ 56.84, 115.91, 118.50, 125.52, 129.66, 137.01, 153.83, 160.73. HRMS (ESI) for $C_8H_8NO_4S$ [M+H] calcd. 214.0174, found: 214.0168.

4.2.2.26. 3-chloro-7-methoxybenzo[d]isothiazole 1,1-dioxide (17). A mixture of 7-methoxybenzo[d]isothiazol-3(2H)-one 1,1-dioxide 16 (550 mg; 2.58 mmol; 1 eq.), thionyl chloride (280 μL; 3.87 mmol; 1.5 eq.) and a catalytic amount of DMF (14 μL) in 1,4-dioxane (5 mL) was heated for 24h under reflux. The reaction mixture was concentrated, and the residue was recrystallized from toluene, filtered, washed by cold toluene and dried under vacuum at 50 °C to give of a broken white solid. The filtrate was concentrated under reduced pressure and was recrystallized from toluene, filtered, washed by cold toluene. The combined solids were washed by cold toluene and dried under vacuum at 50 °C to give 3-chloro-7-methoxybenzo[d]isothiazole 1,1-dioxide (300 mg; yeld 50 %). ^{1}H NMR (600 MHz, DMSO) δ 4.02 (s, 3H), 7.54 (d, $J = 7.5$ Hz, 1H), 7.64 (dd, $J = 8.0$, 3.6 Hz, 1H), 7.90 (t, $J = 8.0$ Hz, 1H). ^{13}C NMR (151 MHz, DMSO) δ 56.93, 116.08, 118.83, 125.31, 128.20, 128.90, 137.23, 153.95, 160.12. HRMS (ESI) for $C_8H_7ClNO_3S^+$ [M+H]$^+$: calc. 231.9835, found:231,9834.

4.2.2.27. (E)(Z)-4-((2-(2-hydroxyethyl)hydrazineylidene)methyl)-2-methoxyphenol (19). To a solution of 4-hydroxy-3-methoxybenzaldehyde (1.00 g; 6.57 mmol; 1 eq.) in EtOH (25 ml) was added 2-hydroxyethylhydrazine (446 μL; 6.57 mmol; 1 eq.) and sodium acetate 5 (808.8 mg; 9.86 mmol; 1.50 eq.). The solution was heated at 80 °C under MW irradiation for 5 min. The solvent was concentrated under vacuum. The solid was triturated into water, filtered and washed with water to give after drying at 50 °C giving 4-[(E)-(2-hydroxyethylhydrazono) methyl]-2-methoxy-phenol (1.20 g, yeld 58 %) as a yellow solid. ^{1}H NMR (400 MHz, DMSO) δ 9.77 (s, 1H), 8.63 (s, 1H), 7.33 (d, $J = 1.9$ Hz, 1H), 7.23 (dd, $J = 8.2$, 1.9 Hz, 1H), 6.93 (d, $J = 8.1$ Hz, 1H), 3.83 (s, 3H), 3.77–3.66 (m, 2H), 3.31 (t, $J = 5.4$ Hz, 2H). ^{13}C NMR (101 MHz, DMSO) δ 153.12, 148.18, 143.2, 128.69, 124.53, 115.63, 110.72, 55.65, 55.27, 51.65. HRMS (ESI) for $C_{10}H_{15}N_2O_3$ [M+H]$^+$: calc. 211,1083, found 211.1070.

4.2.2.28. (E)-3-(2-(4-hydroxy-3-methoxybenzylidene)-1-(2-hydroxyethyl)hydrazinyl)-7-methoxybenzo[d]isothiazole 1,1-dioxide (20). 3-chloro-7-methoxybenzo[d]isothiazole 1,1-dioxide (290 mg; 1.25 mmol; 1 eq.) was dissolved into dry THF (4 mL) and then added dropwise to a solution of 2-methoxy-4-[(*E*)- (methylhydrazono)methyl]phenol (287 mg; 1.37 mmol; 1.1 eq.) in THF (8 mL). The resulting mixture was stirred under reflux for 1.5 h and then concentrated under vacuum. The solid was triturated into ACN, filtered, washed with ACN and dried, to give (*E*)-3-(2-(4-hydroxy-3-methoxybenzylidene)-1-(2-hydroxyethyl) hydrazinyl)-7-methoxybenzo [d]isothiazole 1,1-dioxide (49.0 mg; yeld 9 %) as a yellow powder. ^{1}H NMR (400 MHz, DMSO) δ 3.75 (t, $J = 6.0$ Hz, 2H), 3.87 (s, 3H), 3.99 (s, 3H), 4.37 (t, $J = 6.0$ Hz, 2H), 5.30 (s, 1H), 7.00 (d, $J = 8.1$ Hz, 1H), 7.30 (dd, $J = 8.2$, 1.9 Hz, 1H), 7.42 (d, $J = 1.9$ Hz, 1H), 7.51 (d, $J = 8.4$ Hz, 1H), 7.86 (t, $J = 8.1$ Hz, 1H), 8.38 (d, $J = 7.9$ Hz, 1H), 8.63 (s, 1H), 9.93 (s, 1H). ^{13}C NMR (101 MHz, DMSO) δ 48.86, 55.41, 56.50, 56.58, 110.49, 115.88, 116.87, 121.81, 122.42, 124.98, 129.42, 129.50, 135.83, 148.10, 148.71, 149.73, 154.29, 158.48. HRMS (ESI) for $C_{18}H_{20}N_3O_6S$ [M+H]$^+$: calcd.406.1073, found = 406.1069. HPLC, t_R: 12.576, purity, 99.1 %.

4.2.2.29. 3-chlorobenzo[d]isothiazole 1,1-dioxide (22). A mixture of saccharin 21 (1 g; 5.46 mmol; 1 eq.), thionyl chloride (590 μL; 8.18 mmol; 1.5 eq.) and a catalytic amount of DMF (5 μL) in 1,4-dioxane (5 mL) was heated for 24hrs under reflux. The reaction mixture was concentrated, and the residue was recrystallized from toluene, filtered, washed by cold toluene and dried under vacuum at 50 °C to give of a broken white solid. The filtrate was concentrated under reduced pressure and was recrystallized from toluene, filtered, washed by cold toluene. The combined solids were washed by cold toluene and dried

under vacuum at 50 °C to give 3-chloro-benzothiazole 1,1-dioxide (548 mg; yeld 50 %). ^{1}H NMR (400 MHz, DMSO) δ 8.15 (dd, J = 6.0 Hz, 1H), 7.95 (m, 3H). HRMS (ESI) for $C_7H_5ClNO_2S^+$ $[M+H]^+$: calc. 201.9730, found:201,9734.

4.2.2.30. (E)-3-(2-(4-hydroxy-3-methoxybenzylidene)-1-(2-hydroxyethyl)hydrazineyl)benzo[d]isothiazole 1,1-dioxide (23). 3-chloro-7-methoxybenzo[d]isothiazole 1,1-dioxide (290 mg; 1.25 mmol; 1 eq.) was dissolved into dry THF (4 mL) and then added dropwise to a solution of 2-methoxy-4-[(*E*)- (methylhydrazono)methyl]phenol (287 mg; 1.37 mmol; 1.1 eq.) in THF (8 mL). The resulting mixture was stirred under reflux for 1.5 h and then concentrated under vacuum. The solid was triturated into ACN, filtered, washed with ACN and dried, to give ((E)-3-(2-(4-hydroxy-3-methoxybenzylidene)-1-(2-hydroxyethyl)hydrazineyl)benzo[d]isothiazole 1,1-dioxide (49.0 mg; yeld 9 %) as a yellow powder. ^{1}H NMR (400 MHz, DMSO) δ 9.77 (s, 1H), 8.67 (s, 1H), 7.51–7.36 (m, 4H)) 7.24 (dd, J = 8.2, 2.0 Hz, 1H), 6.98 (dd, J = 22.2, 8.1 Hz, 2H), 3.83 (s, 3H), 3.76 (dd, J = 6.0, 4.8 Hz, 2H), 3.32 (t, J = 5.4 Hz, 3H), ^{13}C NMR (101 MHz, DMSO) δ 48.86, 55.41, 110.49, 115.88, 116.87, 121.81, 122.42, 124.98, 129.42, 129.50, 135.83, 148.10, 148.71, 149.73, 154.29, 158.48. HRMS (ESI) for $C_{17}H_{18}N_3O_5S$ $[M+H]^+$: calcd.376.0967, found = 376.0960. HPLC, t_R: 10.827, purity, 97.4 %.

HPLC-UV/Vis Purity and ^{1}H/^{13}C NMR characterization of the compounds are reported in Supplementary Information 4 and Supplementary Information 5, respectively.

4.3. Synthesis of the fluorescent probe

Peptides **P6** and **P6-TMR** were assembled on a Syro XP multiple peptide synthesizer (MultiSynTech GmbH, Witten Germany) through a standard Fmoc/t-butyl-based solid-phase peptide synthesis (SPPS). The syntheses were performed on a 0.11 mM scale using a 4-(2′,4′-dimethoxyphenyl-Fmoc-aminomethyl)-phenoxyacetamido-norleucyl-MBHA resin (Rink amide MBHA resin, loading: 0.55 mmol/g). Natural Fmoc-amino acids were used with a four-fold excess and coupled to the growing peptide chain with 1,3-diisopropylcarbodiimide (DIC, 4 eq) and 1-hydroxybenzotriazole (HOBt, 4 eq) as coupling reagents for 1 h at room temperature. Couplings of non-natural amino acids (6-chloro-triptophan, Norleucine, 1-naphthylalanine) and Rhodamine (9-(2-Carboxyphenyl)-3,6-bis(diethylamino)xanthylium chloride) were performed manually with a 1.5 fold excess, using 1-[Bis(dimethylamino) methylene]-1H-1,2,3-triazolo[4,5-b]pyridinium 3-oxid hexafluorophosphate (HATU, 1.7 eq) and N,N-Diisopropylethylamine (DIPEA, 1.7 eq) for the carboxyl group activation. The Fmoc-deprotection was executed in 20 % piperidine in N,N-dimethylformamide. N-terminal acetylation, when required, was performed with a solution of acetic anhydride (0.5 M) and N-methylmorpholine (0.25 M) in DMF. After assembly of the sequences, the resin was washed with DCM and dried. The cleavage cocktail to obtain the desired derivative from the resin consisted of a mixture of 95 % trifluoroacetic acid, 2.5 % water and 2.5 % triethylsilane (TFA:H2O: Et_3SiH). The resins were filtered off, the filtrates were partially concentrated under reduced pressure and then precipitated with cold diethyl ether to obtain crude peptides. Analytical high-performance liquid chromatography (HPLC) was conducted using a Beckman 116 liquid chromatograph with a Beckman 166 diode array detector. Peptide purity was evaluated on an XBridge C18 column (4.6 × 150 mm, 5 μm particle size) at a flow rate of 0.7 mL/min, utilizing a linear gradient from 100 % solvent A (H_2O + 0.1 % TFA) to 100 % solvent B (CH_3CN + 0.1 % TFA) over 25 min. Crude peptides were purified using a reverse phase Waters Prep 600 HPLC system with a Jupiter C18 column (250 × 30 mm, 300 Å, 15 μm spherical particle size), eluted with solvent A (H_2O + 0.1 % TFA) and solvent B (40 % H_2O in CH_3CN + 0.1 % TFA) at a flow rate of 20 mL/min. The gradient was adjusted based on the analytical HPLC profile of the crude peptide. All final compounds exhibited ≥95 % purity when monitored at 220 nm, with their molecular weights confirmed by a mass spectrometer ESI Micromass ZQ. Compounds characterization are reported in **Supplementary Information 1_pag 39**.

4.4. Production of *h*TEAD4 YAP binding domain (TEAD4-YBD)

The synthetic gene encoding for the YAP binding domain of TEAD4 (*h*TEAD4-YBD, residues 217–434), optimized for *E. coli* expression, was purchased from GenScript (www.genscript.com) and subcloned in the pET-15b vector within the restriction sites NdeI-BamHI. The resulting pET-15b – hTEAD4-YBD expression vector was used to heat-shock transform *E. coli* ArcticExpress (DE3) cells (Agilent). Bacteria were cultured at 30 °C in ZYP-5052 auto-induction medium [66], supplemented with 100 mg L^{-1} ampicillin, until the OD_{600nm} became 1, then the culture was cooled to 12 °C and cell growth was continued for 60 h under vigorous aeration. Cells, harvested by centrifugation (3500 g, 20 min, 8 °C), were resuspended in 25 mM TRIS pH 8.0 and 150 mM NaCl (Buffer A), supplemented with 0.5 mg/mL lysozyme (Sigma Aldrich), 0.2 mM phenylmethylsulfonyl fluoride (PMSF) and 20 mM imidazole and then disrupted by sonication after 1 h of incubation on ice. The supernatant of the resulting crude extract was collected by centrifugation (13500 g, 1 h, 8 °C) and further purified by nickel-affinity chromatography on a HisTrap FF 5 mL column (Cytiva). *h*TEAD4-YBD was purified by taking advantage of the His^6-tag added at its N-terminus (HT-*h*TEAD4-YBD), using a three-step gradient protocol. HT-*h*TEAD4-YBD was eluted by applying a 250 mM imidazole concentration in buffer A and then desalted by HiTrap 5 mL desalting column (Cytiva).

4.5. Recombinant hTEAD4 MS characterization

The high purity (estimated as ≥ 98 %) of the mature *h*TEAD4-YBD protein sample was verified by SDS-PAGE analysis and High-Resolution Mass Spectrometry. Production yield is 40 mg (protein)/L (medium) of purified protein. Protein identity and sequence was analyzed with HRMS (Orbitrap Q-Exactive, Thermo Fisher). *h*TEAD4 isoforms were separated with a Bioshell IgG C4 1000 Å, 125 × 2.1 mm (Merck), 0.3mL min^{-1} with a 20min 20–70 % ACN gradient in 0.1 % formic acid, 70 °C on an UltiMate 3000 UHPLC (Thermo Fisher), SID 10 %. Each peak was identified with the FreeStyle deconvolution software (Thermo Fisher) to calculate the exact masses for the myristoilated and non myristoilated isoforms. Parameters were set as follows: min charges 5, charge numbers: 5–50+, adducts $[M + nH]^{n+}$. *h*TEAD4 sequence was confirmed with a ms/ms sequencing after sample digestion, as reported in literature [67]. Peptides were separated on a Hypersil GOLD C18 column, 100 × 2.1 mm (Thermo Fisher) with a 45min linear gradient and analyzed in FullMS/$ddMS^2$ (Top6), nce 28. Data were processed with Mascot Matrix suite against the UniProtKD database [68]. hTEAD4 was identified with a MS^1 tolerance of 10 ppm and a ms/ms tolerance of 0.02Da, carbammidomethylation (C) as fixed modification and oxidation (M), deamidation (N,Q) as variable modifications with Proteome Discoverer v3.1 [69]. Results were checked manually also on SkyLine suite [70]. Cys367 myristoilation was mapped and quantified with Proteome Discoverer v3.1 platform and SkyLine. MS spectra, deconvoluted with FreeStyle software (Thermo Fisher), revealed a higher abundance of myristoilated isoform at Cys367 over the Cys(IAA) form, with an average ratio of 75:25 (calculated on the bases of three different purified batches), as previously reported in literature by crystal structure analysis [71].

4.6. Fluorescence anisotropy assays and K_d determination

UV–vis absorption and fluorescence emission were measured, respectively, on an Agilent Cary 100 spectrophotometer and a Horiba FluoroMax-3 spectrofluorometer. All samples were prepared in 80-20 %

(Hepes 20 mM, KAc 100 mM)-glycerol buffer, pH 7.4. The emission spectra of the TMR probe were measured upon exciting at 550 nm. Emission anisotropy was computed between 570 and 630 nm from the four acquired emission curves, I_{vv} (λ), I_{vh} (λ), I_{hh} (λ) and I_{hv} (λ), where v and h indicate the directions, vertical and horizontal, of the excitation and emission polarizers. The anisotropy values used in the quantitative analyses were obtained as averages of the values between 575 and 600 nm.

The affinity of **P6-TMR** for TEAD4 was determined from the anisotropy values measured in the titration of 1.5 μM peptide with a 10 μM protein solution. The latter was added up to a 4.2 μM final hTEAD4 concentration. After each addition, the **P6-TMR** concentration, modified by dilution, was measured spectrophotometrically using a molar extinction coefficient of 100000 M^{-1} cm^{-1} at the absorption maximum, 568 nm. The anisotropy values were employed within a standard binding analysis to determine the dissociation constant of the TEAD4/**P6-TMR** complex, shortly TP: $TP \rightleftarrows T + P$, $K^{TP} = \frac{[T][P]}{[TP]}$. Straightforward passages show that the equilibrium constant is the slope of a linear plot with $x = f_{TP}/(1\text{-}f_{TP})$, where f_{TP} is the mole fraction of peptide bound to the protein and $y = [T]_t - f_{TP}[P]_t$, t meaning total. It is equally easy to see that $f_{TP}=(r\text{-}r_0)/(r_\infty\text{-}r_0)$, where r_0 and r_∞ are the anisotropies measured at titration start and end corresponding, respectively, to the anisotropies of free and protein-bound **P6-TMR**. Once determined the dissociation constant of the TEAD4/**P6-TMR** complex, the K_ds of the syntehsized compounds were estimated from TMR anisotropy in displacement experiments. Typically, six samples containing 830 μl of a solution containing 1 μM TEAD4 and 300 nM **P6-TMR** were prepared in six fluorescence quartz 1×0.4 cm^2 cuvettes. DMSO alone or in a mixture with a 4 mM solution of the compound in the same solvent were added so that the total amount of DMSO was the same, 5 % v/v, in all samples, while the concentrations of the added displacer ranged from 0 (control) to several tens of microMolar. The TMR emission anisotropies were measured after addition, 30 min and, sometimes, 1 h later. The final results, whenever they exhibited a regular decrease with increasing displacer concentration, were employed for the quantitative analysis of the displacement reaction, $TP + D \rightleftarrows TD + P$ (D = displacer). This was carried out as reported in the literature [43,44]. We assumed a value for the K_d of the displacer and, for a given concentration of the latter, combined the previously determined equilibrium constant for the TEAD4/**P6-TMR** complex and the total concentrations of the protein and the peptide to compute f_{TP}, the fraction of protein-bound peptide and, using the previously determined r_∞ and r_0, the corresponding value of r. The computed anisotropy was plotted as a function of the displacer concentration and compared, both visually and in terms of squared deviation, with the experimental results; the displacer K_d was gradually modified to minimize this deviation. In some cases, we observed opalescence in the samples as well as an increase in the absorption baseline, suggesting precipitation of part of the added compound in the mostly aqueous solvent. In some of these cases, the anisotropy results showed little reproducibility and a scattered behaviour, thus not allowing us to obtain reasonable K_ds from their analyses. In some other cases, while the data analyses produced acceptable fittings, low hydrosolubility of the displacer might have limited its effective concentration in solution, thus leading to overestimated K_ds and an underestimated affinity for TEAD4.

4.7. Cell cultures

HT29 and HCT116 human colon-rectal cancer (5-FU-resistant adenocarcinoma) cell lines [72] were cultured in Dulbecco's modified Eagle medium (DMEM) (Euroclone, Devon, UK), supplemented with 10 % heat-inactivated (30 min at 56 °C) fetal bovine serum (Euroclone) and 1 % Pen/Strep (Euroclone). A2780 human ovarian carcinoma cell line [73] was grown in RPMI 1640 medium, supplemented with 10 % heat-inactivated (30 min at 56 °C) fetal bovine serum, 1 % Pen/Strep (Euroclone) and 50 μg/mL of gentamycin sulphate. Cells were incubated at 37 °C under a humidified atmosphere containing 5 % CO_2. All cell culture reagents were purchased from Euroclone (Devon, UK).

4.8. Analysis of cell growth inhibition by crystal violet dye assay

Compounds were solubilized in DMSO (*VWR Amresco*) to achieve a final concentration of 8 mM in the mother solution. 24 h after cell seeding into 24-well plates, cytotoxicity assays were carried out on the cell lines by adding 2.5 μL of mother solution, to preliminarily test all the compounds with a concentration of 40 μM. Thus, a deeper evaluation of the compound activity has been developed through the cytotoxicity curves at 5, 10, 20 and 40 μM, by serially diluting the stock solution of 8 mM. All experiments were conducted in triplicate. 72 h after treatment, the tissue culture medium was removed, and the cell monolayer fixed with methanol and stained with 0.2 % Crystal Violet (*Sigma Aldrich*) solution in 20 % methanol for at least 1 h. After washing to remove excess dye, the cells were left to dry. The incorporated dye was solubilized in acidified isopropanol (1 N HCl:2-propanol, 1:10, 20 %). Absorbance was determined spectrophotometrically at 540 nm with a TECAN GeniosPro microplate reader. The extracted dye was proportional to cell number. The percentage of cytotoxicity was calculated by comparing the absorbance of cultures exposed to the drug to un-exposed (control) cultures [74].

4.9. Cell transfection with compounds by SAINT-protein delivery system

Transfection of compounds was performed by an adaptation of the standard transfection protocol of the SAINT-Protein delivery system (Synvolux Therapeutics, Groningen, NL). Complexes of drugs (≤4 μL) with SAINT-Protein (7 μL) were prepared for the treatment in a 24-well without vortexing. The mixture was incubated for 5 min at room temperature, then filled with serum-free medium. The culture medium was aspirated from the cells, the SAINT-Protein/drug complex was added to the wells and incubated 4 h (37 °C; 5 % CO_2). After this time, complete medium was added to reach the appropriate volume. All experiments were conducted in triplicate. 72 h after treatment, the tissue culture medium was removed, and the cell monolayer fixed with methanol and stained with 0.2 % Crystal Violet (Sigma Aldrich) solution in 20 % methanol for at least 1 h and processed as above mentioned.

4.10. Study of YAP expression levels and TEAD target genes

The cells under examination were seeded in 6-well plates at a confluence of 50 %, approximately 500 thousand cells in a final volume of medium corresponding to 3 ml. Once attached, the cells were treated by adding the compounds directly into the culture medium: **6i** (80 μM), **6j** (55 μM), **6a** (60 μM), and **VP** (12 μM) was used as a reference molecule. The SAINT-Protein (# SP-3004-01 Synvolux products) was adopted to facilitate the internalization of the compound for the RT-PCR assay. The compounds under examination were treated with the selected compounds and cells were collected after 48h from the treatment time to study the expression levels of the genes under examination. Total RNA from cultured cells was isolated with Purelink RNA Mini Kit (Life Technologies) according to the manufacturer's instructions and was quantified using a NanoDrop ND-1000 instrument (Thermo Scientific). Purity was determined by measuring absorbance at 260 and 280 nm and calculating the A260/280 ratio. DNase treatment and cDNA synthesis were performed starting from 1 μg of total RNA using Maxima H(−) MasterMix (#M1682, Life Technologies) following the manufacturer's instructions. Subsequently, quantification of transcript levels was achieved by qRT-PCR experiments performed on the CFX96 Connect Real-Time System instrument (Bio-Rad) using SsoAdvanced Universal SYBR™ Green Supermix (BIO-RAD) and each sample was analyzed independently tripled. Specially designed primers, each at a final concentration of 400 nM. The amplification reaction (95 °C, 2 min; 40 cycles of 95 °C, 5 s and 60 °C, 30 s) was followed by a melting curve

generated by increasing the temperature in small increments (from 65 °C to 95 °C, 0 0.5 °C/s). Relative quantification was performed according to the ΔΔCt method [75]. **SI1**-Table S12 reports the primers used for real-time RT-PCR assays.

4.11. Western blot assay

Cells were harvested and washed in ice-cold PBS and suspended in 80ul RIPA (Radio-Immunoprecipitation Assay) buffer supplemented with protease and phosphatase inhibitors (#78442, Thermo Scientific). The insoluble debris was removed by centrifugation at 14,000 g for 30 min at 4 °C. Proteins were quantified with a Bradford assay (final-concentration of about 5ug/ul). Cellular extracts were resolved using 4–15 % SDS-PAGE and transferred to Nitrocellulose membranes. Immunoblot analysis was performed using anti-TEAD 4 (WH0007004M1 MONOCLONAL ANTI-TEAD4 mouse Merck, 1:1000), anti-Pan TEAD (Cell Signaling 1:1000) and anti-a-Tubulin mouse MAB (DM1A-Merck 1:1000). Horseradish peroxidase-conjugated secondary antibodies (Anti-Rabbit A6667, Anti Mouse A5906, Sigma Aldrich) were used to detect the bound primary antibody. Immune complexes were visualized by enhanced chemiluminescence (Amersham ECL Prime Western blotting reagent, RPN2235, cytiva) following the manufacturer's instructions. Amersham Imager 680 RGB was used for the analysis. The bands obtained by immunoblot were analyzed by ImageJ (Java-based image-processing and analysis software).

4.12. Luciferase reporter assays to determine YAP-TEAD activity in the cell

HEK293T cell lines were cultured in Dulbecco's modified Eagle medium (DMEM) (Euroclone, Devon, UK), supplemented with 10 % heat-inactivated (30 min at 56 °C) fetal bovine serum (Euroclone). Cells were incubated at 37 °C under a humidified atmosphere containing 5 % CO2. All cell culture reagents were purchased from Euroclone (Devon, UK). Cells were subjected to a co-transfection of plasmids, *i.e.* pRL-CMV Renilla (40 ng), 8xGT-LUX (250 ng) and pCDNA3 – YAP (250 ng). DNA transfections were performed with TransIT®-LT1 Transfection Reagent (Mirus Bio) according to the reverse transfection protocol provided by the manufacturer.

Cells under examination were seeded in 96-well plates at a confluence of 70 %, in a final volume of medium corresponding to 100uL. Once attached, after 18h of transfection cells were treated with **6i** (80 μM), **6j** (55 μM), **6a** (60 μM), and **VP** (12 μM) as a reference molecule. After 24 h of treatment with the compounds, samples are supplemented with luciferin coelenterazine. The light emitted from the enzyme-luminescent reaction is measured using a luciferase reader (GloMax Promega). Data were normalized by dividing the Firefly luciferase activity by the Renilla luciferase activity to correct for any variations in transfection efficiency.

4.13. Coimmunoprecipitation

HCT116 cells were treated with different concentrations of 6a in combination with SAINT Protein (Synvolux SP-3004). After 8h of treatments, cells were harvested with NP40 Lysis Buffer (FNN0021, Thermo Fisher, 50 mM Tris-HCl pH 7.4, 250 mM NaCl, 5 mM EDTA, 50 mM NaF, 1 mM Na3VO4, 1 % NP-40, 0.02 % NaN3, 1 mM PMSF) using a cell scraper on ice. Cells were vortexed and placed on ice three times for 30 s each. ext, cells were centrifuged at 4 °C for 30 min at 13.000 rpm. At the end, the supernatants were collected into new sterile tubes. An amount of 400 μL of KPL Protein G agarose (5720-0004, Seracare) was washed with cold lysis buffer three times. Next, lysates were incubated with 20 μL of KPL Protein G Agarose with Control Rabbit IgG for 1 h at 4 °C with rotation (pre-cleaning). Protein concentration was determined after the pre-cleaning using the Bradford assay. 1 mg of pre-cleared lysate was taken for each condition, incubated with 70 ng of primary antibody (Anti Pan-TEAD (D3F7L) e Anti YAP (D8H1X)) or IgG control overnight at, and 20 μL of KPL Protein G Agarose at 4 °C with gentle rotation. The next day, samples were washed four times with cold lysis buffer to remove unbound proteins. Bound proteins were eluted by adding Laemmli sample buffer 2X and DTT and heating at 95 °C for 5 min. Samples were resolved by SDS-PAGE and transferred to nitrocellulose membranes. Membranes were blocked and probed with Anti Pan-TEAD (D3F7L), Anti YAP (Santa Cruz, sc-101199) or Anti α-TUBULIN (CP06, Sigma Aldrich) and HRP-conjugated secondary antibodies. Signal detection was performed using chemiluminescence (Bio-Rad ChemiDoc™ Imagers).

4.14. Whole cell MS proteomics sample preparation

Cells were prepared as reported in the previous paragraph according to d'Arca et al. with slight modifications [76]. Briefly, cell pellets were scraped in PBS buffer, lysed with 200uL of 8 M Urea and 3 cycles of sonication, 10s, on ice bath (Soniplus). Samples were then centrifuged at 14,000 g and the supernatant concentration was determined with a BCA assay (Thermo Fisher, Waltham, Massachusetts, U.S.). The equivalent of 50 μg of protein soluble lysate was treated in triplicate per sample with a standard FASP protocol. Briefly, samples were loaded into a Millipore 30 kDa MWCO centrifugal filters (Merck, Darmstadt, Germany), heat-denatured, reduced with excess dithiothreitol, cys-alkylated with iodoacetamide, and digested with 1 mg/mL mass spectrometry grade trypsin (Roche, Basel, Switzerland). The obtained peptides were desalted in a C18 SPE columns (Empore 3 M) and the eluted peptides were dried down in a SpeedVac (Eppendorf's) [77]. Samples were stored at −80° until MS analysis.

4.15. MS proteomics analysis and data elaboration

Samples were reconstituted to a final concentration of 0.5 mg/mL with mobile phase and injected in a nLC-nESI-HRMS (Orbitrap Exploris 480, Thermo Fisher, Waltham, Massachusetts, U.S) at the Centro Interdipartimentale Grandi Strumenti (CIGS, UniMoRe). Peptides were separated on an EASY-Spray C18, 75 cm × 75 μm capillary column at 200 nL/min (40 °C) with a 160min gradients from 2 to 30 % organic phase. MS was operating in data dependant acquisition mode, with a top = 20 method with 30nce as collision energy, scan range 375–1500 m/z, normalized ACG target 300 %, MaxIT 120s, 120000 resolution. MS/MS parameters were 15000 for resolution, 1.5 m/z of isolation window and 0.4 m/z for isolation offset.

Raw data were loaded onto Proteome Discoverer Tool (Thermo Fisher, Waltham, Massachusetts, U.S), and a LFQ analysis with an ANOVA was applied between control replicates and each treatment. Identification was run against a validated *H. sapiens* UniProtKD database (updated on May 2023) and cRAP, with an FDR 1 % and Chimerys extension [78,79]. M(ox) and N-term acetylation were considered as variable modifications, where C(IAA) as fixed modification. Quantitation was based on chromatographic peak heights. Differentially expressed proteins (DEPs) were identified as those entries with a $-1 \leq FC \leq 1$ (where FC stands for Fold Change and represents $\log_2$ of the abundance ratio with respect to control) with a significance level of p-value <0.05 between triplicates, corrected with FDR 5 %, and expressed as -log(10)q-value. Proteins identified with no *Unique peptides*, with a sequence coverage <5 %, and/or with <2 general peptides were excluded from the analysis. STRING and PANTHER tools were used for DEP's analysis and the protein lists converted into genes with the standard notation, with a *p*-value threshold for the analysis set to <0.05. DepMap with CHRONOS algorithm was used to compare experimental Proteomics results with CRISP/Cas9 knock out data on the corresponding neges. Local STRING network reported in Fig. 14B was obtained has the following features: Number of nodes: 7, number of edges: 16, average node degree: 4.57 avg. local clustering coefficient: 0.952, expected number of edges: 5, PPI enrichment p-value:5.55e-05. PANTHER analysis was performed with the tool 'gene list analysis',

molecular function (MF) GOs, by loading the DEPs of each sample treatment. The nominal number of genes associated to our proteins for each MF-GOs were converted to percentage and compared to each other.

4.16. Statistical analysis

Statistical analysis was performed using using GraphPad Prism v7. Unless stated otherwise, the experiments were carried out in replicate and the values were presented as the mean ± standard deviation. Statistical significance of comparison was assessed using the unpaired T-test or one-way ANOVA detailed in each experiment. Differences among the groups were considered statistically significant with: ns, not significant, $p > 0.05$; $^{**}p < 0.01$; $^{***}p < 0.001$. MS Proteomics q-values were generated from p-values obtained with ANOVA tests and corrected with BH adjustments.

CRediT authorship contribution statement

Laura Scalvini: Methodology, Investigation, Data curation. **Lorenzo Tagliazucchi:** Methodology, Investigation, Data curation. **Gian Marco Elisi:** Methodology, Investigation, Data curation. **Dana Zappaterra:** Methodology, Investigation. **Maria Gaetana Moschella:** Methodology, Investigation. **Sebastian Fantini:** Methodology, Investigation. **Daniele Aiello:** Writing – original draft, Methodology, Investigation. **Remo Guerrini:** Writing – original draft, Methodology, Investigation, Conceptualization. **Valentina Albanese:** Methodology, Investigation. **Salvatore Pacifico:** Methodology, Investigation. **Ludovica Lopresti:** Methodology, Investigation. **Giulia Malpezzi:** Writing – original draft, Methodology, Investigation. **Giulia Saporito:** Methodology, Investigation. **Stefania Ferrari:** Methodology, Investigation, Conceptualization. **Michele Lamesta:** Methodology, Investigation. **Lorena Losi:** Writing – original draft, Supervision, Investigation, Conceptualization. **Cecilia Pozzi:** Writing – original draft, Methodology, Investigation, Conceptualization. **Stefano Mangani:** Methodology, Investigation. **Gaetano Marverti:** Writing – review & editing, Writing – original draft, Methodology, Investigation, Data curation, Conceptualization. **Alberto Venturelli:** Methodology, Investigation. **Glauco Ponterini:** Writing – review & editing, Writing – original draft, Supervision, Methodology, Investigation, Formal analysis, Data curation, Conceptualization. **Domenico D'Arca:** Writing – review & editing, Writing – original draft, Methodology, Investigation, Conceptualization. **Marco Mor:** Writing – original draft, Visualization, Methodology, Investigation, Conceptualization. **Maria Paola Costi:** Writing – review & editing, Writing – original draft, Supervision, Resources, Methodology, Investigation, Funding acquisition, Conceptualization.

Funding

The present work was supported by i. FAR 2021 Mission Oriented-FAR2021INTERM_O_UNIM ("TEAD ligands prevent YAP binding and combat colorectal cancer growth and resistance", awarded to M.P.C.), ii. PRIN 2022 "YAP-TEAD impairment to target the Hippo pathway induced cancer cell growth (TEAD-I3T)" project code 2022WYAZ47awarded to M.P.C. This work has been carried out in the frame of the ALIFAR project, funded by the Italian Ministry of University thorugh the program "Dipartimenti di Eccellenza 2023–2027"; Associazione Italiana per la Ricerca sul cancro IG25785, to M.P.C.

Declaration of competing interest

The authors declare the following financial interests/personal relationships which may be considered as potential competing interests: Maria Paola Costi reports financial support was provided by Italian Association for Cancer Research. Maria Paola Costi reports financial support was provided by Ministry of Education and Merit. Marco Mor reports financial support was provided by Ministry of Education and Merit. If there are other authors, they declare that they have no known competing financial interests or personal relationships that could have appeared to influence the work reported in this paper.

Acknowledgement

This work was carried out using the HPC (High Performance Computing) computational facilities of the University of Parma, Italy; http://www.hpc.unipr.it. The authors acknowledge the "Fondazione Cassa di Risparmio di Modena" for funding the UHPLC-ESI/HRMS Q-Exactive system at the Centro Interdipartimentale Grandi Strumenti (CIGS) of the University of Modena and Reggio Emilia, employed for TEAD4 MS characterization.

Appendix A. Supplementary data

Supplementary data to this article can be found online at https://doi.org/10.1016/j.ejmech.2025.118056.

Data availability

Data will be made available on request.

References

[1] A. Lauriola, E. Uliassi, M. Santucci, M.L. Bolognesi, M. Mor, L. Scalvini, G.M. Elisi, G. Gozzi, L. Tagliazucchi, G. Marverti, S. Ferrari, L. Losi, D. D'Arca, M.P. Costi, Identification of a quinone derivative as a YAP/TEAD activity modulator from a repurposing library, Pharmaceutics 14 (2022) 391, https://doi.org/10.3390/pharmaceutics14020391.

[2] M. Fu, Y. Hu, T. Lan, K.-L. Guan, T. Luo, M. Luo, The hippo signalling pathway and its implications in human health and diseases, Signal Transduct Target Ther 7 (2022) 376, https://doi.org/10.1038/s41392-022-01191-9.

[3] K.F. Harvey, X. Zhang, D.M. Thomas, The hippo pathway and human cancer, Nat. Rev. Cancer 13 (2013) 246–257, https://doi.org/10.1038/nrc3458.

[4] T. Zhou, X. Li, J. Liu, J. Hao, The Hippo/YAP signaling pathway: the driver of cancer metastasis, Cancer Biol. Med. 20 (2023), https://doi.org/10.20892/j.issn.2095-3941.2023.0164.

[5] X.-L. Liu, R. Zuo, W.-B. Ou, The hippo pathway provides novel insights into lung cancer and mesothelioma treatment, J. Cancer Res. Clin. Oncol. 144 (2018) 2097–2106, https://doi.org/10.1007/s00432-018-2727-0.

[6] M. Chi, J. Liu, C. Mei, Y. Shi, N. Liu, X. Jiang, C. Liu, N. Xue, H. Hong, J. Xie, X. Sun, B. Yin, X. Meng, B. Wang, TEAD4 functions as a prognostic biomarker and triggers EMT via PI3K/AKT pathway in bladder cancer, J. Exp. Clin. Cancer Res. 41 (2022) 175, https://doi.org/10.1186/s13046-022-02377-3.

[7] S. Noguchi, A. Saito, M. Horie, Y. Mikami, H.I. Suzuki, Y. Morishita, M. Ohshima, Y. Abiko, J.S.M. Mattsson, H. König, M. Lohr, K. Edlund, J. Botling, P. Micke, T. Nagase, An integrative analysis of the tumorigenic role of TAZ in human non–small cell lung cancer, Clin. Cancer Res. 20 (2014) 4660–4672, https://doi.org/10.1158/1078-0432.CCR-13-3328.

[8] S. He, K. Gao, L. Mao, S. Bhushan, Z. Xiao, Gene silencing of transcription factor *TEAD4* inhibits esophageal cancer cells by regulating TCF7, Cancer Biother. Radiopharm. (2020) 3870, https://doi.org/10.1089/cbr.2020.3870, cbr.2020.

[9] L. Lv, X. Zhou, Targeting hippo signaling in cancer: novel perspectives and therapeutic potential, MedComm 4 (2023), https://doi.org/10.1002/mco2.375.

[10] Z. Li, B. Zhao, P. Wang, F. Chen, Z. Dong, H. Yang, K.-L. Guan, Y. Xu, Structural insights into the YAP and TEAD complex, Genes Dev. 24 (2010) 235–240, https://doi.org/10.1101/gad.1865810.

[11] P. Furet, B. Salem, Y. Mesrouze, T. Schmelzle, I. Lewis, J. Kallen, P. Chène, Structure-based design of potent linear peptide inhibitors of the YAP-TEAD protein-protein interaction derived from the YAP omega-loop sequence, Bioorg Med Chem Lett 29 (2019) 2316–2319, https://doi.org/10.1016/j.bmcl.2019.06.022.

[12] S. Yuan, H.C.S. Chan, Z. Hu, Using <scp>PyMOL</scp> as a platform for computational drug design, WIREs Computational Molecular Science 7 (2017), https://doi.org/10.1002/wcms.1298.

[13] A. Al-Moujahed, K. Brodowska, T.P. Stryjewski, N.E. Efstathiou, I. Vasilikos, J. Cichy, J.W. Miller, E. Gragoudas, D.G. Vavvas, Verteporfin inhibits growth of human glioma in vitro without light activation, Sci. Rep. 7 (2017) 7602, https://doi.org/10.1038/s41598-017-07632-8.

[14] C. Wang, X. Zhu, W. Feng, Y. Yu, K. Jeong, W. Guo, Y. Lu, G.B. Mills, Verteporfin inhibits YAP function through up-regulating 14-3-3σ sequestering YAP in the cytoplasm, Am. J. Cancer Res. 6 (2016) 27–37.

[15] J. Giraud, S. Molina-Castro, L. Seeneevassen, E. Sifré, J. Izotte, C. Tiffon, C. Staedel, H. Boeuf, S. Fernandez, P. Barthelemy, F. Megraud, P. Lehours, P. Dubus, C. Varon, Verteporfin targeting YAP1/TAZ-TEAD transcriptional activity inhibits the tumorigenic properties of gastric cancer stem cells, Int. J. Cancer 146 (2020) 2255–2267, https://doi.org/10.1002/ijc.32667.

[16] L. Mélin, S. Abdullayev, A. Fnaiche, V. Vu, N. González Suárez, H. Zeng, M. M. Szewczyk, F. Li, G. Senisterra, A. Allali-Hassani, I. Chau, A. Dong, S. Woo, B. Annabi, L. Halabelian, S.R. LaPlante, M. Vedadi, D. Barsyte-Lovejoy, V. Santhakumar, A. Gagnon, Development of LM98, a small-molecule TEAD inhibitor derived from flufenamic acid, ChemMedChem 16 (2021) 2982–3002, https://doi.org/10.1002/cmdc.202100432.

[17] P. Chan, X. Han, B. Zheng, M. DeRan, J. Yu, G.K. Jarugumilli, H. Deng, D. Pan, X. Luo, X. Wu, Autopalmitoylation of TEAD proteins regulates transcriptional output of the hippo pathway, Nat. Chem. Biol. 12 (2016) 282–289, https://doi.org/10.1038/nchembio.2036.

[18] Y. Sun, L. Hu, Z. Tao, G.K. Jarugumilli, H. Erb, A. Singh, Q. Li, J.L. Cotton, P. Greninger, R.K. Egan, Y. Tony Ip, C.H. Benes, J. Che, J. Mao, X. Wu, Pharmacological blockade of TEAD–YAP reveals its therapeutic limitation in cancer cells, Nat. Commun. 13 (2022) 6744, https://doi.org/10.1038/s41467-022-34559-0.

[19] A. Kaneda, T. Seike, T. Danjo, T. Nakajima, N. Otsubo, D. Yamaguchi, Y. Tsuji, K. Hamaguchi, M. Yasunaga, Y. Nishiya, M. Suzuki, J.-I. Saito, R. Yatsunami, S. Nakamura, Y. Sekido, K. Mori, The novel potent TEAD inhibitor, K-975, inhibits YAP1/TAZ-TEAD protein-protein interactions and exerts an anti-tumor effect on malignant pleural mesothelioma, Am. J. Cancer Res. 10 (2020) 4399–4415.

[20] W. Lu, M. Fan, W. Ji, J. Tse, I. You, S.B. Ficarro, I. Tavares, J. Che, A.Y. Kim, X. Zhu, A. Boghossian, M.G. Rees, M.M. Ronan, J.A. Roth, S.M. Hinshaw, B. Nabet, S.M. Corsello, N. Kwiatkowski, J.A. Marto, T. Zhang, N.S. Gray, Structure-based design of Y-shaped covalent TEAD inhibitors, J. Med. Chem. 66 (2023) 4617–4632, https://doi.org/10.1021/acs.jmedchem.2c01548.

[21] M. Fan, W. Lu, J. Che, N.P. Kwiatkowski, Y. Gao, H.-S. Seo, S.B. Ficarro, P. C. Gokhale, Y. Liu, E.A. Geffken, J. Lakhani, K. Song, M. Kuljanin, W. Ji, J. Jiang, Z. He, J. Tse, A.S. Boghossian, M.G. Rees, M.M. Ronan, J.A. Roth, J.D. Mancias, J. A. Marto, S. Dhe-Paganon, T. Zhang, N.S. Gray, Covalent disruptor of YAP-TEAD association suppresses defective Hippo signaling, eLife 11 (2022), https://doi.org/10.7554/eLife.78810.

[22] A.W. Tolcher, N.J. Lakhani, M. Mckean, T. Lingaraj, L. Victor, M. Sanchez-Martin, K. Kacena, K.S. Malek, S. Santillana, A phase 1, First-in-Human study of IK-930, an oral TEAD inhibitor targeting the Hippo pathway in subjects with advanced solid tumors, J. Clin. Oncol. (2022), https://doi.org/10.1200/JCO.2022.40.16_suppl.TPS3168 n.d.

[23] T.T. Tang, A.W. Konradi, Y. Feng, X. Peng, M. Ma, J. Li, F.-X. Yu, K.-L. Guan, L. Post, Small molecule inhibitors of TEAD auto-palmitoylation selectively inhibit proliferation and tumor growth of *NF2* -deficient mesothelioma, Mol Cancer Ther 20 (2021) 986–998, https://doi.org/10.1158/1535-7163.MCT-20-0717.

[24] T.J. Hagenbeek, J.R. Zbieg, M. Hafner, R. Mroue, J.A. Lacap, N.M. Sodir, C. L. Noland, S. Afghani, A. Kishore, K.P. Bhat, X. Yao, S. Schmidt, S. Clausen, M. Steffek, W. Lee, P. Beroza, S. Martin, E. Lin, R. Fong, P. Di Lello, M.H. Kubala, M.N.-Y. Yang, J.T. Lau, E. Chan, A. Arrazate, L. An, E. Levy, M.N. Lorenzo, H.-J. Lee, T.H. Pham, Z. Modrusan, R. Zang, Y.-C. Chen, M. Kabza, M. Ahmed, J. Li, M. T. Chang, D. Maddalo, M. Evangelista, X. Ye, J.J. Crawford, A. Dey, An allosteric pan-TEAD inhibitor blocks oncogenic YAP/TAZ signaling and overcomes KRAS G12C inhibitor resistance, Nat. Cancer 4 (2023) 812–828, https://doi.org/10.1038/s43018-023-00577-0.

[25] M. Rajurkar, M. Sanchez-Martin, D. Hidalgo, N. Young, B. Amidon, G. Punkosdy, J. Ecsedy, L. Xu, IK930, a novel TEAD inhibitor, sensitizes KRAS and EGFR mutant tumors to oncogene targeted therapy, Eur. J. Cancer 174 (2022) S40, https://doi.org/10.1016/s0959-8049(22)00906-6.

[26] A. Dey, X. Varelas, K.-L. Guan, Targeting the Hippo pathway in cancer, fibrosis, wound healing and regenerative medicine, Nat. Rev. Drug Discov. 19 (2020) 480–494, https://doi.org/10.1038/s41573-020-0070-z.

[27] P. Chène, Direct inhibition of the YAP : TEAD interaction: an unprecedented drug discovery challenge, ChemMedChem 19 (2024), https://doi.org/10.1002/cmdc.202400361.

[28] A. Anbanandam, D.C. Albarado, C.T. Nguyen, G. Halder, X. Gao, S. Veeraraghavan, Insights into transcription enhancer factor 1 (TEF-1) activity from the solution structure of the TEA domain, Proc. Natl. Acad. Sci. 103 (2006) 17225–17230, https://doi.org/10.1073/pnas.0607171103.

[29] Z. Zhou, T. Hu, Z. Xu, Z. Lin, Z. Zhang, T. Feng, L. Zhu, Y. Rong, H. Shen, J.M. Luk, X. Zhang, N. Qin, Targeting Hippo pathway by specific interruption of YAP-TEAD interaction using cyclic YAP-like peptides, FASEB J. 29 (2015) 724–732, https://doi.org/10.1096/fj.14-262980.

[30] Z. Zhang, Z. Lin, Z. Zhou, H.C. Shen, S.F. Yan, A.V. Mayweg, Z. Xu, N. Qin, J. C. Wong, Z. Zhang, Y. Rong, D.C. Fry, T. Hu, Structure-based design and synthesis of potent cyclic peptides inhibiting the YAP–TEAD protein–protein interaction, ACS Med. Chem. Lett. 5 (2014) 993–998, https://doi.org/10.1021/ml500160m.

[31] M. Barth, S. Contal, C. Montalbetti, L. Spitzer, New Compounds Inhibitors of the yap/taz-tead Interaction and their Use in the Treatment of Malignant Mesothelioma, 2017. WO2017064277A1.

[32] H. Sellner, E. Chapeau, P. Furet, M. Voegtle, B. Salem, M. Le Douget, V. Bordas, J. Groell, A. Le Goff, C. Rouzet, T. Wietlisbach, T. Zimmermann, J. McKenna, C. E. Brocklehurst, P. Chène, M. Wartmann, C. Scheufler, J. Kallen, G. Williams, S. Harlfinger, M. Traebert, B.M. Dumotier, T. Schmelzle, N. Soldermann, Optimization of a class of dihydrobenzofurane analogs toward orally efficacious YAP-TEAD protein-protein interaction inhibitors, ChemMedChem 18 (2023), https://doi.org/10.1002/cmdc.202300051.

[33] E.A. Chapeau, L. Sansregret, G.G. Galli, P. Chène, M. Wartmann, T.P. Mourikis, P. Jaaks, S. Baltschukat, I.A.M. Barbosa, D. Bauer, S.M. Brachmann, C. Delaunay, C. Estadieu, J.E. Faris, P. Furet, S. Harlfinger, A. Hueber, E. Jiménez Núñez, D. P. Kodack, E. Mandon, T. Martin, Y. Mesrouze, V. Romanet, C. Scheufler, H. Sellner, C. Stamm, D. Sterker, L. Tordella, F. Hofmann, N. Soldermann, T. Schmelzle, Direct and selective pharmacological disruption of the YAP–TEAD interface by IAG933 inhibits Hippo-dependent and RAS–MAPK-altered cancers, Nat. Cancer (2024), https://doi.org/10.1038/s43018-024-00754-9.

[34] D. Bajusz, A. Rácz, K. Héberger, Why is Tanimoto index an appropriate choice for fingerprint-based similarity calculations? J. Cheminform. 7 (2015) 20, https://doi.org/10.1186/s13321-015-0069-3.

[35] J. Rosenbluh, D. Nijhawan, A.G. Cox, X. Li, J.T. Neal, E.J. Schafer, T.I. Zack, X. Wang, A. Tsherniak, A.C. Schinzel, D.D. Shao, S.E. Schumacher, B.A. Weir, F. Vazquez, G.S. Cowley, D.E. Root, J.P. Mesirov, R. Beroukhim, C.J. Kuo, W. Goessling, W.C. Hahn, β-Catenin-Driven cancers require a YAP1 transcriptional complex for survival and tumorigenesis, Cell 151 (2012) 1457–1473, https://doi.org/10.1016/j.cell.2012.11.026.

[36] X. Liu, H. Li, M. Rajurkar, Q. Li, J.L. Cotton, J. Ou, L.J. Zhu, H.L. Goel, A. M. Mercurio, J.-S. Park, R.J. Davis, J. Mao, Tead and AP1 coordinate transcription and motility, Cell Rep. 14 (2016) 1169–1180, https://doi.org/10.1016/j.celrep.2015.12.104.

[37] Y. Xia, Y.-L. Zhang, C. Yu, T. Chang, H.-Y. Fan, YAP/TEAD Co-Activator regulated pluripotency and chemoresistance in ovarian cancer initiated cells, PLoS One 9 (2014) e109575, https://doi.org/10.1371/journal.pone.0109575.

[38] J. Payandeh, M. Volgraf, Ligand binding at the protein–lipid interface: strategic considerations for drug design, Nat. Rev. Drug Discov. 20 (2021) 710–722, https://doi.org/10.1038/s41573-021-00240-2.

[39] J. Dong, N.-N. Wang, Z.-J. Yao, L. Zhang, Y. Cheng, D. Ouyang, A.-P. Lu, D.-S. Cao, ADMETlab: a platform for systematic ADMET evaluation based on a comprehensively collected ADMET database, J. Cheminform. 10 (2018) 29, https://doi.org/10.1186/s13321-018-0283-x.

[40] S.A. Ashraf, A.E.O. Elkhalifa, K. Mehmood, M. Adnan, M.A. Khan, N.E. Eltoum, A. Krishnan, M.S. Baig, Multi-targeted molecular docking, pharmacokinetics, and drug-likeness evaluation of okra-derived ligand abscisic acid targeting signaling proteins involved in the development of diabetes, Molecules 26 (2021) 5957, https://doi.org/10.3390/molecules26195957.

[41] Z.-Y. Yang, Z.-J. Yang, J.-H. He, A.-P. Lu, S. Liu, T.-J. Hou, D.-S. Cao, Benchmarking the mechanisms of frequent hitters: limitation of PAINS alerts, Drug Discov. Today 26 (2021) 1353–1358, https://doi.org/10.1016/j.drudis.2021.02.003.

[42] R.F. Barghash, W.M. Eldehna, M. Kovalová, V. Vojáčková, V. Kryštof, H.A. Abdel-Aziz, One-pot three-component synthesis of novel pyrazolo[3,4-b]pyridines as potent antileukemic agents, Eur. J. Med. Chem. 227 (2022) 113952, https://doi.org/10.1016/j.ejmech.2021.113952.

[43] Z.-X. Wang, An exact mathematical expression for describing competitive binding of two different ligands to a protein molecule, FEBS Lett. 360 (1995) 111–114, https://doi.org/10.1016/0014-5793(95)00062-E.

[44] G. Di Rocco, I. Martinelli, S. Pacifico, R. Guerrini, E. Cichero, P. Fossa, S. Franchini, S. Cardarelli, M. Giorgi, M. Sola, G. Ponterini, Fluorometric detection of protein-ligand engagement: the case of phosphodiesterase5, J. Pharm. Biomed. Anal. 149 (2018) 335–342, https://doi.org/10.1016/j.jpba.2017.11.014.

[45] P. Rzasa, S. Whelan, P. Farahmand, H. Cai, I. Guterman, R. Palacios-Gallego, S. S. Undru, L. Sandford, C. Green, C. Andreadi, M. Mintseva, E. Parrott, H. Jin, F. Hey, S. Giblett, N.B. Sylvius, N.S. Allcock, A. Straatman-Iwanowska, R. Feuda, C. Tufarelli, K. Brown, C. Pritchard, A. Rufini, BRAFV600E-mutated serrated colorectal neoplasia drives transcriptional activation of cholesterol metabolism, Commun. Biol. 6 (2023) 962, https://doi.org/10.1038/s42003-023-05331-x.

[46] W.C. Chiang, T.M. Geel, M.M. Altintas, S. Sever, M.H.J. Ruiters, J. Reiser, Establishment of protein delivery systems targeting podocytes, PLoS One 5 (2010) e11837, https://doi.org/10.1371/journal.pone.0011837.

[47] D. Cardinale, G. Guaitoli, D. Tondi, R. Luciani, S. Henrich, O.M.H. Salo-Ahen, S. Ferrari, G. Marverti, D. Guerrieri, A. Ligabue, C. Frassineti, C. Pozzi, S. Mangani, D. Fessas, R. Guerrini, G. Ponterini, R.C. Wade, M.P. Costi, Protein–protein interface-binding peptides inhibit the cancer therapy target human thymidylate synthase, Proc. Natl. Acad. Sci. 108 (2011), https://doi.org/10.1073/pnas.1104829108.

[48] G. Marverti, M.G. Moschella, A. Belardo, M. Lamesta, G. Mercanile, L. Tagliazucchi, D. Aiello, A. Venturelli, D. Illuminati, R. Guerrini, L. Losi, G. Ponterini, M.P. Costi, D. D'Arca, Enhanced anticancer effect of thymidylate synthase dimer disrupters by promoting intracellular accumulation, Front. Pharmacol. 15 (2024), https://doi.org/10.3389/fphar.2024.1477318.

[49] X. Shen, X. Peng, Y.G. Guo, Z. Dai, L. Cui, W. Yu, Y. Liu, C.Y. Liu, YAP/TAZ enhance P-body formation to promote tumorigenesis, eLife12:RP88573 (2023).

[50] L. Xie, X. Song, H. Lin, Z. Chen, Q. Li, T. Guo, T. Xu, T. Su, M. Xu, X. Chang, L.-K. Wang, B. Liang, D. Huang, Aberrant activation of CYR61 enhancers in colorectal cancer development, J. Exp. Clin. Cancer Res. 38 (2019) 213, https://doi.org/10.1186/s13046-019-1217-9.

[51] J. Liang, L. Wang, C. Wang, J. Shen, B. Su, A.L. Marisetty, D. Fang, C. Kassab, K. J. Jeong, W. Zhao, Y. Lu, A.K. Jain, Z. Zhou, H. Liang, S.-C. Sun, C. Lu, Z.-X. Xu, Q. Yu, S. Shao, X. Chen, M. Gao, F.X. Claret, Z. Ding, J. Chen, P. Chen, M.C. Barton, G. Peng, G.B. Mills, A.B. Heimberger, Verteporfin inhibits PD-L1 through autophagy and the STAT1–IRF1–TRIM28 signaling axis, exerting antitumor efficacy, Cancer Immunol. Res. 8 (2020) 952–965, https://doi.org/10.1158/2326-6066.CIR-19-0159.

[52] C. Wei, X. Li, Verteporfin inhibits cell proliferation and induces apoptosis in different subtypes of breast cancer cell lines without light activation, BMC Cancer 20 (2020) 1042, https://doi.org/10.1186/s12885-020-07555-0.

[53] P.D. Thomas, D. Ebert, A. Muruganujan, T. Mushayahama, L. Albou, H. Mi, scp>PANTHER</scp> : making genome-scale phylogenetics accessible to all, Protein Sci. 31 (2022) 8–22, https://doi.org/10.1002/pro.4218.

[54] Y.-C. Chiu, S. Zheng, L.-J. Wang, B.S. Iskra, M.K. Rao, P.J. Houghton, Y. Huang, Y. Chen, Predicting and characterizing a cancer dependency map of tumors with deep learning, Sci. Adv. 7 (2021), https://doi.org/10.1126/sciadv.abh1275.
[55] J.M. Dempster, I. Boyle, F. Vazquez, D.E. Root, J.S. Boehm, W.C. Hahn, A. Tsherniak, J.M. McFarland, Chronos: a cell population dynamics model of CRISPR experiments that improves inference of gene fitness effects, Genome Biol. 22 (2021) 343, https://doi.org/10.1186/s13059-021-02540-7.
[56] M. Witkowska, P. Smolewski, SMAD family proteins: the current knowledge on their expression and potential role in neoplastic diseases, Postepy Hig. Med. Dosw. 68 (2014) 301–309, https://doi.org/10.5604/17322693.1094726.
[57] F. Yao, Z. Zhou, J. Kim, Q. Hang, Z. Xiao, B.N. Ton, L. Chang, N. Liu, L. Zeng, W. Wang, Y. Wang, P. Zhang, X. Hu, X. Su, H. Liang, Y. Sun, L. Ma, SKP2- and OTUD1-regulated non-proteolytic ubiquitination of YAP promotes YAP nuclear localization and activity, Nat. Commun. 9 (2018) 2269, https://doi.org/10.1038/s41467-018-04620-y.
[58] H. Mi, D. Ebert, A. Muruganujan, C. Mills, L.-P. Albou, T. Mushayamaha, P. D. Thomas, PANTHER version 16: a revised family classification, tree-based classification tool, enhancer regions and extensive API, Nucleic Acids Res. 49 (2021) D394–D403, https://doi.org/10.1093/nar/gkaa1106.
[59] W.L. Jorgensen, D.S. Maxwell, J. Tirado-Rives, Development and testing of the OPLS all-atom force field on conformational energetics and properties of organic liquids, J. Am. Chem. Soc. 118 (1996) 11225–11236, https://doi.org/10.1021/ja9621760.
[60] J.B. Baell, G.A. Holloway, New substructure filters for removal of pan assay interference compounds (PAINS) from screening libraries and for their exclusion in bioassays, J. Med. Chem. 53 (2010) 2719–2740, https://doi.org/10.1021/jm901137j.
[61] Schrödinger Release 2024-2, LigPrep, Schrödinger, LLC, New York, NY, 2024 n.d.
[62] R.C. Johnston, K. Yao, Z. Kaplan, M. Chelliah, K. Leswing, S. Seekins, S. Watts, D. Calkins, J. Chief Elk, S.V. Jerome, M.P. Repasky, J.C. Shelley, Epik: pK_a and protonation state prediction through machine learning, J. Chem. Theory Comput. 19 (2023) 2380–2388, https://doi.org/10.1021/acs.jctc.3c00044.
[63] T.A. Halgren, R.B. Murphy, R.A. Friesner, H.S. Beard, L.L. Frye, W.T. Pollard, J. L. Banks, Glide: a new approach for rapid, accurate docking and scoring. 2. Enrichment factors in database screening, J. Med. Chem. 47 (2004) 1750–1759, https://doi.org/10.1021/jm030644s.
[64] M.P. Repasky, M. Shelley, R.A. Friesner, Flexible ligand docking with glide, Curr. Protoc. Bioinformatics 18 (2007), https://doi.org/10.1002/0471250953.bi0812s18.
[65] S.L. Dixon, A.M. Smondyrev, S.N. Rao, PHASE: a novel approach to pharmacophore modeling and 3D database searching, Chemical Biology & Drug Design 67 (2006) 370–372, https://doi.org/10.1111/j.1747-0285.2006.00384.x.
[66] F.W. Studier, Protein production by auto-induction in high-density shaking cultures, Protein Expr. Purif. 41 (2005) 207–234, https://doi.org/10.1016/j.pep.2005.01.016.
[67] K.R. Ludwig, M.M. Schroll, A.B. Hummon, Comparison of in-solution, FASP, and S-Trap based digestion methods for Bottom-Up proteomic studies, J. Proteome Res. 17 (2018) 2480–2490, https://doi.org/10.1021/acs.jproteome.8b00235.
[68] A. Bateman, M.-J. Martin, S. Orchard, M. Magrane, R. Agivetova, S. Ahmad, E. Alpi, E.H. Bowler-Barnett, R. Britto, B. Bursteinas, H. Bye-A-Jee, R. Coetzee, A. Cukura, A. Da Silva, P. Denny, T. Dogan, T. Ebenezer, J. Fan, L.G. Castro, P. Garmiri, G. Georghiou, L. Gonzales, E. Hatton-Ellis, A. Hussein, A. Ignatchenko, G. Insana, R. Ishtiaq, P. Jokinen, V. Joshi, D. Jyothi, A. Lock, R. Lopez, A. Luciani, J. Luo, Y. Lussi, A. MacDougall, F. Madeira, M. Mahmoudy, M. Menchi, A. Mishra, K. Moulang, A. Nightingale, C.S. Oliveira, S. Pundir, G. Qi, S. Raj, D. Rice, M. R. Lopez, R. Saidi, J. Sampson, T. Sawford, E. Speretta, E. Turner, N. Tyagi, P. Vasudev, V. Volynkin, K. Warner, X. Watkins, R. Zaru, H. Zellner, A. Bridge, S. Poux, N. Redaschi, L. Aimo, G. Argoud-Puy, A. Auchincloss, K. Axelsen, P. Bansal, D. Baratin, M.-C. Blatter, J. Bolleman, E. Boutet, L. Breuza, C. Casals-Casas, E. de Castro, K.C. Echioukh, E. Coudert, B. Cuche, M. Doche, D. Dornevil, A. Estreicher, M.L. Famiglietti, M. Feuermann, E. Gasteiger, S. Gehant, V. Gerritsen, A. Gos, N. Gruaz-Gumowski, U. Hinz, C. Hulo, N. Hyka-Nouspikel, F. Jungo, G. Keller, A. Kerhornou, V. Lara, P. Le Mercier, D. Lieberherr, T. Lombardot, X. Martin, P. Masson, A. Morgat, T.B. Neto, S. Paesano, I. Pedruzzi, S. Pilbout, L. Pourcel, M. Pozzato, M. Pruess, C. Rivoire, C. Sigrist, K. Sonesson, A. Stutz, S. Sundaram, M. Tognolli, L. Verbregue, C.H. Wu, C.N. Arighi, L. Arminski, C. Chen, Y. Chen, J.S. Garavelli, H. Huang, K. Laiho, P. McGarvey, D. A. Natale, K. Ross, C.R. Vinayaka, Q. Wang, Y. Wang, L.-S. Yeh, J. Zhang, P. Ruch, D. Teodoro, UniProt: the universal protein knowledgebase in 2021, Nucleic Acids Res. 49 (2021) D480–D489, https://doi.org/10.1093/nar/gkaa1100.
[69] B.C. Orsburn, Proteome discoverer—A community enhanced data processing suite for protein informatics, Proteomes 9 (2021) 15, https://doi.org/10.3390/proteomes9010015.
[70] L.K. Pino, B.C. Searle, J.G. Bollinger, B. Nunn, B. MacLean, M.J. MacCoss, The skyline ecosystem: informatics for quantitative mass spectrometry proteomics, Mass Spectrom. Rev. 39 (2020) 229–244, https://doi.org/10.1002/mas.21540.
[71] Y. Li, S. Liu, E.Y. Ng, R. Li, A. Poulsen, J. Hill, A.V. Pobbati, A.W. Hung, W. Hong, T.H. Keller, C. Kang, Structural and ligand-binding analysis of the YAP-binding domain of transcription factor TEAD4, Biochem. J. 475 (2018) 2043–2055, https://doi.org/10.1042/BCJ20180225.
[72] K. Bracht, A.M. Nicholls, Y. Liu, W.F. Bodmer, 5-Fluorouracil response in a large panel of colorectal cancer cell lines is associated with mismatch repair deficiency, Br. J. Cancer 103 (2010) 340–346, https://doi.org/10.1038/sj.bjc.6605780.
[73] C.M. Beaufort, J.C.A. Helmijr, A.M. Piskorz, M. Hoogstraat, K. Ruigrok-Ritstier, N. Besselink, M. Murtaza, W.F.J. van Ijcken, A.A.J. Heine, M. Smid, M.J. Koudijs, J. D. Brenton, E.M.J.J. Berns, J. Helleman, Ovarian cancer cell line panel (OCCP): clinical importance of in vitro morphological subtypes, PLoS One 9 (2014) e103988, https://doi.org/10.1371/journal.pone.0103988.
[74] G. Marverti, G. Gozzi, A. Lauriola, G. Ponterini, S. Belluti, C. Imbriano, M.P. Costi, D. D'Arca, The 1,10-Phenanthroline ligand enhances the antiproliferative activity of DNA-intercalating Thiourea-Pd(II) and -Pt(II) complexes against cisplatin-sensitive and -Resistant human ovarian cancer cell lines, Int. J. Mol. Sci. 20 (2019) 6122, https://doi.org/10.3390/ijms20246122.
[75] K.J. Livak, T.D. Schmittgen, Analysis of relative gene expression data using real-time quantitative PCR and the 2(-Delta Delta C(T)) method, Methods. 25 (2001) 402–408, n.d.
[76] D. D'Arca, L. Severi, S. Ferrari, L. Dozza, G. Marverti, F. Magni, C. Chinello, L. Pagani, L. Tagliazucchi, M. Villani, G. d'Addese, I. Piga, V. Conteduca, L. Rossi, G. Gurioli, U. De Giorgi, L. Losi, M.P. Costi, Serum mass spectrometry proteomics and protein set identification in response to FOLFOX-4 in drug-resistant ovarian carcinoma, Cancers (Basel) 15 (2023) 412, https://doi.org/10.3390/cancers15020412.
[77] J.R. Wiśniewski, Filter aided sample preparation – a tutorial, Anal. Chim. Acta 1090 (2019) 23–30, https://doi.org/10.1016/j.aca.2019.08.032.
[78] T.U. Consortium, UniProt: the universal protein knowledgebase, Nucleic Acids Res. 45 (2017) D158–D169, https://doi.org/10.1093/nar/gkw1099.
[79] D. Mellacheruvu, Z. Wright, A.L. Couzens, J.-P. Lambert, N.A. St-Denis, T. Li, Y. V Miteva, S. Hauri, M.E. Sardiu, T.Y. Low, V.A. Halim, R.D. Bagshaw, N.C. Hubner, A. al-Hakim, A. Bouchard, D. Faubert, D. Fermin, W.H. Dunham, M. Goudreault, Z.-Y. Lin, B.G. Badillo, T. Pawson, D. Durocher, B. Coulombe, R. Aebersold, G. Superti-Furga, J. Colinge, A.J.R. Heck, H. Choi, M. Gstaiger, S. Mohammed, I. M. Cristea, K.L. Bennett, M.P. Washburn, B. Raught, R.M. Ewing, A.-C. Gingras, A. I. Nesvizhskii, The CRAPome: a contaminant repository for affinity purification–mass spectrometry data, Nat. Methods 10 (2013) 730–736, https://doi.org/10.1038/nmeth.2557.